ISSN 0972-0405

# ISET JOURNAL OF EARTHQUAKE TECHNOLOGY

Vol. 47 No. 1 March 2010

## CONTENTS



**Financial Assistance from AICTE and DST, New Delhi for the Publication of ISET Journals for 2009–2010 is duly acknowledged.**

ISET Journal of Earthquake Technology, Paper No. 507, Vol. 47, No. 1, March 2010, pp. 1–23

# TECOMÁN EARTHQUAKE: PHYSICAL IMPLICATIONS OF SEISMIC SOURCE MODELING, APPLYING THE EMPIRICAL GREEN'S FUNCTION METHOD, AND EVIDENCE OF NONLINEAR BEHAVIOR OF GROUND

Alejandro Ramírez-Gaytán*, Jorge Aguirre** and Carlos I. Huerta-López***

*Geological Sciences Department, San Diego State University
San Diego, CA 92182-1020, U.S.A.
**Instituto de Ingeniería, Universidad Nacional Autónoma de México
04510 México, D.F., Mexico
***Civil Engineering and Surveying Department, University of Puerto Rico at Mayaguez
Mayagüez, PR 00681-8041, U.S.A.

## ABSTRACT

In this study, we generate a source model for the Tecomán Mexico earthquake of January 22, 2003. The presence of soft soils and the location of eight of the ten major cities of Colima state in its earthquake prone area are important factors to model the seismic source. We model in the frequency interval of 1–10 Hz, because many buildings, bridges and civil construction have their dominant vibration periods in this range. For generating the model, we apply the empirical Green's function method (EGFM) considering the Tecomán earthquake ($M_W$ = 7.5) as the target event and the November 19, 2006 ($M_W$ = 5.5) earthquake as the element event. At the recording site of MANZ, we did a spectral analysis to compare weak and strong ground motions in order to identify if some energy distribution is biased and concentrated at certain frequencies in the frequency interval of 1–10 Hz. The synthetic waveforms and Fourier spectra show good fitting with the observed ones at five stations. The latter roughly correspond to the dislocation model found by Yagi et al. (2004).

**KEYWORDS:** Empirical Green's Function Method (EGFM), Manzanillo Recording Station (MANZ), Target Event, Element Event

## INTRODUCTION

Colima, due to its location, is one of the states of Mexico that are subjected to the occurrences of destructive earthquakes. Much of this seismicity has originated in the subduction zone, along the Pacific coast of Mexico. Although the rate of seismicity is lower than that in the state of Guerrero, it is not negligible. Two examples are the earthquakes of 1932 ($M_W$ = 8.0) and 2003 ($M_W$ = 7.5) (see Figure 1), which are the largest earthquakes recorded throughout Mexico during the last and present century, respectively.

The instrumentation and seismicity in the state did not receive adequate attention, and until 2005 Colima had only a single accelerograph station. Although Red Sísmica del Estado de Colima (RESCO) was operating, its network was installed with the purpose of monitoring the activity of the Colima volcano, and it did not produce useful records since all of them were saturated during the Tecomán earthquake. Thus, the investigations have been made only based on teleseismic and regional records (dominated by low frequencies), to determine the source model of the two largest earthquakes that have affected the region. However, the absence of accelerographic and wide-band networks inside Colima does not permit us to tackle source models in high frequencies.

Yagi et al. (2004) generated a source model that showed a clear directivity towards inside the state (i.e., El Gordo graben and Colima graben). Zobin and Pizano-Silva (2007) also showed directivity in the same zone. In these areas, the Tecomán earthquake ($M_W$ = 7.5) produced more damage than the Manzanillo earthquake (October 9, 1995; $M_W$ = 8.0). Therefore, it is important to generate a source model in high frequencies that can be used in future to estimate high-acceleration records in the area affected by the directivity of the Tecomán earthquake. It is useful in seismic engineering to recover the histories of acceleration because many structures have natural periods in the high-frequency range (1–10 Hz). We took the first step to reach this objective in this study: the use of available data to generate a source model.

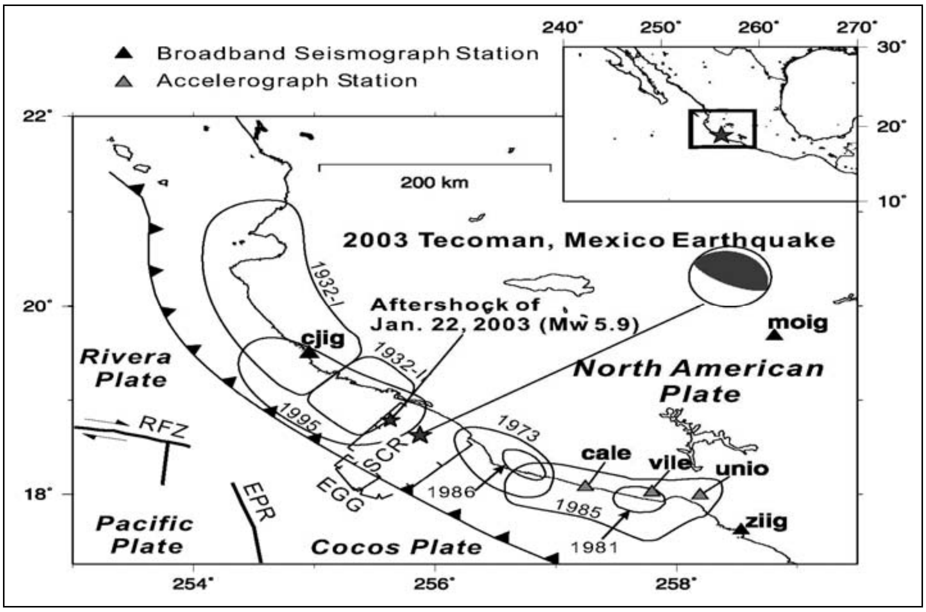


Fig. 1 Geographic map showing the location and rupture area of the major earthquakes that occurred in the region (from Yagi et al., 2004)

Five stations were used for modeling the seismic source of the Tecomán earthquake (January 22, 2003; $M_W$ = 7.5). The local condition of the MANZ site is alluvial soft soil and the maximum acceleration recorded at this site is 0.37*g*. Due to these two particular conditions, an immediate doubt arises whether the site responded with a significant nonlinear behavior in the frequency interval of 1–10 Hz, which is our frequency band of interest.

In order to solve the lack of instrumentation in the region, we initiated a project whose main objective was to set up instruments permanently in Colima. For this purpose, we installed a temporary network consisting of 16 accelerographs and 9 short-band seismographs. All instruments were installed along the 120-km long coastline and inside the Colima state. The data recorded by this network can be used in future to simulate the peak ground acceleration and time-histories of the ground acceleration during the Tecomán earthquake. However, in this study we tried to take the first step: to generate a source model.

As a result of the instrumentation work, on November 19, 2006, this network recorded the most important event since the earthquake of 2003. Its epicenter can be seen in Figure 2. This earthquake was recorded at 16 acceleration stations and 9 velocity stations of the temporary network installed as part of the project. This event was located within the rupture area of the Tecomán earthquake (of January, 2003). In addition to our network, this was recorded by the local acceleration station in Manzanillo (MANZ) and four velocity-type broad-band stations of Servicio Sismológico Nacional (SSN), which are the same stations that recorded the Tecomán earthquake. The features mentioned above allow the application of the empirical Green´s function method proposed by Irikura (1986), by using the earthquake of November 19, 2006, to simulate the Tecomán earthquake.

We estimated the strong motion generation areas (SMGAs) by using this method and the frequency band of 1–10 Hz, which corresponds to high frequencies that cannot be modeled by other theoretical approaches, due to the lack of cortical structure information. The SMGAs are rectangular areas where the slip exceeds the average slip of the fault; it is considered that in this area the slip, stress drop, and rupture velocity are constants (Miyake et al., 2003). This simple source model has been successfully applied to simulate acceleration records of some moderate and large earthquakes. However, unlike the SMGAs, the asperities are estimated through inversions using low frequencies in the 0.1–0.5 Hz range. An asperity is defined as a region within the dislocation area, in which the slip exceeds the average slip in the entire dislocation area (Somerville et al., 1999).

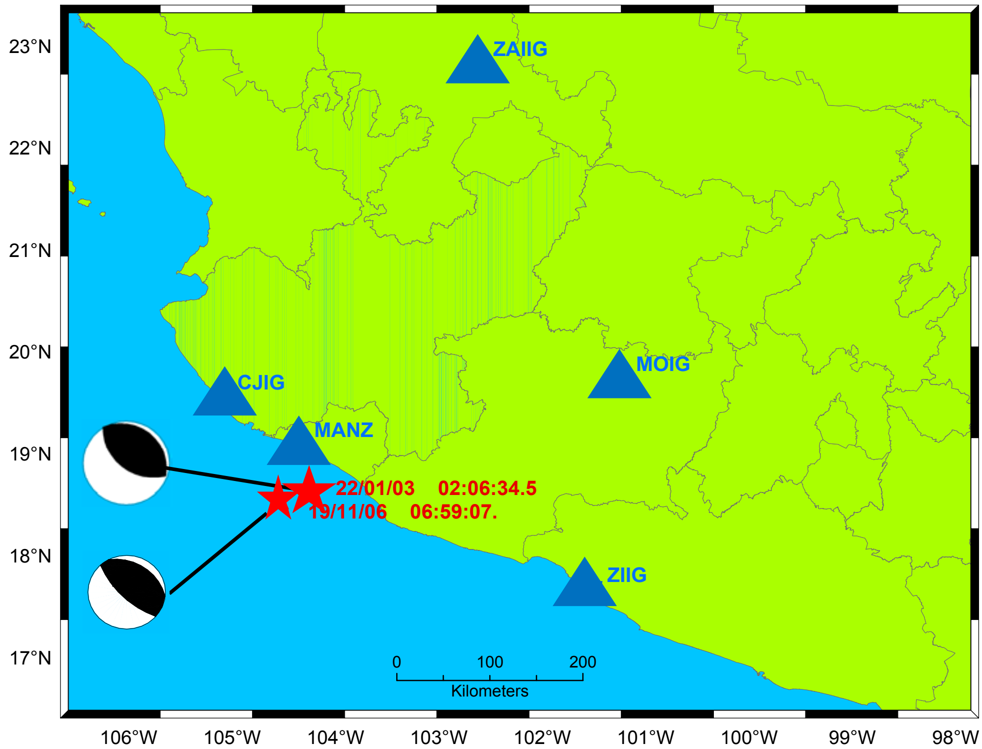


Fig. 2 Geographic map showing the epicentral locations and focal mechanisms of the Tecomán earthquake and the event of November 19, 2006, along with the geographical locations of the local acceleration stations and regional stations that recorded both earthquakes

Miyake et al. (2003) showed that the SMGAs are located almost on the same positions as the asperities and that those match roughly the areas of highest dislocation or asperities, according to the criterion established by Somerville et al. (2002). Based on this criterion, the SMGAs found in our best model are compared with the dislocation model found by Yagi et al. (2004). Somerville et al. (1999) suggested that the dislocation for a subduction earthquake is characterized by a spatial variation of asperities in the dislocation area, and examined how the dislocation models are scaled with the seismic moment. Since our estimates of SMGAs approximately match the areas of highest dislocation or asperities, we quantified the characteristics of our SMGAs individually and as a whole to compare them with the relationships proposed by Somerville et al. (2002). It was found that these relationships are suitable to be applied to the subduction zone under study.

The fact that sediments can amplify earthquake ground motions was recognized at least 100 years ago (Milne, 1898). However, there has been a lingering uncertainty as to whether the degree of amplification varies with the level of input motion. This issue remains one of the most important questions with regard to understanding and predicting earthquake ground motions.

According to the energy conservation principle, seismic-wave amplitudes generally increase in sediments due to lower densities and/or lower seismic velocities. In addition, resonance effects can occur where abrupt impedance contrasts exist. If sediments were perfectly elastic, their response would be independent of the incident-wave amplitudes. As with any real material, however, sediments begin to yield at some level of strain, and this violation of the Hooke's law gives rise to nonlinear response.

The engineering community has long believed that sediment nonlinearity is significant. This perspective was based almost entirely on the laboratory studies, where observed stress-strain loops imply a reduced effective shear modulus and an increased damping (i.e., lower $Q$) at higher levels of strain. A reduced shear modulus alone implies an increased amplification, depending on how it is measured. However, the increased damping generally tends to dominate, thus resulting in a reduced amplification (and even possible de-amplification). One manifestation of this perspective was that peak ground acceleration (PGA) got reduced (or deamplified) at sediment sites when rock-site PGA exceeded 0.1$g$ (Seed and Idriss, 1982). The 1985 Michoacán and 1989 Loma Prieta earthquakes however changed this perspective, by shifting the threshold between PGA amplification and deamplification to ~0.4$g$ for deep, soft clay sites (Finn, 1991; Idriss, 1990). Furthermore, the data obtained during the 1989 Loma Prieta and 1994 Northridge earthquakes indicated a threshold of ~0.6*g* for deep, stiff soil sites (Chang and Bray, 1998).

On the other hand, seismologists have traditionally been skeptical of the significance of sediment nonlinearity, in spite of the fact that one of their very own (Reid, 1910) recognized and described the potential effect some 90 years ago (in the same paper that introduced the elastic-rebound theory of faulting). The prevailing seismological perspective as of 1988 was reflected in a seminal review paper by Aki (1988), who wrote, "... except for the obvious case of liquefaction, ... the amplification factor obtained using weak motion data can be used to predict ... strong ground motion ...". The reason for this view was either that nonlinear effects were indeed insignificant, or that they could not be resolved among the myriad of other effects complicating a very limited number of strong-motion observations. Seismologists were also skeptical that laboratory studies reflect the 'in situ' behavior, both because of the well-known difficulties in obtaining undisturbed samples, and because such studies do not include the effects of scattering attenuation. Given a lack of direct evidence for sediment nonlinearity, seismologists naturally opted for the simpler linear model (which is also generally more conservative in terms of the predicted ground motion). Keiiti Aki turned out to be one of the earliest seismological converts. In a follow-up review paper, he wrote, "Non-linear amplification at sediment sites appears to be more pervasive than seismologists used to think" (Aki, 1993).

A published seismological study claims to have identified a pervasive nonlinear effect (Field et al., 1997); and sediment amplification factors were inferred from the 1994 Northridge earthquake main shock, which were up to a factor of two less, on average, than for the relatively weak-motion aftershocks. Although this nonlinear interpretation seems to be most reasonable, it remains to be seen whether the conclusion holds up to an additional scrutiny. Given the recent progress, the time is ripe to reassess our present understanding (or, lack thereof) with respect to the nonlinear sediment response. In general terms, Hooke's law is only an approximation, especially because some degree of nonlinearity is apparent in laboratory studies at even the lowest detectable strain levels. The question is more of degree, or of the adequacy of the linear model under various conditions, especially in comparison with the other commonly made approximations (such as isotropy). In other words, when is sediment nonlinearity a first-order effect in terms of understanding or predicting earthquake ground motions?

Based on the statements published in several papers related to nonlinear effects, we have carried out a spectral analysis comparing weak, moderate, and strong ground motions as an alternate way to identify empirically if some energy is concentrated at particular frequencies (which may be used as an indicator of the nonlinear effects) in the frequency interval of 1–10 Hz for the MANZ site. This alternative is adopted here because a detailed nonlinear analysis is a different kind of study, which is out of the context of our research.

## TECTONIC AND HISTORICAL SEISMICITY

There are three seismic sources in the state of Colima. The first source is the Colima volcano that generates microtremors and low-magnitude earthquakes (of magnitudes generally less than 3.5). The second source comes from the seismic block of Jalisco, which is located in the North American plate and borders on the east with the Rivera plate, southward with the El Gordo graben and the Colima graben, and in the north with the graben of Tepic and Chapala (Bandy et al., 1995). In this region there have been significant intraplate earthquakes with magnitudes not greater than 6.0. In our temporary seismic network, we recorded a significant seismic activity in this area, which seems to be cut exactly on the limits between the El Gordo graben and the block of Jalisco.

The most important seismic source in the region is the subduction zone, located in front of the coast of the state of Colima, where the Rivera, Cocos and North America plates converge. The Cocos and Rivera plates are subducting under the North American plate at an average rate of 5 cm per year. This mechanism occurs in front of the coast of the state in the area known as El Gordo graben (see Figure 1).

The Tecomán earthquake occurred in the seismic gap that forms the boundaries of the rupture area of the 1973 and 1995 earthquakes. However, the location of the aftershocks of the Tecomán earthquake indicates that their rupture area covers the northern part of the El Gordo graben and invades part of the rupture zone of the 1932 and 1995 earthquakes. The absence of aftershocks in the southwest indicates that half of this seismic gap was not broken (Quintanar et al., 2010).

An analysis of the data presented in Table 1 shows that the 1995 and 1932 earthquakes, although they had different rupture areas, had the same $M_W$ (equal to 8.0). This indicates that the earthquake of 1995 released an amount of energy equivalent to that of the largest recorded earthquake in the history of Mexico.

**Table 1: Location Data, Magnitude and Seismic Moment of Main Earthquake Occurrences in the Region**

| Date | Latitude | Longitude | $M_0$ (N-m) | $M_W$ |
|---|---|---|---|---|
| 1932 06 03 | 19.80° | −104.00° | $9.1\times10^{20}$ | 8.0* |
| 1932 06 18 | 18.95° | −104.42° | $7.3\times10^{20}$ | 7.9* |
| 1973 01 30 | 18.39° | −103.21° | $3\times10^{20}$ | 7.6+ |
| 1995 10 09 | 19.05° | −104.20° | $9.1\times10^{20}$ | 8.0** |
| 2003 01 22 | 18.625° | −104.12° | $1.6\times10^{20}$ | 7.5** |

*Singh et al. (1985); +Alcocer and Klingner (2006); **Harvard CMT[1]

The big difference between the seismic moments of the 1995 earthquake ($M_0$ = $9.0\times10^{20}$ N-m) and the Tecomán earthquake ($M_0$ = $1.6\times10^{20}$ N-m) shows that the Tecomán earthquake had much less energy than the earthquake of 1995. However, the damage caused by the Tecomán earthquake was much higher in the urban areas of the state with the exception of Manzanillo city. Directivity is one of the reasons that can explain this phenomenon. The earthquake directivity towards the interior of the North American plate coincides with the geographical locations of eight of the ten largest urban areas in the state. Because these urban areas along with the earthquake rupture direction are located within the Colima graben, it is important in future projects to explore the role of this graben in the conduction of seismic energy (through the transmission, reflection and refraction of waves) produced by this source. The site effects produced by the alluvial or dilluvial deposits within the graben also have to be considered. These two phenomena together could be responsible for the large accelerations in the area. The difference between the seismic moments of the 1995 and 2003 earthquakes, which share a zone of rupture area, suggests that if an earthquake of similar magnitude to the 1995 earthquake occurs in the portion of the seismic gap inside the Colima graben, going by the above-explained causes it would create a very critical seismic scenario for the region.

## DATA

We collected records from the main shock of January 22, 2003 (i.e., the target event) and the earthquake of November 19, 2006 (i.e., the element event), both recorded at the accelerograph station MANZ (see Figure 2), which is owned by Federal Electricity Commission (CFE) and operated by Centro de Instrumentación y Registro Sísmico (CIRES). This station is located 54 km away from the epicenter and is the nearest accelerograph station that recorded the Tecomán earthquake. The equipment is a DCA-333 three-component accelerograph that records the acceleration waveform with 100 samples per second and has a trigger threshold of 4.9 gal (0.049 m/s$^2$).

Attempts were made to collect acceleration records for both events from the stations of Servicio Sismológico Nacional (SSN) with good azimuthal coverage around the target event and those stations are Chamela (CJIG), Morelia (MOIG), Zacatecas (ZAIG), and Zihuatanejo (ZIIG) (see Figure 2). According to the information provided by the staff of SSN, the acceleration records were not stored in memory, in contrast with the velocity records that are stored in memory. For this reason we had to work with the velocity records. The four stations being considered have broad-band seismographs: those at the stations CJIG and ZIIG have a sampling rate of 80 samples per second, while those at the stations MOIG and ZAIG have a sampling rate of 100 samples per second. The data was first changed from the original format to the ASCII format and was subsequently converted from velocity to acceleration.

The focal mechanisms adopted for the main shock and secondary earthquake are same as those reported by Harvard CMT[1], i.e., strike 308°, dip 12°, and slip 110° for the main shock, and strike 300°, dip 21°, and slip 74° for the secondary earthquake (see Table 2). The dislocation area is assumed to be 70×85 km which is same as in Yagi et al. (2004).

**Table 2: Locations for Target and Element Events, as Determined by Servicio Sismológico Nacional (SSN), and Focal Mechanisms for Both Events, as Determined by Central Moment Tensor (CMT[1])**

| | Target Event | Element Event |
|---|---|---|
| **Origin time (local time)** | 22/01/2003 02:06 GMT | 19/11/2006 06:59 |
| **Hypocentral location (latitude, longitude, and depth)** | (18.60°N, 104.22°W, 26 km) | (18.46°N, 104.49°W, 18 km) |
| **Magnitude $M_W$** | 7.5 | 5.5 |
| **Focal mechanism (strike, dip, rake)** | (308°, 12°, 110°) | (300°, 21°, 74°) |

By using the accelerograms, we extracted the flat levels of displacement spectra for low frequencies and the flat levels of acceleration spectra for high frequencies for the MANZ station. Based on the analysis of these spectra, we discovered that the flat levels of acceleration spectra were between 1.0 and 10 Hz. Also, corner frequencies (i.e., the values of $f_c$) were obtained for the element and target events.

For the spectral analysis, background noise data was collected at four sites: MANZ, CASA, CAMPOS, and LAGO. Figure 3 shows the Google satellite image of the area and the locations of sites. In Table 3 the details of geographic locations and soil classifications are provided.


Fig. 3 Google satellite image of the area and the locations of sites (shown by the triangles) for the spectral analysis; background noise data was collected at four sites: MANZ (soil), CASA (rock), CAMPOS (soil), and LAGO (soil)

**Table 3: Details of Geographic Locations and Soil Classifications for the Four Sites Considered to Collect Background Noise Data for the Spectral Analysis**

| Station | Latitude | Longitude | Time of Record (s) | Type of Soil |
|---|---|---|---|---|
| CAMPOS | 19.0289° | −104.316° | 31417 seg (8.7 hrs) | Soil |
| CASA | 19.0236° | −104.325° | 35553 seg (9.87 hrs) | Rock |
| MANZ | 19.027710° | −104.318504° | 34820 seg (9.67 hrs) | Soil |
| LAGO | 19.030273° | −104.318581° | 36001 seg (10.00 hrs) | Soil |

Among the four sites considered, CASA is located in a rocky outcrop, and the other three in soft soils. We used two earthquake records, in addition to the above background time series, and those correspond to the target and element events considered above; the epicenters of both events were close to each other (see Figure 2). The record lengths of the two ground motions were 2545 and 2565 sample points per channel respectively, and both ground motions were recorded at the soft-soil site at MANZ.

The background noise data was collected by using the Kinematrics K2 recorders of 24-bit ADC converter, with integrated accelerometers of 2*g* at full scale, and three additional recording channels with externally connected Guralp-40T sensors. The sampling frequency was 100 Hz, together with unit gain.

Segments of ground motions for the background noise were plotted for visual inspection. The visual inspection was mainly concerned with the selection of desired types of signals for use in the frequency domain analysis, which consisted of power spectral density (PSD) estimations of the time series. For this we avoided those time periods which might contain signals due to seismic events and other transient signals. Significant differences in background noise levels were evident between the horizontal and vertical components.

For unit conversion from digital units (DU) to physical units of the background noise ground motion in velocity (in m/s), we used the Guralp-40T sensor conversion factor of 2000 V/m/s over the frequency band of 0.03–50 Hz. The D.C. offset was removed from the selected time series. The plots of the prepared time-series segments were useful to double-check the amplitude levels of the recorded background noise ground motions by comparison with the published data from similar studies. In computing PSD from the background noise, more stable and reliable PSD estimates were obtained with the use of larger ensembles of time series in the averaging process. For the background-noise analysis, we used time series of one hour length, which contained 360,000 sample points per channel. We excluded, either manually or by an implemented automatic algorithm, transient signals, if any, in obtaining the PSD spectra.

## METHOD

The method used to model the target event (i.e., Tecomán earthquake of January 22, 2003 in this study) requires a small-magnitude earthquake (i.e., the earthquake of November 11, 2006 in this study) with its hypocenter near the hypocenter of the target event. On applying the synthetic method for the $\omega^{-2}$ spectral model, as proposed by Aki (1967), we obtain the necessary number of subevents, $N^3$, from the relationship between the seismic moments of the target event (to be simulated) and the element event, which is used as the empirical Green's function. When $N^3$ is equal to the number of sub-faults in the directions of strike (i.e., $N_x$), dip (i.e., $N_w$), and time (i.e., $N_t$), i.e.,

$$N^3 = N_x \times N_w \times N_t \tag{1}$$

it is necessary to find the parameter $N$ used to scale the fault area of main event. Since it is divided into $N \times N$ sub-faults, $N^3$ is obtained as

$$\frac{\bar{U}_0}{\bar{u}_0} = \frac{M_0}{m_0} = N^3 \tag{2}$$

where $\bar{U}_0$ and $\bar{u}_0$ are the flat levels of the displacement Fourier spectra for the target and element events, respectively; and $M_0$ and $m_0$ are the seismic moments of the target and element events, respectively. The relationship for high frequency is given by

$$\frac{\bar{A}_0}{\bar{a}_0} = \left(\frac{M_0}{m_0}\right)^{1/3} = N \tag{3}$$

where $\bar{A}_0$ and $\bar{a}_0$ are the flat levels of the acceleration Fourier spectra of the target and element events, respectively.

Thus, the synthetic motion for the target event, $A(t)$, is given by that for the element event, $a(t)$, by using the following equations:

$$A(t) = \sum_{i=1}^{N_x} \sum_{j=1}^{N_w} \frac{r}{r_{ij}} F\left(t - t_{ij}\right) a(t) \tag{4}$$

$$F_{ij}\left(t-t_{ij}\right)=\delta\left(t-t_{ij}\right)+\frac{1}{n'}\sum_{k=1}^{(N-1)n'}\delta\left(t-t_{ij}-\frac{(k-1)\tau}{\left(N-1\right)n'}\right) \tag{5}$$

where $n'$ is an appropriate value to eliminate spurious periodicity, $r$ is the distance from the station to the element-event hypocenter, $r_{ij}$ is the distance from the station to the subfault ($i, j$), and $t_{ij}$ is the delay time of the rupture from the starting point ($i, j$) to the site of observation.

To use the element-event waveform with a different stress drop, the empirical Green's function formulation is modified by introducing a factor $C$ that serves to correct the difference between the stress drops of the target and element events:

$$C=\Delta\sigma_{SP}/\Delta\sigma_{R} \tag{6}$$

The spectral levels of Equations (2) and (3) are affected by the same factor $C$ as follows:

$$\bar{U}_0/\bar{u}_0=CN'^3 \tag{7}$$

$$\bar{A}_0/\bar{a}_0=CN' \tag{8}$$

Further, Equation (4) is amended by replacing $a(t)$ with $Ca(t)$ and $N$ with $N'$ as

$$A(t)=\sum_{i=1}^{N'}\sum_{j=1}^{N'}\frac{r}{r_{ij}}F(t_{ij})a(t) \tag{9}$$

For the spectral analysis, the data processing has followed the rules of Fourier analysis, as described, for example, in the books by Kanasewich (1981), Oppenheim and Shafer (1975), and Bendat and Piersol (1971). The PSD estimates for the background noise measurements have been obtained by using time series of 3600 s (with 360,000 samples) and by averaging 351 sub-segments of 1024 points each and with an overlap of 75% in length. The time-series lengths of 25.45 and 25.65 s were used for the two earthquakes with $M_W$ = 7.5 and 5.5, respectively. The same segment length and overlap, as those used for the background noise, were used for the earthquake time series. For both kinds of records, the mean value of each sub-segment was removed and a Hanning window was applied to each sub-segment. The averaged PSD estimates were then normalized by multiplying with the frequency increment $\Delta f$ and the amplitude scaling factor (which equals two due to the symmetry property of DFT) and by dividing by the number of data points, $N$. Finally, after the instrument correction was applied, the spectral amplitudes were transformed to the units of acceleration. The $\omega^2$ factor was applied for acceleration conversion from the velocity records. By means of using weak (for microtremors), moderate (for the earthquake of $M_W$ = 5.5), and strong (for the earthquake of $M_W$ = 7.5) ground motions, $H/V$ spectral ratios (HVSPR) were computed between each horizontal component and the vertical component in order to identify empirically whether local site effects were present. As indicator of the above, the HVSPR spectra were inspected for energy concentration at particular frequencies within the frequency interval of 1–10 Hz. This procedure is an alternate way to provide an empirical evidence to accept or reject the hypothesis that at the MANZ site, nonlinear local site effects were significant. It should be pointed out that an evidence of nonlinearity is shown by significant decreases in the frequencies of peak spectral ratios, corresponding to material softening, as the amplitude is increased. The observed shifts in peaks do not show any significant contributions in the frequency range of 1–10 Hz. These results provide constraints for future numerical modeling studies on strong ground motions during earthquakes.

## MODEL

Since the stress drop is different for the target and element events, the above method was applied (see Equations (4)–(6)). Thus, we obtained the parameters, $N'$ = 8 and $C$ = 1.08. We also need to assume and vary some other parameters in order to simulate the acceleration records. Those parameters are rupture velocity, rise time, and the point where the rupture starts, among others.

On applying this modeling, we found little sensitivity of the synthetics to the rise-time variations. On the other hand, we found high sensitivity of the synthetics to the rupture-velocity variation, and to the size of SMGA and its location inside the fault plane. By applying this method, we generated several models in which these parameters were varied. The corresponding iterations can be classified in four stages: the models with one, two, three, and four SMGAs. As shown in Figure 4, the SMGA area is divided into four parts and these areas are positioned on each point into the dislocation area until the entire area is covered. Each variation in the position of SMGA corresponds to single iteration. In this process, the rupture velocity, rise time, and radiation pattern were varied. The size of SMGA changes in the strike or dip direction, according to the azimuth of the station or stations that had poor adjustment. In others, the location of SMGA was varied by moving it close to the hypocenter and by increasing its rupture velocity, while trying to compact or expand the packets of some waves within the trace. Major iterations were made by taking into consideration the best adjustments in the first, second and third previous stages (i.e., the process based on discrimination and optimization to determine the best model). The parameters and tests described above were applied in each one of the three stages. The best model for each stage was determined by minimizing the residuals between the synthetic and observed waveforms.

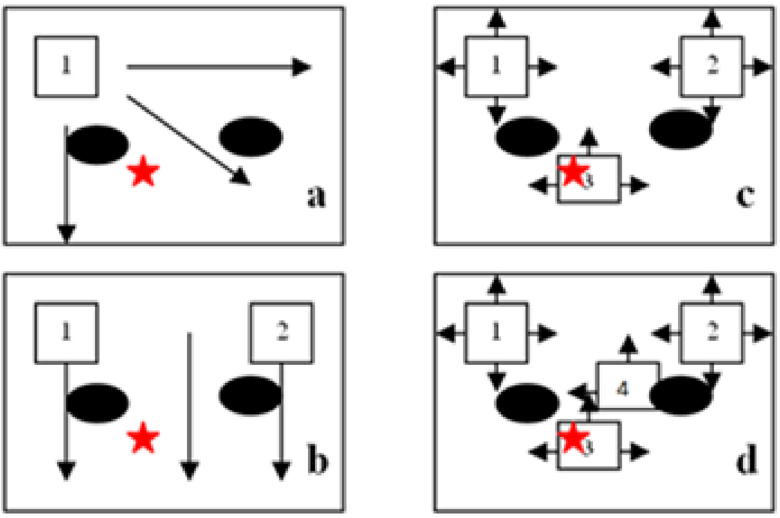


Fig. 4 Process of modeling in four stages for the Tecomán earthquake (oval: asperities of the dislocation model found by Yagi et al. (2004); star: epicenter of the Tecomán earthquake; numbered squares represent the SMGAs used in each stage; arrows show the direction of movement of each square searching the best residuals)

In the beginning, we modeled the target event by attempting to adjust the synthetics for the local station MANZ, and then by applying it to the regional stations. In the same way, some models were generated primarily by adjusting those to the waveforms for regional stations and then by applying those to the local station MANZ.

## RESULTS

In the first stage, we modeled the target event by using one SMGA and by adjusting it to the source nearest to the MANZ station. The location of SMGA was varied around the fault plane. The best models were generated during the first stage when the only SMGA was located in the zones identified as SMGA "A" and SMGA "B" (see Figures 5(a) and 5(b)).

The first best-fit location (i.e., SMGA "A") was obtained when the target event was modeled with a SMGA of 59.16 km$^2$ and $V_r$ = 2.1 km/s (see Table 4), located at 16.68 km SW from the hypocenter. The sum of residual values for each of the components in velocity, acceleration, and displacement for both models, which appear in Table 5, show a better match in the three components when modeling is done with one SMGA (i.e., SMGA "B") of 59.16 km$^2$ and $V_r$ = 2.1 km/s (see Table 4), located at 21.27 km NE from the hypocenter (see Figure 5(a)).

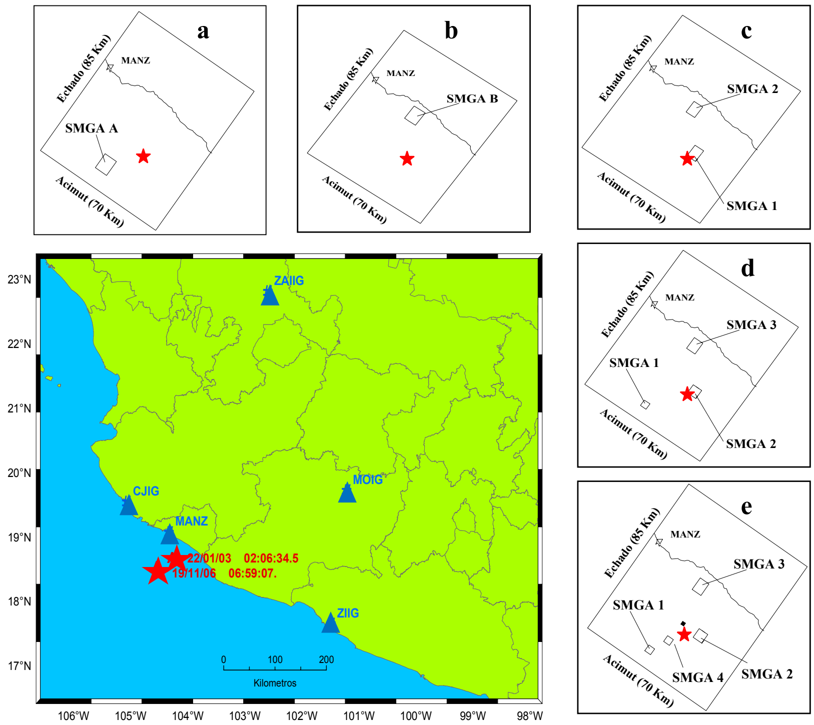


Fig. 5 Models with minor residuals generated in the EGFM process by using one SMGA (see (a) and (b)) and two, three and four SMGAs (see (c), (d) and (e), respectively)

**Table 4: Locations and Areas of SMGAs for the Four Models Generated, with One, Two and Three SMGAs, Respectively, Where $V_r$ is the Rupture Velocity**

| Model | SMGA | Length (km) | Width (km) | Area ($km^2$) | Starting Point of Rupture with Relation to Hypocenter | $V_r$ (km/s) |
|---|---|---|---|---|---|---|
| 1 | 1 | 8.60 | 6.88 | 59.168 | 16.68 km SW | 2.1 |
| 2 | 1 | 8.60 | 6.88 | 59.168 | 21.27 km NE | 2.1 |
| 3 | 1 | 5.16 | 6.88 | 35.5008 | 10.48 km SE | 2.1 |
| | 2 | 5.16 | 6.88 | 35.5008 | 20.07 km NE | 2.9 |
| 4 | 1 | 3.44 | 3.44 | 11.83 | 20.75 km SW | 2.1 |
| | 2 | 5.16 | 5.16 | 26.62 | 10.24 km SE | 2.9 |
| | 3 | 6.88 | 5.16 | 35.50 | 20.16 km NE | 2.1 |
| 5 | 1 | 3.44 | 3.44 | 11.83 | 20.75 km SW | 2.1 |
| | 2 | 5.16 | 5.16 | 26.62 | 10.24 km SE | 2.9 |
| | 3 | 6.88 | 5.16 | 35.50 | 20.16 km NE | 2.1 |
| | 4 | 3.44 | 3.44 | 11.83 | 18.45 km SW | 2.9 |

Figure 6 (for SMGA "A") shows the comparisons between the observed records (see the bottom curves) and synthetic records (see the top curves) for the three components in velocity, acceleration, and displacement in the first stage.

In the second stage, the Tecomán earthquake of 2003 is modeled with two SMGAs. Here, we also adjusted the synthetic record to those recorded at the nearest station to the source (i.e., MANZ). The locations of the two SMGAs were varied within the fault plane. The model with the best fitting was applied to the records obtained from the regional stations, CJIG, MOIG, ZAIG, and ZIIG. These four regional stations provide a good azimuthal coverage around the earthquake. The residual values for three components in velocity, acceleration, and displacement presented in Table 5 show that the best fitting was obtained for the model shown in Figure 5(c). This model consists of one SMGA of 35.50 $km^2$ located at 10.48 km SE from the hypocenter, and another SMGA of 35.50 $km^2$, located at 20.07 km NE from the hypocenter as shown in Table 4.

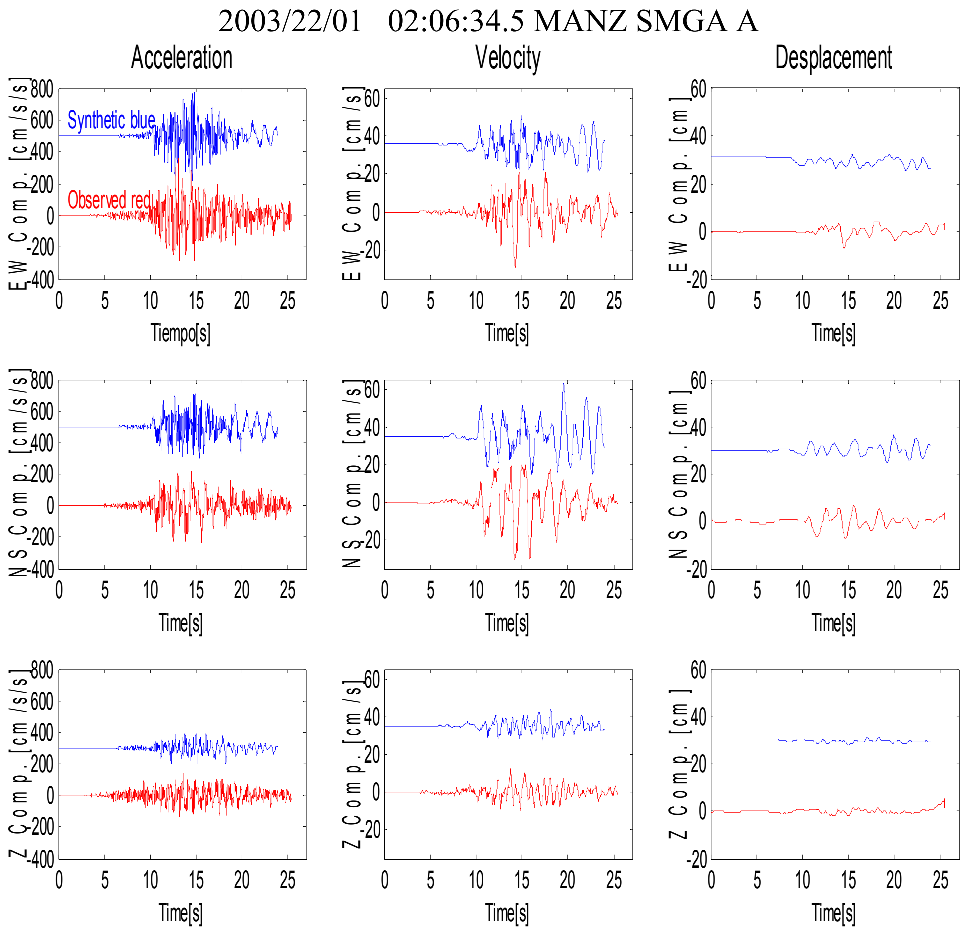


Fig. 6 Simulation for MANZ station with one SMGA (top: synthetic; bottom: observed; columns from left to right: acceleration, velocity, and displacement; rows from top to bottom: EW, NS, and Z components)

In the third stage, we modeled the target event with three SMGAs by adjusting the synthetic records to those recorded at the source of the nearest station (i.e., MANZ). The locations of these three SMGAs were varied within the fault plane. The best-fit model was also applied to the records from the regional stations, CJIG, MOIG, ZAIG and ZIIG. Table 5 shows that the best fitting was obtained for the model presented in Figure 5(d). This model consists of three SMGAs. One of them is 11.83 km$^2$, located 20.75 km SW from the hypocenter; another has 20.62 km$^2$, located 10.24 km SE from the hypocenter; and the third one has 35.50 km$^2$, located 20.16 km NE from the hypocenter. The features of this model are also listed in Table 4.

**Table 5: Sum of Residuals for EW, NS and Z Components in Acceleration, Velocity and Displacement**

| **Models for MANZ Station** | **Residual** | | |
|---|---|---|---|
| | **Acceleration** | **Velocity** | **Displacement** |
| One SMGA (SMGA "A") | 108.75 | 29.62 | 9.55 |
| One SMGA (SMGA "B") | 23.00 | 12.50 | 7.05 |
| Two SMGAs | 6.13 | 17.32 | 5.63 |
| Three SMGAs | 4.79 | 3.36 | 4.59 |
| Four SMGAs | 6.82 | 6.92 | 10.44 |
| **Models for Regional Stations, CJIG, MOIG, ZAIG, ZIIG** | **Average Residual** | | |
| | **Acceleration** | **Velocity** | **Displacement** |
| Two SMGAs | 49.00 | 24.79 | 16.82 |
| Three SMGAs | 5.33 | 4.51 | 4.10 |
| Four SMGAs | 41.49 | 74.96 | 63.51 |

Figures 7, 8, 9(a), 10 and 11 show the comparisons between the observed records (see the bottom curves) and synthetic records (see the top curves) for the three components in velocity, acceleration, and displacement at the MANZ, CJIG, MOIG, ZAIG and ZIIG stations, respectively, for the best model with three SMGAs.

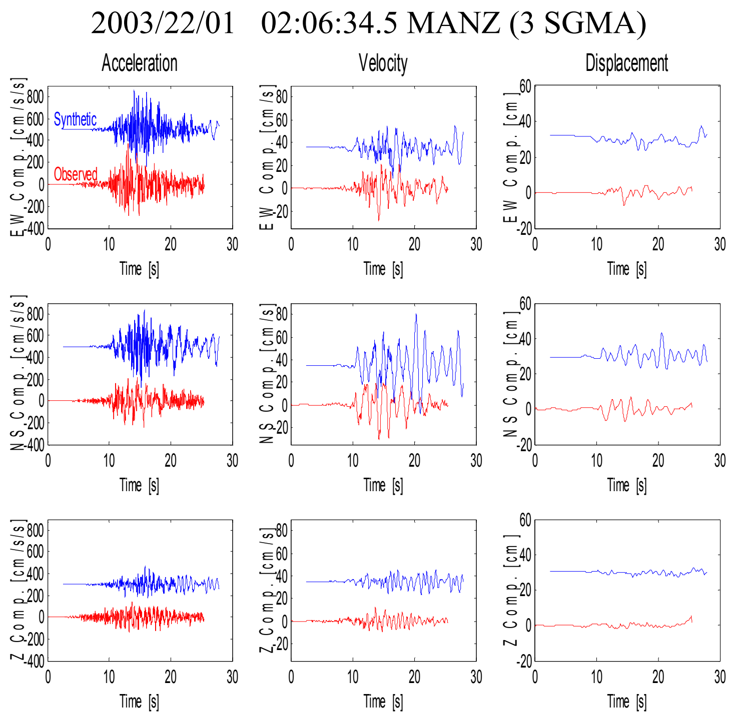


Fig. 7 Simulation for MANZ station with three SMGAs (top: synthetic; bottom: observed; columns from left to right: acceleration, velocity, and displacement; rows from top to bottom: EW, NS, and Z components)

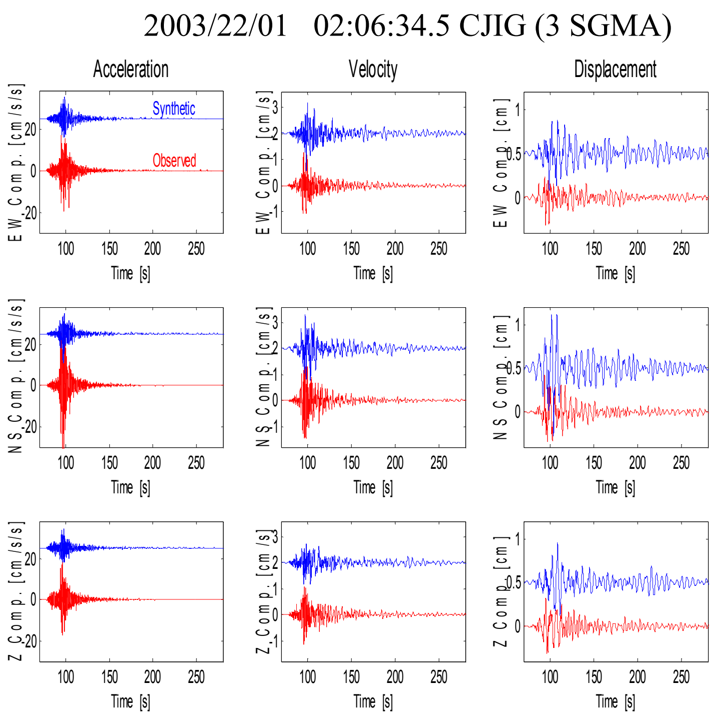


Fig. 8 Simulation for CJIG station with three SMGAs (top: synthetic; bottom: observed; columns from left to right: acceleration, velocity, and displacement; rows from top to bottom: EW, NS, and Z components)

2003/22/01 02:06:34.5 MOIG (3 SGMA)

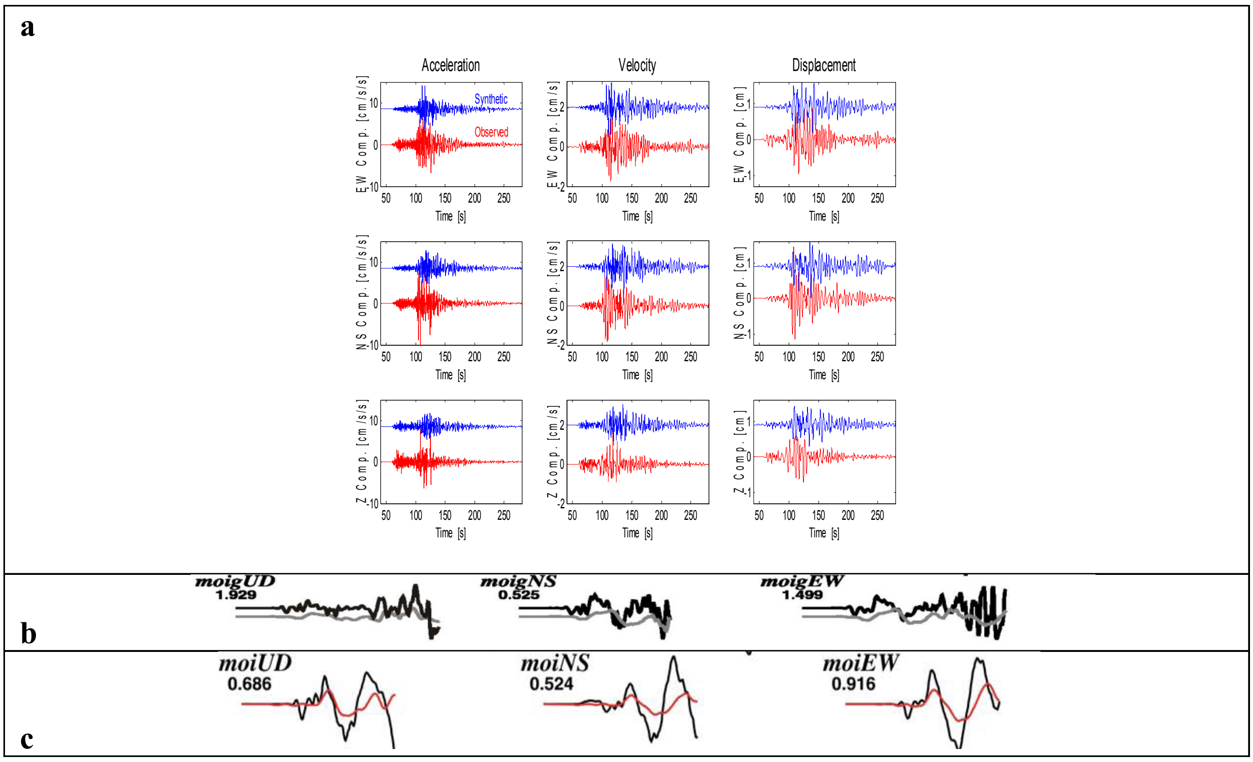


Fig. 9 (a) Simulation for MOIG station by the model with three SMGAs (top: synthetic; bottom: observed; columns from left to right: acceleration, velocity, and displacement; rows from top to bottom: EW, NS, and Z components); (b) Synthetic and observed records for the Tecomán earthquake at MOIG station from Yagi et al. (2004); (c) Synthetic and observed records for the Tecomán earthquake at MOIG station from Quintanar et al. (2010)

2003/22/01 02:06:34.5 ZAIG (3 SGMA)

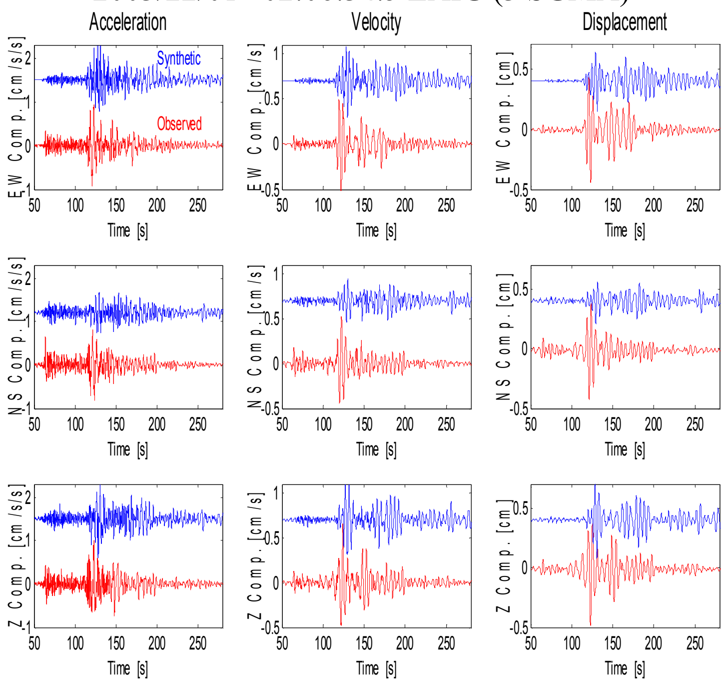


Fig. 10 Simulation for ZAIG station with three SMGAs (top: synthetic; bottom: observed; columns from left to right: acceleration, velocity, and displacement; rows from top to bottom: EW, NS, and Z components)

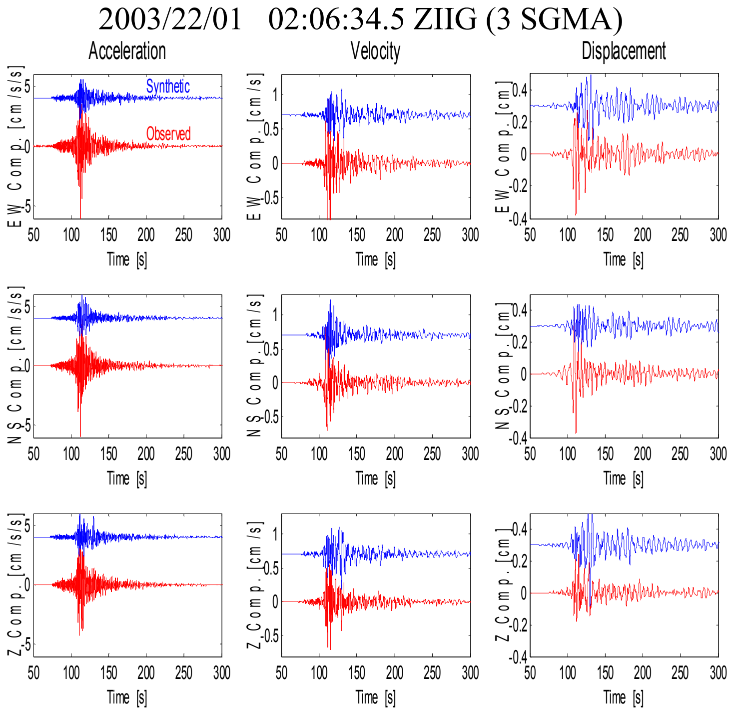


Fig. 11 Simulation for ZIIG station with three SMGAs (top: synthetic; bottom: observed; columns from left to right: acceleration, velocity, and displacement; rows from top to bottom: EW, NS, and Z components)

Figures 12–16 show the comparisons between the observed and synthetic Fourier spectra for the three components in velocity, acceleration, and displacement at the MANZ, CJIG, MOIG, ZAIG and ZIIG stations, respectively, for the best model with three SMGAs.

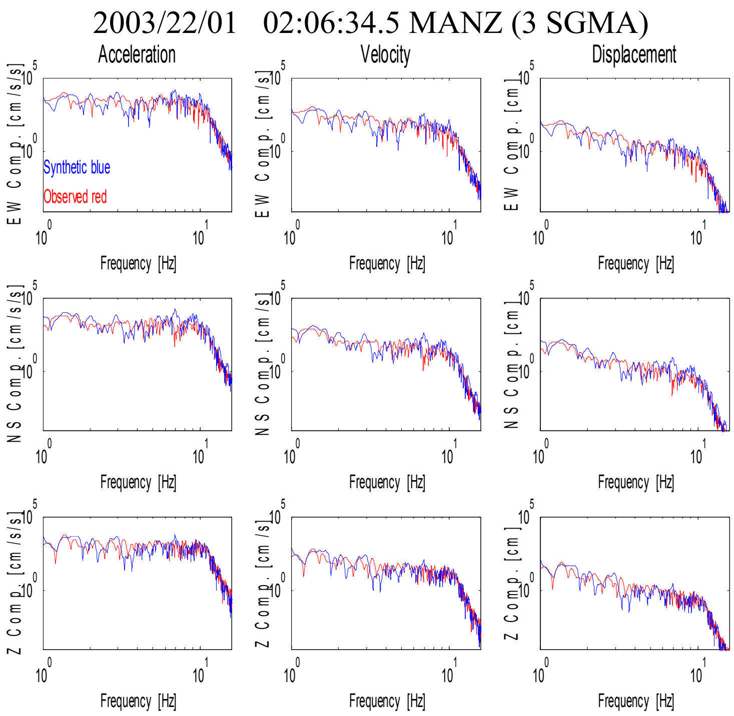


Fig. 12 Fourier spectra for MANZ station with three SMGAs (columns from left to right: acceleration, velocity, and displacement; rows from top to bottom: EW, NS, and Z components)

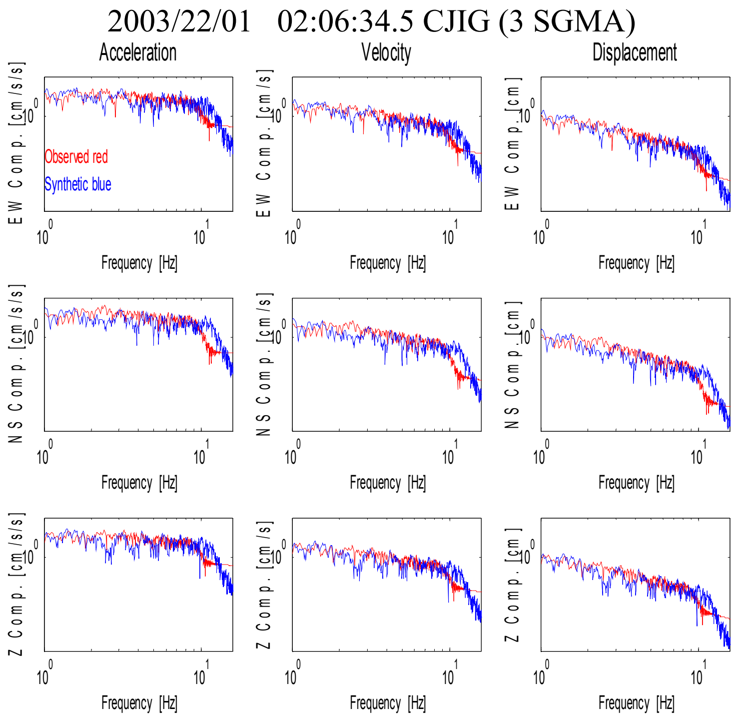


Fig. 13 Fourier spectra for CJIG station with three SMGAs (columns from left to right: acceleration, velocity, and displacement; rows from top to bottom: EW, NS, and Z components)

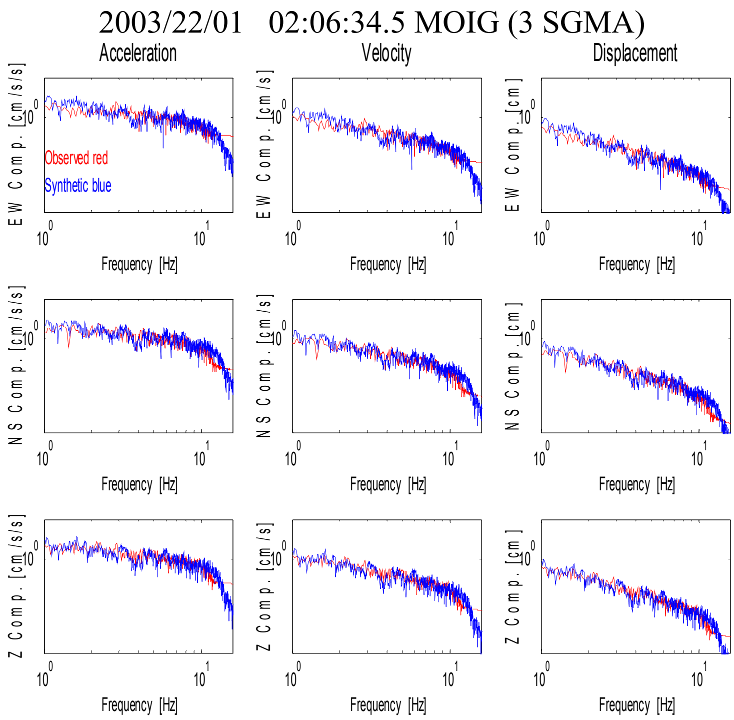


Fig. 14 Fourier spectra for MOIG station with three SMGAs (columns from left to right: acceleration, velocity, and displacement; rows from top to bottom: EW, NS, and Z components)

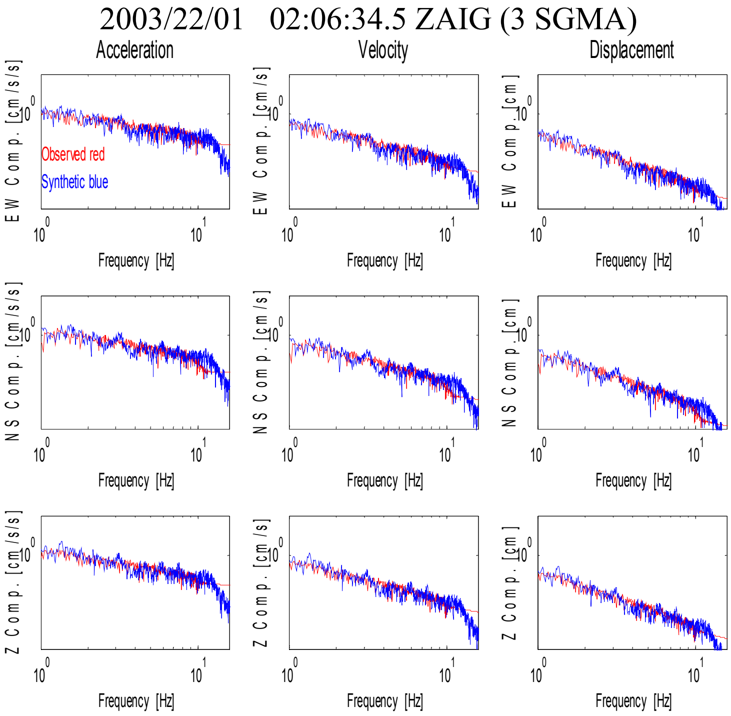


Fig. 15 Fourier spectra for ZAIG station with three SMGAs (columns from left to right: acceleration, velocity, and displacement; rows from top to bottom: EW, NS, and Z components)

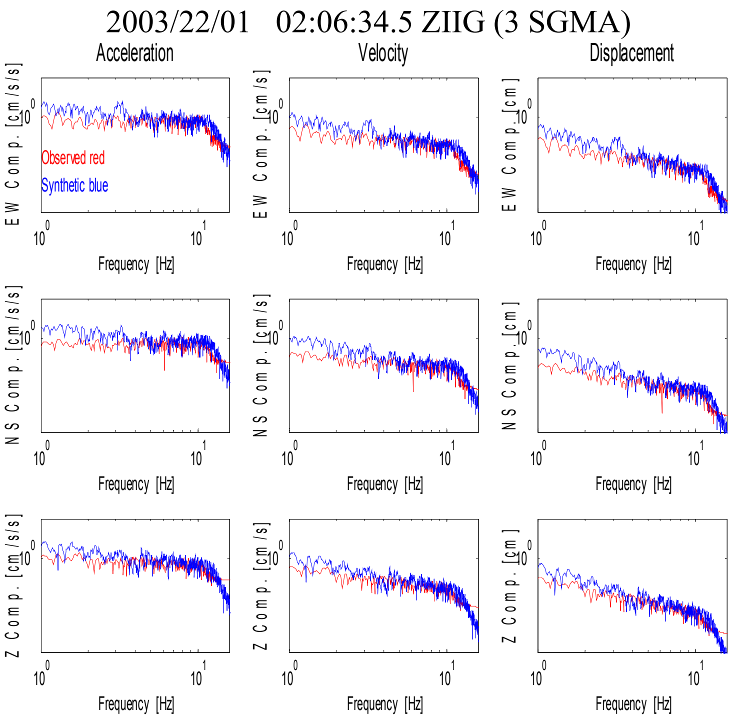


Fig. 16 Fourier spectra for ZIIG station with three SMGAs (columns from left to right: acceleration, velocity, and displacement; rows from top to bottom: EW, NS, and Z components)

Table 4 shows the best fit obtained for the model with four SMGAs. This model consists of the SMGA of 11.83 km$^2$, located 20.75 km SW of the epicenter; SMGA of 20.62 km$^2$, located 10.24 km SE of the epicenter; SMGA of 35.50 km$^2$, located 20.16 km NE of the epicenter; and SMGA of 11.83 km$^2$ at 18.45 km SW of the epicenter.

For the spectral analysis conducted for the MANZ site, HVSPR were computed between each horizontal component and the vertical component in order to identify the local site effects using the weak (for microtremors), moderate (for the earthquake of $M_W$ = 5.5), and strong (for the earthquake of $M_W$ = 7.5) ground motions. Further, an analysis was conducted to provide an empirical evidence to support the hypothesis that for the frequency range of 1–10 Hz, nonlinear effects are significant at the MANZ soft soil site. In Figure 17, both $H_{NS}/V$ and $H_{EW}/V$ spectral ratios (SPR) are presented. In both graphs, the HVSPR of the strong and the moderate earthquake ground motions, as well as those for the microtremor ground motions, are also plotted for an easy viewing of the frequency shift to lower values. On inspecting, from the weak motions (see the dash-dot, dashed, and thick-dotted lines, all with maximum amplitude peaks around 0.7 Hz) to the moderate (see the thin solid line) and strong (see the dashed thin line) ground motions, two maximum amplitude peaks are clearly seen. One peak each can be observed at the frequencies of 4 and 3 Hz, respectively, for the $H_{NS}/V$ SPR, and the second-maximum amplitude peaks for both earthquakes are located between 0.68 and 0.59 Hz. The $H_{EW}/V$ SPR for the moderate earthquake ground motion exhibit a wide frequency range of 0.5–0.7 Hz, and the second-maximum amplitude peak for the strong earthquake ground motion is located between 0.8 and 0.9 Hz. On comparing the dotted line, which belongs to the CASA site (located on a rocky outcrop), with all other lines, the local site effects become clearly evident; however, the nonlinear response behavior is not evident. Details of the station identification and the corresponding line are provided in the caption of Figure 17.

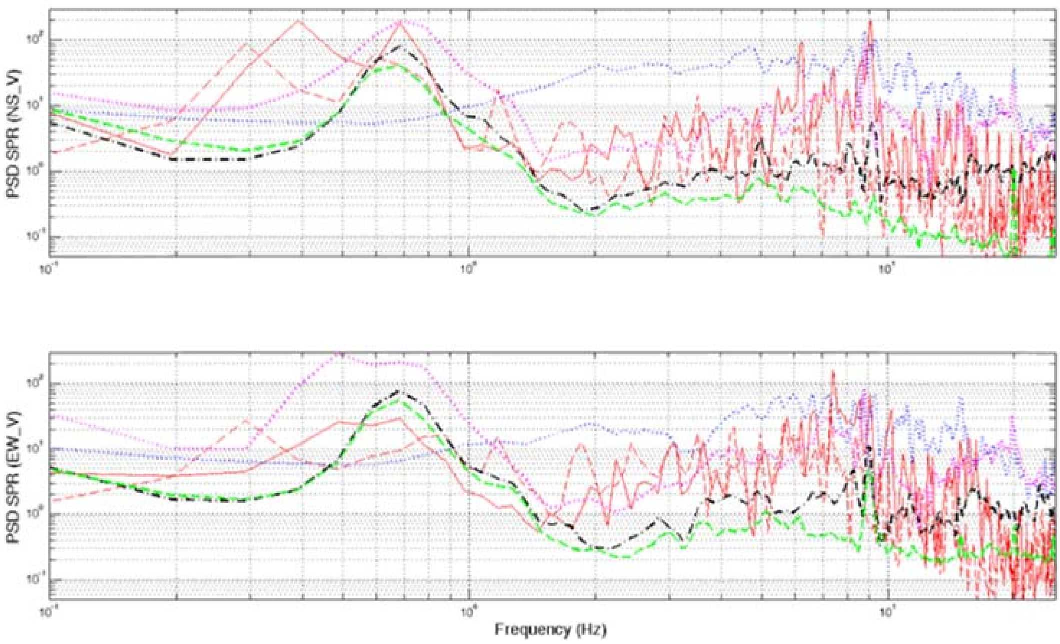


Fig. 17 Spectral ratios of microtremors, moderate and strong ground motions (top: $H_{NS}/V$ SPR; bottom: $H_{EW}/V$ SPR; the dashed-thin and solid-thin lines are for the strong (for the earthquake of $M_W$ = 7.5) and moderate (for the earthquake of $M_W$ = 5.5) ground motions, respectively, both recorded at the MANZ soft soil site; the small-dots line is for the CASA site on rocky outcrop; the dash-dot and dashed lines correspond to the CAMPOS and LAGOS soft-soil sites, respectively; the large-dots line belongs to the MANZ soft-soil site)

As mentioned before, the spectral analysis was done for the MANZ site to identify if significant nonlinear effects were present in the frequency band of 1–10 Hz. This was not necessary for the other four sites because those are located on hard rocks.

The non-significant effect of the nonlinear response of soft soils at the MANZ site is now well supported by the inspection of the frequency shift associated with no significant amplitude changes, as the HVSPR have demonstrated, at least for the frequency band of 1–10 Hz. On the other hand, the local site effects of the soft soils of our study area are also confirmed on comparing the HVSPR of the CASA site (located on a rocky outcrop) with those of the rest of the sites, which are located on soft soils.

As part of this investigation, we quantified individual and average characteristics of SMGA, rupture area, dislocation time and rise time. These values are related with the seismic moment of these events, $M_0$ (= $1.6\times10^{20}$ N-m); the results obtained were compared with the relationships proposed by Somerville et al. (2002) for the subduction earthquakes (see Table 6). These relationships involved the seismic moment $M_0$ and the inner and outer parameters. The outer parameters are fault area, dislocation time, and rise time. The inner parameters are the total area of all SMGAs, the area of bigger SMGA, the radius of bigger SMGA, and the distance from hypocenter to the nearest SMGA.

**Table 6: Comparison between the Relationships Proposed by Somerville et al. (2002) for Subduction Earthquakes and the Results of This Study**

| | This Study (A) | Somerville et al. (2002) (B) | Ratio (= A/B) |
|---|---|---|---|
| Rupture Area | 5.95E+03 | 8.01E+03 | 7.43E-01 |
| Dislocation Time | 3.00E+01 | 4.80E+00 | 6.25E+00 |
| Rise Time | 4.00E-01 | 2.38E+00 | 1.68E-01 |
| Total Area of SMGA | 7.40E+01 | 2.00E+03 | 3.70E-02 |
| Area of the Largest SMGA | 3.55E+01 | 1.30E+03 | 2.73E-02 |
| Radius of the Largest SMGA | 3.36E+00 | 2.20E+01 | 1.53E-01 |
| Hypocentral Distance of the Nearest SMGA | 1.37E+01 | 2.10E+01 | 6.53E-01 |

The results of these comparisons show that the relationships between $M_0$ and rupture area, and $M_0$ and hypocentral distance to the nearest asperity, adjust moderately well. However, this is not the case for the rest of the relationships described above.

## DISCUSSION

The best model obtained consists of three SMGAs of maximum dislocation. The process of finding the best adjustment mentioned above generated four different models (of one, two, three, and four SMGAs). This process clearly shows that the residual values for the local station MANZ decreased progressively (see Table 5). First, on modeling the target event with a single SMGA and on varying the location from Position A (with residual acceleration = 108.75) to Position B (with residual acceleration = 23.00), the residual value was reduced. The residual value improved significantly on modeling with two SMGAs (with residual acceleration = 6.13), at the locations shown in Figure 5(c). The best adjustment was obtained when the target event was modeled with three SMGAs, at the locations shown in Figure 5(d) (with residual acceleration = 4.79). However, when modeled with four SMGAs (see Figure 5(e)), the best model generated a residual of 6.82 and thus the residual increased. The poor adjustment with four SMGAs (which directly involves an increase in the area of SMGA) is evident on comparing the synthetic and observed records of Figure 18. The components of velocity and displacement have a similar behavior.

The model process includes the variation of other parameters like that of $V_r$ and rise time. The parameters with major weights in the model are the number, sizes and locations of SMGAs. The optimal model is a combination of all these parameters. In order to find a minor residual that could increase the total area of SMGA, it is necessary to consider that the method used considers displacement in SMGA to be uniform. This is not completely correct. Displacements can vary inside an SMGA and can take significant weights in the fitting. Additionally, it is necessary to take into consideration the quantity and quality of the available data. Nozu and Irikura (2008) used the same method to model the Tokachi-Oki 2003 earthquake. The K-NET and KiK Japan networks recorded this earthquake and aftershocks at 600 accelerographic stations. Forty stations with better azimuthal coverage were chosen for the modeling. In contrast, in this study we have only five stations, only one near the source (i.e., the MANZ station, located at a distance of 53.82 km to the hypocenter), and the other four with distances ranging from 132 km (for CJIG) to 494 km (for ZAIG). Despite the limited quantity and quality of available data, the comparison of residuals and the fitting between synthetic and observed records and their Fourier spectra show that residuals were considerably minimized.

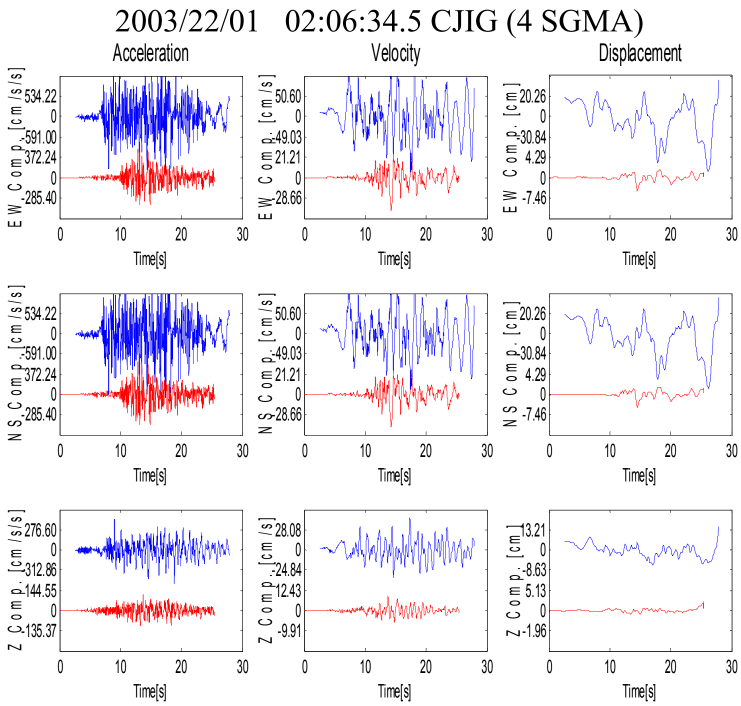


Fig. 18 Simulation for MANZ station with four SMGAs (columns from left to right: acceleration, velocity, and displacement; rows from top to bottom: EW, NS, and Z components; synthetic waveforms overestimate the observed waveforms)

Figure 9(a) shows, for the MOIG station, the adjustment between the synthetic and observed records at high frequencies, as obtained in this study for the Tecomán earthquake. Figures 9(b) and 9(c) show the adjustments at low frequencies obtained from the inversions of Yagi et al. (2004) and Quintanar et al. (2010), respectively. The poor adjustment at low frequencies for this station is attributed to the lack of cortical information for this site. Our results show contrasting results on applying the EGFM.

The final model with three SMGAs, having presented the best adjustment in residuals, also gives a close resemblance with the dislocation model found by Yagi et al. (2004) (see Figure 19), who reported that the rupture process is divided in three stages. In the first stage, the rupture starts near the hypocenter. In the second stage, the rupture propagates towards the southeast and breaks the asperity A, which is 15 km away from the starting point of the rupture; at the same time, a third stage occurs in which the rupture spreads to the northeast and breaks the asperity B, which is 25 km away from the starting point of the rupture. SMGA “1” in our model is located at 1.72 km from the center of asperity A, as reported by Yagi et al. (2004); SMGA “2” is located at 5.16 km from the hypocenter, and SMGA “3” is located at the same place as the asperity B, as reported by Yagi et al. (2004).

In Table 5 we can observe that the stations MANZ and ZAIG have adjustments better than 90% in the accelerations for the WE and Z components, and that adjustments in velocity are better than 70% for the same components; adjustments in acceleration, velocity and displacement for the NS component at the same stations are less than 60%. In the same way, adjustments in acceleration for the three components at the remaining stations (i.e., CJIG, MOIG and ZAIG) are less than 60%.

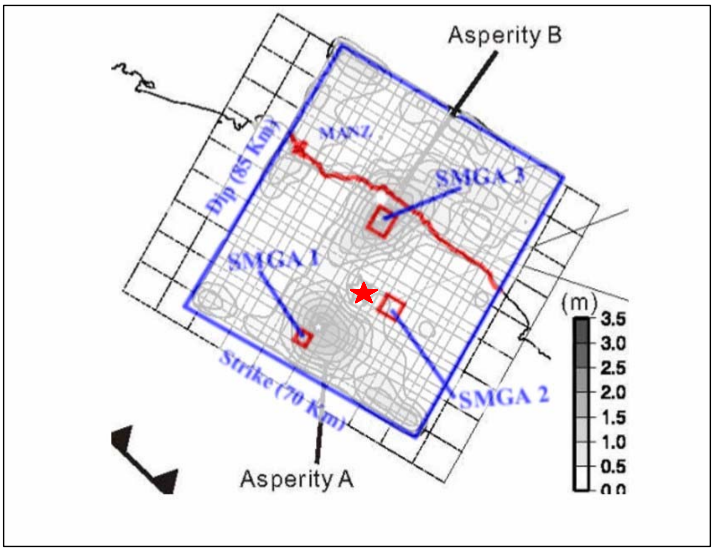


Fig. 19 Comparison between the dislocation model obtained by Yagi et al. (2004) and the positions and sizes of the SMGAs generated with our model

Singh et al. (2003) show that the Tecomán earthquake of 2003 generated directivity in the direction of the station COIG, which then spread to Colima city and to the northeast with an azimuth of 38ºNE. The stations which presented the best adjustments in acceleration, velocity and displacement (i.e., the stations MANZ and ZAIG) seem to fit this direction of rupture propagation of the earthquake. The stations, where the adjustments were smaller that 50% (i.e., the stations CJIG, MOIG and ZIIG), seem to be outside this direction. The Tecomán earthquake of 2003 originated in the center of El Gordo graben and spread in the direction mentioned above within the Colima State. The peak values in accelerations, velocities, and displacements at the stations that are outside the direction of rupture propagation of the earthquake might be explained due to a phenomenon wherein the boundaries of the graben operate as borders and the seismic waves undergo diffraction, reflection, and refraction at those borders. This implies that the direction, in which the waves propagate after arriving at this border, depends on their initial trajectory. This further means that the direction of wave propagation depends on the location of the earthquake within the graben. Thus, in order to reproduce waveforms at the stations outside the graben (perpendicular to the direction of propagation), the locations of the target and element events should be as close as possible. However, the distance between these two earthquakes is 36 km. The adjustments in the peak values in acceleration, velocity, and displacement for the stations that are outside the direction of rupture propagation are not clear in comparison with the good adjustments for the stations that are located in this direction.

From the interpretation of the results of the spectral analysis, we conclude that the nonlinear effects of soft soils were not significant at the MANZ site. This is well supported by the mild frequency shift seen in the HVSPR plots, at least for the frequency band of 1–10 Hz. On the other hand, the local site effects of soft soils in our study area are also confirmed on comparing the HVSPR of the CASA site (on rocky outcrop) with those of the rest of the sites (located on soft soils).

We applied the relationships proposed by Somerville et al. (2002) for subduction earthquakes, which related seismic moment with some source parameters, as well as seismic moment with some characteristics of the SMGA generated in this study (see Table 6). The results show that the relationship between $M_0$ and hypocentral distance to the nearest asperity gets adjusted by 53% to the value proposed by Somerville et al. (2002). The number of SMGAs in our model is 3, which is close to 2.4 proposed by Somerville et al. (2002). However, when the relationship between $M_0$ and rupture area is compared, the area obtained in the inversion made by Yagi et al. (2004) is only 27% of the value proposed by Somerville et al. (2002). For the same relation, Quintanar et al. (2010) obtained an area of 22.40% of the value proposed by Somerville et al. (2002). Garduño (2006) applied the same relationships to her model obtained for the July 15, 1996 earthquake in the Guerrero State coast. When she applied the relationship between $M_0$ and rupture area, the obtained value was only 3% of that proposed by Somerville et al. (2002). For the rest of the relationships the values obtained with our model are usually less than 15%

of those obtained by Somerville et al. (2002). The results obtained by Yagi et al. (2004), Quintanar et al. (2010), Garduño (2006) as well as those obtained in this study suggest that not all of the relationships proposed by Somerville et al. (2002) are applicable to the subduction zone in Mexico.

## CONCLUSIONS

In this investigation, we have generated a model for the Tecomán earthquake of January 22, 2003, while applying the method of empirical Green's functions and using the acceleration records of two earthquakes. The Tecomán earthquake has been used as the target event and the November 21, 2006 event as the element event. We have used the acceleration data recorded at the MANZ station, as obtained by CIRES, and the velocity data of four broad-band regional stations of SSN. These four stations provided good azimuthal coverage of the Tecomán earthquake. The process of modeling the target event has been done in four stages involving one, two, three and four SMGAs, respectively. The observed waveforms have been adjusted gradually by the synthetic waveforms and the residual values have progressively decreased in each stage from one to three SMGAs; the model with four SMGAs has shown an increased value in residual values and poor adjustment. Thus, the best fitting has been obtained by modeling the target event with three SMGAs, corresponding to the best adjustment in residual values. In addition, this model has a close resemblance with the dislocation model found by Yagi et al. (2004). The SMGA “1” found in our model is located at 1.72 km from the asperity A, as reported by Yagi et al. (2004). SMGA “2” is located at 5.16 km away from the hypocenter, and SMGA “3” is located at the same place as the asperity B found by Yagi et al. (2004).

We conclude that for the frequency band of 1–10 Hz, the nonlinear effects of soft soils were not significant at the MANZ site. The mild frequency shift seen on the HVSPR plots supports our interpretation. On the other hand, local site effects, due to soft soils, have been confirmed by comparing the HVSPR for all recording sites.

## ACKNOWLEDGEMENTS

We thank three anonymous reviewers and the Editor for their constructive comments. We appreciate the support of Lucio Camarillo of Centro de Instrumentación y Registro Sísmico (CIRES), for providing the acceleration records of the MANZ station, and the support of Carlos Valdés González, Caridad Cárdenas, for providing the records of the broadband network of Servicio Sismológico National (SSN). This experiment could have not taken place without the valuable help of Ricardo Vasquez, Horacio Mijares Juan Tejeda Jacome and Miguel Rodriguez in the instrumentation and logistic support. We thank Consejo Nacional de Ciencia y Tecnología (CONACYT) for the support provided to this project (under Grant No. SEP-2003-C02-43880/A).

## REFERENCES

1. Aki, K. (1967). “Scaling Law of Seismic Spectrum”, Journal of Geophysical Research, Vol. 72, No. 4, pp. 1217–1231.
2. Aki, K. (1988). “Local Site Effects on Strong Ground Motion” in “Earthquake Engineering and Soil Dynamics II—Recent Advances in Ground-Motion Evaluation (edited by J.L. Von Thun)”, Geotechnical Special Publication 20, American Society of Civil Engineers, New York, U.S.A.
3. Aki, K. (1993). “Local Site Effects on Weak and Strong Ground Motion”, Tectonophysics, Vol. 218, No. 1-3, pp. 93–111.
4. Alcocer, S.M. and Klingner, R.E. (editors) (2006). “The Tecomán, México Earthquake January 21, 2003: An EERI and SMIS Learning from Earthquakes Reconnaissance Report”, Technical Report, Earthquake Engineering Research Institute, Oakland, U.S.A.
5. Bandy, W., Mortera-Gutierrez, C., Urrutia-Fucugauchi, J. and Hilde, T.W.C. (1995). “The Subducted Rivera-Cocos Plate Boundary: Where is It, What is It, and What is Its Relationship to the Colima Rift?”, Geophysical Research Letters, Vol. 22, No. 22, pp. 3075–3078.
6. Bendat, J.S. and Piersol, A.G. (1971). “Random Data: Analysis and Measurement Procedures”, John Wiley & Sons, Inc., Hoboken, U.S.A.

7. Chang, S.W. and Bray, J.D. (1998). "Implications of Recent Strong Motion Data for Seismic Building Code Design at Deep, Stiff Soil Sites", Proceedings of the NEHRP Conference and Workshop on Research on the Northridge, California Earthquake of Janurary 17, 1994, Richmond, U.S.A., Vol. II, pp. 90–99.
8. Field, E.H., Johnson, P.A., Beresnev, I.A. and Zeng, Y. (1997). "Nonlinear Ground-Motion Amplification by Sediments during the 1994 Northridge Earthquake", Nature, Vol. 390, No. 6660, pp. 599–602.
9. Finn, L.D. (1991). "Geotechnical Engineering Aspects of Microzonation", Proceedings of the Fourth International Conference on Seismic Zonation, Stanford, U.S.A., Vol. 1, pp. 199–259.
10. Garduño, N. (2006). "Procesos de la Fuente del Sismo del 15 de Julio de 1996 Usando el Método de la Función de Green Empírica y Algoritmos Genéticos", Licenciate Thesis, Facultad de Ingeniería, Universidad Nacional Autónoma de México, Mexico City, Mexico (in Spanish).
11. Idriss, I.M. (1990). "Response of Soft Soil Sites during Earthquakes", Proceedings of H. Bolton Seed Memorial Symposium, Berkeley, U.S.A., Vol. 2, pp. 273–289.
12. Irikura, K. (1986). "Prediction of Strong Acceleration Motions Using Empirical Green's Function", Proceedings of the Seventh Japan Earthquake Engineering Symposium, Tokyo, Japan, pp. 151–156.
13. Kanasewich, E. (1981). "Time Series Analysis in Geophysics", University of Alberta Press, Edmonton, Canada.
14. Milne, J. (1898). "Seismology", Kegan Paul, Trench, Trübner & Co. Ltd., London, U.K.
15. Miyake, H., Iwata, T. and Irikura, K. (2003). "Source Characterization for Broadband Ground-Motion Simulation: Kinematic Heterogeneous Source Model and Strong Motion Generation Area", Bulletin of the Seismological Society of America, Vol. 93, No. 6, pp. 2531–2545.
16. Nozu, A. and Irikura, K. (2008). "Strong-Motion Generation Area of a Great Subduction-Zone Earthquake: Waveform Inversion with Empirical Green´s Functions for the 2003 Tokachi-Oki Earthquake", Bulletin of the Seismological Society of America, Vol. 98, No. 1, pp. 180–197.
17. Oppenheim, A.V. and Schafer, R.W. (1975). "Digital Signal Processing", Prentice-Hall, Englewood Cliffs, U.S.A.
18. Quintanar, L., Rodríguez-Lozoya, H.E., Ortega, R., Gómez-González, J.M., Domínguez, T., Javier, C., Alcántara, L. and Rebollar, C.J. (2010). "Source Characteristics of the 22 January 2003 $M_w$ = 7.5 Tecomán, Mexico, Earthquake: New Insights", Pure and Applied Geophysics (in press).
19. Reid, H.F. (1910). "The California Earthquake of April 18, 1906—Report of the State Earthquake Investigation Commission in Two Volumes and Atlas, Volume II: The Mechanics of the Earthquake", Publication 87, Volume II, Carnegie Institute of Washington, Washington, DC, U.S.A.
20. Seed, H.B. and Idriss, I.M. (1982). "Ground Motions and Soil Liquefaction during Earthquakes", Monograph MNO-5, Earthquake Engineering Research Institute, Oakland, U.S.A.
21. Singh, S.K., Ponce, L. and Nishenko, S.P. (1985). "The Great Jalisco, Mexico, Earthquakes of 1932: Subduction of the Rivera Plate", Bulletin of the Seismological Society of America, Vol. 75, No. 5, pp. 1301–1313.
22. Singh, S.K., Pacheco, J.F., Alcántara, L., Reyes, G., Ordaz, M., Iglesias, A., Alcocer, S.M., Gutierrez, C., Valdés, C., Kostoglodov, V., Reyes, C., Mikumo, T., Quaas, R. and Anderson, J.G. (2003). "A Preliminary Report on the Tecomán, Mexico Earthquake of 22 January 2003 ($M_w$ 7.4) and Its Effects", Seismological Research Letters, Vol. 74, No. 3, pp. 279–289.
23. Somerville, P., Irikura, K., Graves, R., Sawada, S., Wald, D., Abrahamson, N., Iwasaki, Y., Kagawa, T., Smith, N. and Kowada, A. (1999). "Characterizing Crustal Earthquake Slip Models for the Prediction of Strong Ground Motion", Seismological Research Letters, Vol. 70, No. 1, pp. 59–80.
24. Somerville, P.G., Sato, T., Ishii, T., Collins, N.F., Dan, K. and Fujiwara, H. (2002). "Characterizing Heterogeneous Slip Models for Large Subduction Earthquakes for Strong Ground Motion Prediction", Proceedings of the 11th Japan Earthquake Engineering Symposium, Tokyo, Japan, pp. 163–166 (in Japanese).
25. Yagi, Y., Mikumo, T., Pacheco, J. and Reyes, G. (2004). "Source Rupture Process of the Tecomán, Colima, Mexico Earthquake of 22 January 2003, Determined by Joint Inversion of Teleseismic Body-

Wave and Near-Source Data", Bulletin of the Seismological Society of America, Vol. 94, No. 5, pp. 1795–1807.

26. Zobin, V.M. and Pizano-Silva, J.A. (2007). "Macroseismic Study of the $M_w$ 7.5 21 January 2003 Colima, México, Across-Trench Earthquake", Bulletin of the Seismological Society of America, Vol. 97, No. 4, pp. 1221–1232.

[1] Website of CMT, www.seismology.harvard.edu/CMTsearch.html

*ISET Journal of Earthquake Technology, Paper No. 508, Vol. 47, No. 1, March 2010, pp. 25–46*

# USE OF STRONG-MOTION DATA FOR FREQUENCY-DEPENDENT SHEAR WAVE ATTENUATION STUDIES IN THE PITHORAGARH REGION OF KUMAON HIMALAYA

A. Joshi*, M. Mohanty**, A.R. Bansal***, V.P. Dimri*** and R.K. Chadha***

*Department of Earth Sciences, Indian Institute of Technology Roorkee, Roorkee-247667
**SERC Division, Department of Science and Technology, Government of India, New Delhi-110016
***National Geophysical Research Institute, Hyderabad-500606

## ABSTRACT

The Pithoragarh district in the state of Uttarakhand, India lies in the border region of India and Nepal and falls in the seismically active zone of Kumaon Himalaya. A local network of eight strong-motion accelerographs has been installed in this region since March 2006. The installed strong-motion instruments have recorded several events in this region. These events are located using HYPO71 and the processed digital data is used for obtaining the frequency-dependent shear wave attenuation. This paper presents a method of finding $Q_\beta(f)$ from the strong-motion data, which is based on the modified method of Joshi (2006). Based on the availability of data, hypocentral parameters, and clear S-phases, a total of 27 strong-motion records from six stations are used in this work. By using the inversion algorithm developed in this work, an average relation in the form, $Q_\beta(f) = 30 f^{1.45}$, is obtained for the Pithoragarh region of Kumaon Himalaya.

**KEYWORDS:** Strong Motion, Attenuation, Inversion, Himalaya

## INTRODUCTION

The Kumaon Himalaya is one of the seismically active regions of the world. Most parts of this region fall in the highest seismic hazard zone defined in the seismic zoning map of India. During the last 100 years, this region has been visited by 14 earthquakes of magnitudes greater than 6.0. It has been observed that the devastation caused by any earthquake in a region is directly related to the attenuation characteristics of the medium and to the amount of seismic energy released during the earthquake. The attenuation characteristics of the medium control the decay of the seismic energy in the lithosphere, and the source characteristics of the earthquake control the amount of energy released during the earthquake. Seismic energy attenuates differently in different rocks. The attenuation of seismic energy signifies a reduction in the energy caused by the heterogeneity and anelasticity in the earth.

The attenuation of seismic energy can be defined by the dimensionless quantity known as quality factor $Q$. This parameter is used to measure the tendency of material to dissipate energy during deformations. Although different fundamental definitions have been proposed for $Q$, the common idea has been to consider a ratio of potential energy to the dissipated energy over one period of harmonic deformations (Pelton, 2005). Attenuation is a petrophysical parameter that is sensitive to the lithology and physical properties like pressure, temperature, saturation with fluid, gas, etc. (Toksöz et al., 1979). Therefore, direct estimate of attenuation gives us an idea about the characteristics of the medium. The estimates of $Q$ have been found to be frequency-dependent by several researchers worldwide (Aki and Chouet, 1975; Aki, 1980; Gupta et al., 1995; Mandal et al., 2001). Numerous studies have been done worldwide to understand the attenuation characteristics by estimating $Q$ based on P-waves (i.e., $Q_\alpha$), S-waves (i.e., $Q_\beta$) and coda waves (i.e., $Q_c$). Very little work has been done, however, in the part of Kumaon and Garhwal Higher Himalaya to estimate the attenuation properties of the medium. Paul et al. (2003) estimated the frequency-dependent coda $Q$ relationship as $(92 \pm 4.73) f^{1.0 \pm 0.023}$ by using the single back scattering model proposed by Aki and Chouet (1975). Based on the study of the aftershock data of the Chamoli earthquake, Mandal et al. (2001) estimated $Q_c(f)$ as $(30\pm0.8)\,f^{1.21\pm0.03}$ for the region surrounding the epicenter of the main shock of the Chamoli earthquake. Gupta et al. (1995) estimated $Q_c(f)$ for the Garhwal Himalaya as $126\,f^{0.95}$ by using seven local earthquakes (2.4 ≤ $M_L$ ; $105\,f^{0.76}$ ≤ 4.9) recorded at five stations on 1.0-Hz velocity sensors. In all studies related to the estimation of coda $Q_c(f)$ relation for the Himalayan region, the single backscattering model proposed by Aki and Chouet (1975) has been used. Recently, a technique has been developed by Joshi (2006) which uses the S-phase of an accelerogram as input in an inversion algorithm and gives $Q_\beta(f)$ and corner frequency $f_c$ of the input events. In the approach given by Joshi (2006) a two-step inversion algorithm was applied to remove near-site effects in the accelerogram due to the unavailability of sufficient data for site studies. Using this technique, Joshi (2006) has estimated $Q_c(f) = 112\,f^{0.97}$ for the Garhwal Himalaya. In the present work we have used the vertical component of acceleration records, which is supposedly free from the site effects. Due to this reason, the two-step inversion used in the earlier approach is now reduced to a single-step algorithm. Further, in order to obtain a direct estimate of corner frequency, we have included a tree search in the inversion algorithm, which was not present in the earlier approach of Joshi (2006). The data used in this paper is collected from a strong-motion network installed in the Kumaon region.

## TECTONICS OF THE REGION

The frequent seismic activity and thrust system present in the Kumaon Himalaya demonstrate the seismotectonic importance of the region. The Kumaon sector manifests strong deformations and reactivation of some of the faults and thrusts during the Quarternary times. This is amply evident from the recurrent seismic episodes, geomorphic developments, and from the geodetic changes (Valdiya, 1999). This region shows the development of all four morphotectonic zones, which are demarcated by the intracrustal boundary thrust of regional dimensions. These zones from the south to the north are Siwalik or Sub Himalaya, Lesser Himalaya, Great Himalaya, and Tethys Himalaya (Paul et al., 2003). The Lesser Himalaya comprises various thrust sheets and nappes, sandwiched between the main boundary thrust (MBT) and main central thrust (MCT) at the base of the Great Himalaya. The Great Himalaya comprises mainly Kyanite-Sillimanite bearing high-grade psammatic Gneiss and Schist intruded by the anatectic Tertiary leucogranite (Paul et al., 2003).

The Kumaon Himalaya exposes all four major litho-tectonic subdivisions of the Himalaya from the south to the north. The Outer Himalaya consisting mainly of the molassic Siwalik super group of the Neo-Pliocene age is separated in the north from the Lesser Himalaya by the main boundary fault (MBF), thus exposing the highly-folded Precambrian Paleozoic sedimentary sequence with a few knappes of older crystalline rocks that are bounded by the main central thrust (MCT) in the north. The Greater or Higher Himalaya, with the north-dipping metamorphics belonging to the central crystalline zone, is separated from the thick pile of the Tethyan Paleo-Mesozoic sequence by the Martoli fault (MF).

Under a major seismicity project funded by Department of Science and Technology, Government of India, a network of eight strong-motion stations has been installed in the highly mountainous terrain of the Kumaon Himalaya. The locations of these eight stations along with the geology of the region are shown in Figure 1. The Pithoragarh region falls in the Lesser Himalayan zone and is bounded by MCT in the north and by North Almora thrust in the south. The Lesser Himalaya consists of the sediments of the Precambrian Palaeozoic and locally Mesozoic age, metamorphosed and subdivided by the thrusts with progressively older rocks towards the north. The Pithoragarh region has the exposures of an extensive sedimentary belt including an outer Krol belt and an inner Tejam-Pithoragarh belt. It consists of a thick sequence of argillo-calcareous and arenaceous sediments constituting the Garhwal super group. The Garhwal super group is divisible into the lower argillo-calacareous Tejam group, middle predominantly-arenaceous Berinag group and the upper metamorphites of the Didihat group. The Didihat group consists of complex assemblages of Phyllite, schist, amphibolite gneiss and quartzite. The strong-motion recorders placed in Sobla, Didihat and Thal are located on the metamorphosed older crystalline hard rocks, which are highly deformed, whereas the stations in Pithoragarh and Dharchula are located on the sedimentary rocks. Didihat is situated on the Askot crystallines (which is a part of the Almora crystallines). The station in Thal is situated on the quartzites of the Berinag formation. The station in Sobla is situated near the MCT and comprises crystalline rocks. The folds of the sedimentary belt of the Pithoragarh region show the variations of strain values and degrees of shape modifications from place to place (Bhattacharya, 1999). These structural features indicate the presence of persistently active collisional stresses in that area.

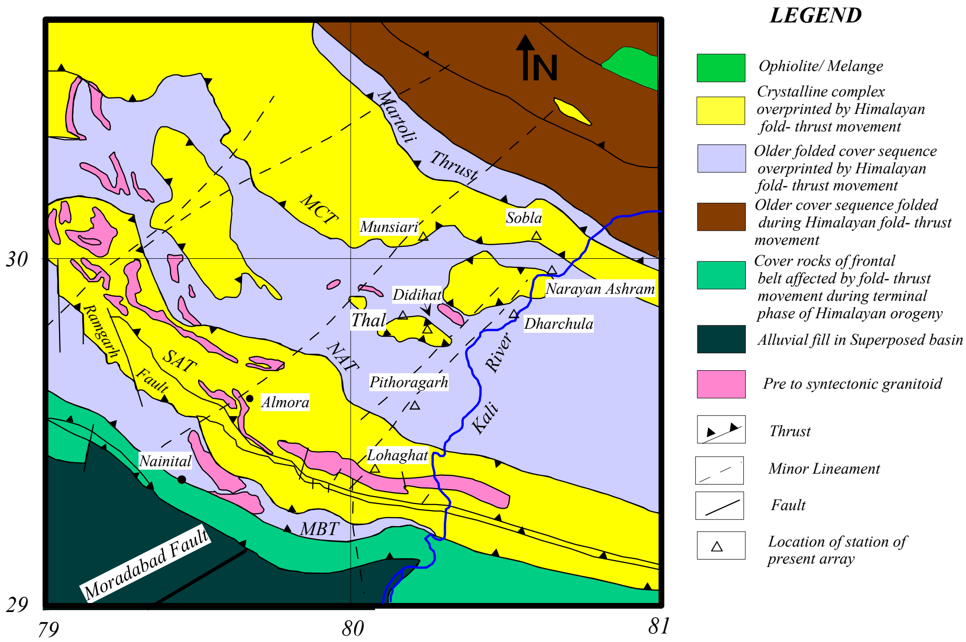


Fig. 1 Locations of the strong-motion recording stations installed in the Kumaon Himalaya (the geology and tectonics of the region are as in Dasgupta et al. (2000); the strong-motion stations of the local network are denoted by the triangles)

## DATA USED IN THE ANALYSIS

The strong-motion recorders installed at each station in the network are three-component force balance accelerometers. In order to have a nearly continuous digital recording mode, the threshold level of the instruments was set at a very low level of 0.005% of the full scale. The sensitivity of the instruments is 1.25 $V/g$ and the full-scale measurement is 2.5 $V$. This implies that the instruments have a very low threshold level of 0.1 Gal (0.001 m/s$^2$). The purpose of so low threshold level is to record almost every possible local event in the entire duration of the project. The sampling interval of digital data was kept as 0.01 s. The minimum inter-station distance between the stations of the network is approximately 11 km. Out of the eight accelerographs, seven are installed in the border district of Pithoragarh and one in the neighboring district of Champawat.

The collected accelerographs have been processed using the procedure suggested by Boore and Bommer (2005). The processing steps involve baseline correction, instrumental scaling, and frequency filtering. After the baseline and instrument corrections, a filter is generally applied to remove the high-frequency noise. In the usual processing of digital records, the California strong motion instrumentation program (CSMIP) uses the Butterworth filter with high-frequency cutoff of nearly 80% of the final sampling rate (Shakal et al., 2004). In the present work, we have the data recorded at the sampling rate of 0.01 s; therefore, on following this criterion, the high-frequency cutoff of the Butterworth filter becomes 40 Hz. The selection of the low-frequency cutoff of the Butterworth filter remains the most difficult part of strong-motion processing because the effect of increase in earthquake magnitude is to raise the response spectrum amplitudes at low frequencies. The selection of this cutoff is based on the criterion that the noise spectrum does not interfere with the usual strong-motion processing band. Hence, this depends on the characteristics of the noise and the event responsible for the record. In this work, we have selected noise from the pre-event memory of the digital records. The selection of the low cutoff of the Butterworth filter has been made in such a way that the ratio of the Fourier amplitude spectrum of the record to that of the noise is greater than 3 (Boore and Bommer, 2005). In the present work, based on the work by Boore and Bommer (2005) and Shakal et al. (2004), we have made use of the following criteria for the selection of the low-frequency cutoffs of the Butterworth filter:

- The first criterion uses the ratio of the Fourier amplitude spectrum of record to that of noise. The cutoff frequency is that frequency below which this ratio is less than 3.
- The second criterion uses the logarithms of the velocity response spectra of record and noise as originally proposed by Trifunac (1977). It is based on the observation that the logarithm of the velocity response spectrum of a record increases from low values at short periods to a maximum at intermediate periods and then starts decreasing for long periods, whereas the logarithm of the noise spectrum increases in the long-period range. The frequency, at which the ratio of the logarithms of the response spectra of record and noise is less than 3, is selected as the low-frequency corner of the Butterworth filter.
- The third criterion is based on the visual inspection of velocity and displacement time histories, which are obtained by the double integration of the acceleration record filtered by applying the Butterworth filter. The low-frequency cutoff of the Butterworth filter is based on the judgment whether or not the obtained time history shows any unusual trends.

The above criteria for the selection of the low-frequency cutoff of the Butterworth filter are shown in Figure 2. The low-frequency cutoffs of the Butterworth filter for different events recorded at different stations using these criteria are given in Table 1. One of the important steps that are used in the processing of accelerograms is padding. The padding processing step extends the time series in both directions by adding zeroes to the leading and trailing ends of the record. This step is applied before the application of the low-cut frequency filtering. The zero pads are added symmetrically to both ends of the records in order to accommodate the filter transient. The length of zero pad, $t_{\text{pad}}$, at each end is calculated by using the following empirically determined formula (Converse and Brady, 1992):

$$t_{\text{pad}} = \frac{1.5 \times \text{nroll}}{f_c} \tag{1}$$

where 'nroll' denotes the roll-off of the acausal low-cut Butterworth filter and $f_c$ the low-cut frequency of the filter. The effect of padding is visible in the integrated displacement record obtained from the accelerogram. A significant value at the end of the velocity or displacement time series indicates that there may be insufficient padding. The integrated displacement record of Dharchula shows that without padding, there is a significant value at the end of the displacement record (see Figure 3(c)). The padding in the accelerogram gives a displacement record (see Figure 3(f)), which does not have significant value at the end. All records from the instruments have been processed before being used in the present work. The processed records at the Dharchula station are shown in Figure 4.

The strong-motion network installed in the Kumaon region has recorded several events from March, 2006 to February, 2007. The events, which were recorded at more than three stations, are localized by using the HYPO71 program originally developed by Lee and Lahr (1972). Table 2 gives the hypocentral parameters of these events and the obtained errors in their localization. The projections of the ray paths of the energy released from the events used in the present work to the recording stations are shown in Figure 5. It shows that at the Sobla station, the ray path of the seismic energy encounters the higher Himalayan topography, while the ray paths of the energy recorded by the other stations encounter mainly the lesser Himalayan topography.

Seismic moment is one of the most important parameters, which is required as an input to the present algorithm. This is computed from the source spectrum of the recorded data by using Brune's model (Keilis-Borok, 1959; Brune, 1970). In this process, a time window of length covering the entire S-phase is applied to the corrected accelerogram. The sampled window is cosine tapered with 10% taper at both ends (Sharma and Wason, 1994). The spectrum of this time series is obtained by using a FFT algorithm and is then corrected for the anelastic attenuation and geometrical spreading terms. For correcting anelastic attenuation, we use the frequency-dependent quality factor given by Joshi (2006), which is applicable for the Garhwal Himalaya. The plots of median source spectra of the eight events, as computed from the recorded data, are shown in Figure 6. By using the long-term flat levels in these spectra, the seismic moment of each event is calculated. Based on Brune's model (Brune, 1970), the seismic moment $M_0$ of an earthquake can be calculated from the long-term flat level of the displacement spectrum given by

$$M_0 = \frac{4\pi\rho\beta^3\Omega_0 R}{R_{\theta\phi}} \tag{2}$$

where $\rho$ and $\beta$ are the density and S-wave velocity of the medium, respectively, $\Omega_0$ is the long-term flat level of the source displacement spectrum at the hypocentral distance $R$, and $R_{\theta\phi}$ is the radiation-pattern coefficient. We use the density of medium as 2.7 g/cm$^3$ (Hanks and McGuire, 1981) and shear wave velocity as 3.3 km/s (Joshi, 2000), respectively. The fault plane solution for each event used in the present work could not be determined owing to the small number of recording stations. Therefore, the radiation pattern term $R_{\theta\phi}$ for S-wave is approximately taken as 0.55 (Atkinson and Boore, 1995). In the above expression, the geometrical spreading term is taken as $1/R$. In the inversion procedure, the vertical component of a record is used to remove the possibility of site effects in the horizontal components. Therefore, in order to have consistency in the inversion procedure, source spectra are computed from the vertical components of records. For computing seismic moments from the vertical components by using the equation given above, we do not include the term, which accounts for the division of energy into two horizontal components. It is also noticed that corner frequencies for the vertical and horizontal motions will not be same. In order to keep consistency in the approach we compute source parameters from the vertical components and same components are used for inversion.

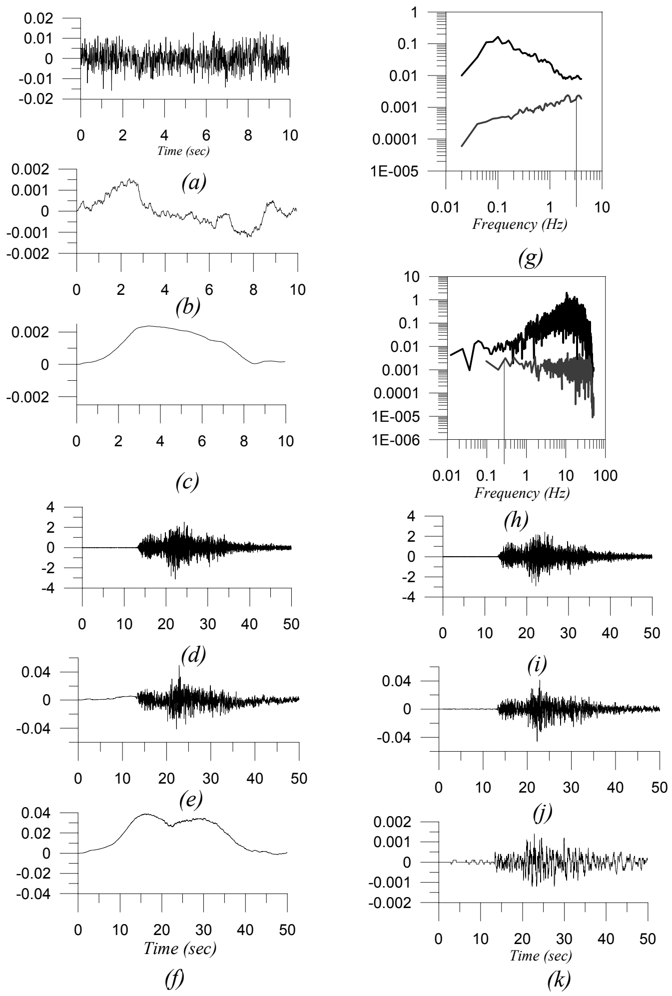


Fig. 2 (a) Acceleration, (b) velocity, and (c) displacement waveforms of the digitized record of noise taken from the pre-event memory of the record of event recorded at the Dharchula station on 05/05/06; (d) Acceleration, (e) velocity, and (f) displacement records of the signal corrupted with noise; (g) Pseudo-velocity response spectra at 5% damping of noise and signal with noise; (h) Amplitude spectra of the acceleration records of noise and signal corrupted with noise; (i) Acceleration, (j) velocity, and (k) displacement records of the signal corrupted with noise (vertical lines in the spectra denote the lower frequency cutoffs)

**Table 1: Frequency Range of Low-Cut Filter Used for the Processing of Records of Strong Ground Motions of Different Events Recorded at Different Stations**

| Station | Date | Origin Time | $F_{cl}$ |
|---|---|---|---|
| Pithoragarh | 05/05/06 | 8:00:28.72 | 2.0 |
| | 05/08/06 | 7:33:00.84 | 2.0 |
| | 27/10/06 | 7:55:01.39 | 2.0 |
| | 05/05/06 | 8:49:46.48 | 1.8 |
| | 05/02/07 | 7:57:34.94 | 1.8 |
| | 27/10/06 | 8:01:32.23 | 1.8 |
| Thal | 05/05/06 | 8:00:28.72 | 1.5 |
| | 27/10/06 | 7:55:01.39 | 2.0 |
| | 07/05/06 | 6:46:03.72 | 1.8 |
| | 05/05/06 | 8:49:46.48 | 1.8 |
| | 05/08/06 | 7:33:00.84 | 1.9 |
| Sobla | 05/05/06 | 8:00:28.72 | 1.0 |
| | 01/04/06 | 19:42:52.1 | 1.0 |
| | 05/05/06 | 8:49:46.48 | 1.0 |
| Didihat | 05/05/06 | 8:00:28.72 | 0.7 |
| | 05/08/06 | 7:33:00.84 | 0.8 |
| | 01/04/06 | 19:42:52.1 | 0.7 |
| | 27/10/06 | 7:55:01.39 | 0.8 |
| | 05/05/06 | 8:49:46.48 | 0.8 |
| | 05/02/07 | 7:57:34.94 | 0.8 |
| | 07/05/06 | 6:46:03.72 | 0.9 |
| Dharchula | 05/05/06 | 8:00:28.72 | 1.0 |
| | 05/05/06 | 8:49:46.48 | 1.5 |
| | 01/04/06 | 19:42:52.1 | 1.5 |
| | 07/05/06 | 6:46:03.72 | 2.0 |
| | 27/10/06 | 7:55:01.39 | 1.5 |
| | 27/10/06 | 8:01:32.23 | 1.6 |

Note: $F_{cl}$ denotes the lower corner of the low-cut filter used for the processing of record.

We know that geometrical spreading term for the spherical earth model cannot be represented for all ranges by the simple power law and is not frequency-independent; however, at relatively short epicentral distances (less than a few hundred km), these effects are negligible (Yang et al., 2007). In order to check the dependency of spectral acceleration on the distance parameter we performed various numerical tests and checked the linear-, exponential- and power-law dependencies of the long-term flat level on hypocentral distance. These numerical tests are shown in Figure 7. Various statistical parameters, calculated for each dependency, are given in Table 3. It is seen that among these, the power-law dependency of the order $R^{-0.97} \sim 1/R$ gives the maximum correlation and minimum error. The mean and standard deviation from the data match effectively with those from the power-law fit. Thus, this study confirms the validity of the term $1/R$ to represent the attenuation due to geometrical spreading for the present data for both inversion and computation of the seismic moment. The geometrical factor term has been used as $1/R$ for the strong-motion studies of Himalayan and worldwide earthquakes by Boore (1983), Atkinson and Boore (1995), Joshi et al. (2001), Joshi and Midorikawa (2004) and

Joshi (2006). Since the spectral acceleration at a particular station is dependent on the geometrical spreading term, the value of this term other than $1/R$ has a direct influence on the obtained results. Therefore, the use of the geometrical term other than $1/R$ needs to be validated before using any data in a new region.

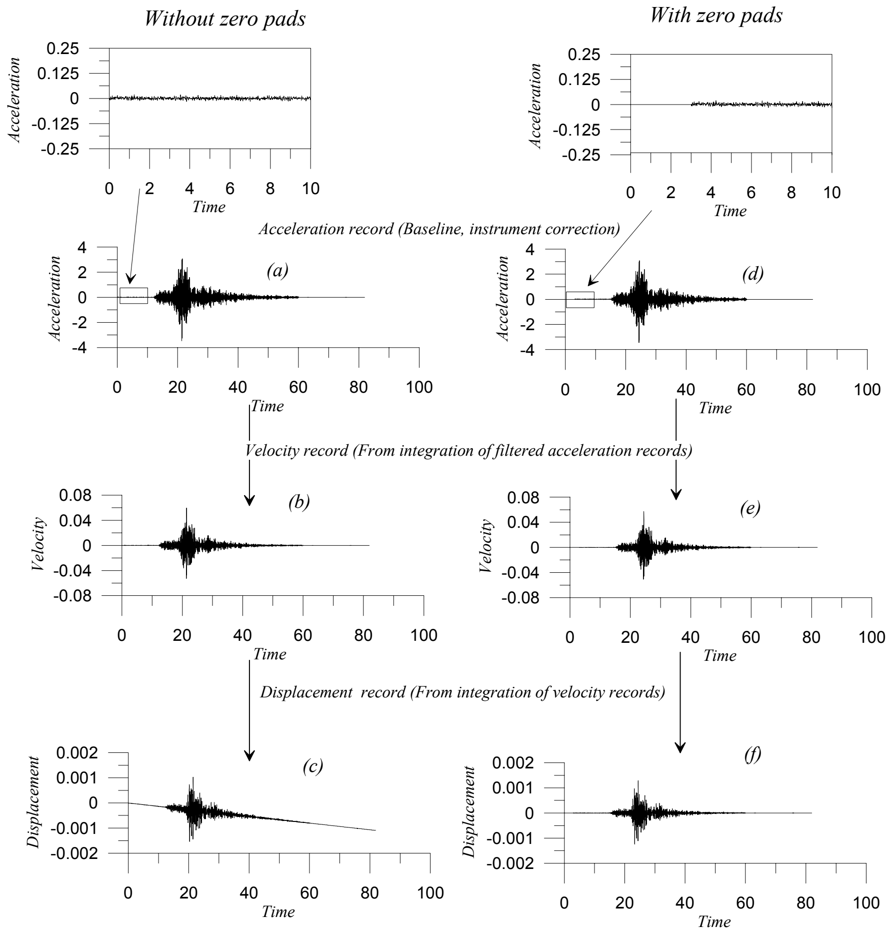


Fig. 3 (a) Acceleration record without zero pads; (b) Velocity record obtained from the integration of acceleration record; (c) Displacement record obtained from the integration of velocity record; (d) Acceleration record with zero pads; (e) Velocity record obtained from the integration of zero-padded acceleration record, and (f) Displacement record obtained from the integration of the velocity record in (e)

## INVERSION

The acceleration spectrum of shear waves at distance $R$ due to an earthquake of seismic moment $M_0$ can be given at frequency $f$ as (Boore, 1983; Atkinson and Boore, 1998)

$$A(f) = CS(f, f_c)D(f) \tag{3}$$

where the term $C$ is constant at a particular station for a given earthquake, $S(f, f_c)$ represents the source acceleration spectrum, and $D(f)$ denotes a frequency-dependent diminution function. This function modifies the spectral shape and is given as (Boore and Atkinson, 1987)

$$D(f) = \left[ \frac{e^{\frac{-\pi fR}{Q(f)\beta}}}{G(R)} \right] P(f, f_{\max}) \tag{4}$$

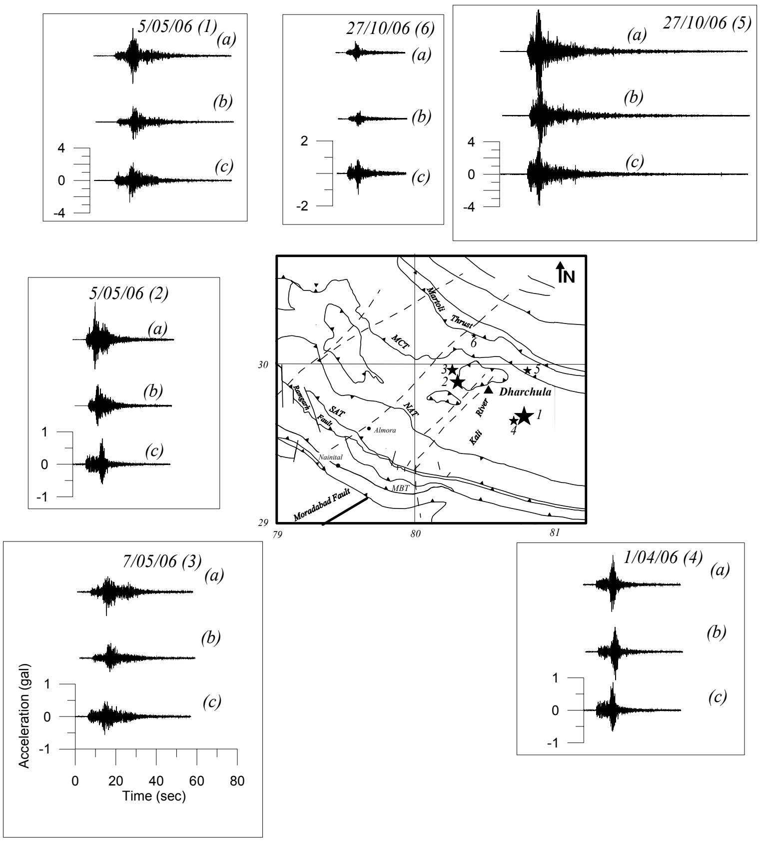

Fig. 4 Processed (a) NS, (b) EW and (c) vertical components of the accelerograms of some of the events recorded at the Dharchula station (stars denote the epicenters of events; triangles show the locations of recording stations; tectonics of the region is taken as in Dasgupta et al. (2000); number assigned to each record in brackets corresponds to the event given in Table 2)

**Table 2: Estimated Hypocentral Parameters of Different Events Used in the Present Work and the Errors Obtained in Their Localization**

| Date | Origin Time | Epicenter | Depth (km) | $M_0$ ($\times 10^{22}$ dyne-cm) | Number of Stations | Error in Depth (km) |
|---|---|---|---|---|---|---|
| 05/05/06 (1) | 08:00:28.72 | 29º 38.65’, 80º 42.16’ | 30 | 0.62 | 5 | 2.7 |
| 05/05/06 (2) | 08:49:46.48 | 29º 40.43’, 80º 45.98’ | 25 | 0.12 | 5 | 4.2 |
| 07/05/06 (3) | 06:46:03.72 | 29º 57.57’, 80º 47.89’ | 35 | 0.10 | 3 | 14.1 |
| 01/04/06 (4) | 19:42:52.1 | 30º 10.14’, 80º 24.63’ | 10 | 0.043 | 3 | 6.5 |
| 27/10/06 (5) | 07:55:01.39 | 29º 57.46’, 80º 15.23’ | 13 | 0.21 | 5 | 5.6 |
| 27/10/06 (6) | 08:01:32.23 | 29º 52.35’, 80º 17.70’ | 16 | 0.29 | 5 | 3.1 |
| 05/08/06 (7) | 07:33:00.84 | 29º 52.61’, 80º 06.88’ | 25 | 1.9 | 3 | 2.1 |
| 05/02/07 (8) | 07:57:34.94 | 29º 52.18’, 80º 16.94’ | 32 | 0.71 | 3 | 1.9 |
| Note: The number assigned to each event is used in Figure 4. | | | | | | |

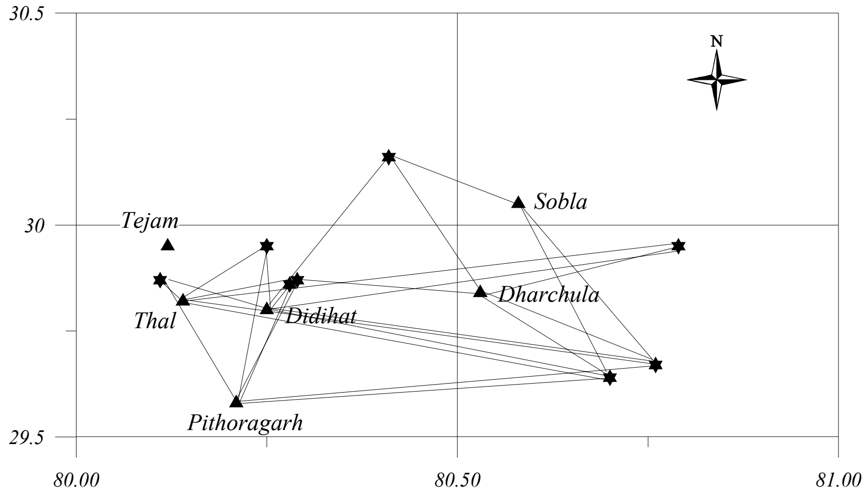


Fig. 5 Projections of the ray paths of different events recorded at different stations (stars denote the epicenters of studied earthquakes and triangles denote the locations of recording stations)

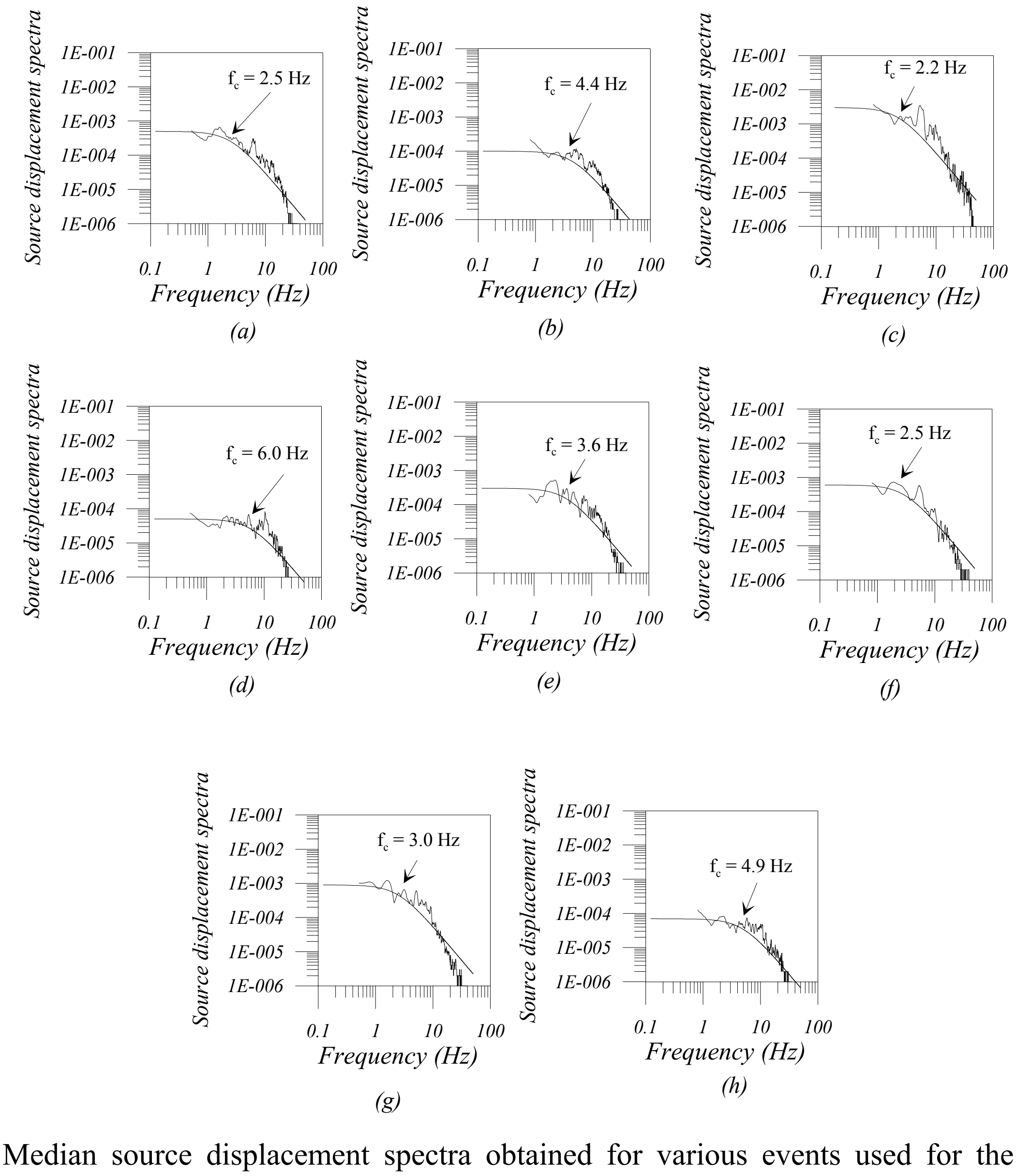


Fig. 6 Median source displacement spectra obtained for various events used for the present study (the theoretical Brune's displacement spectrum is shown in solid line)

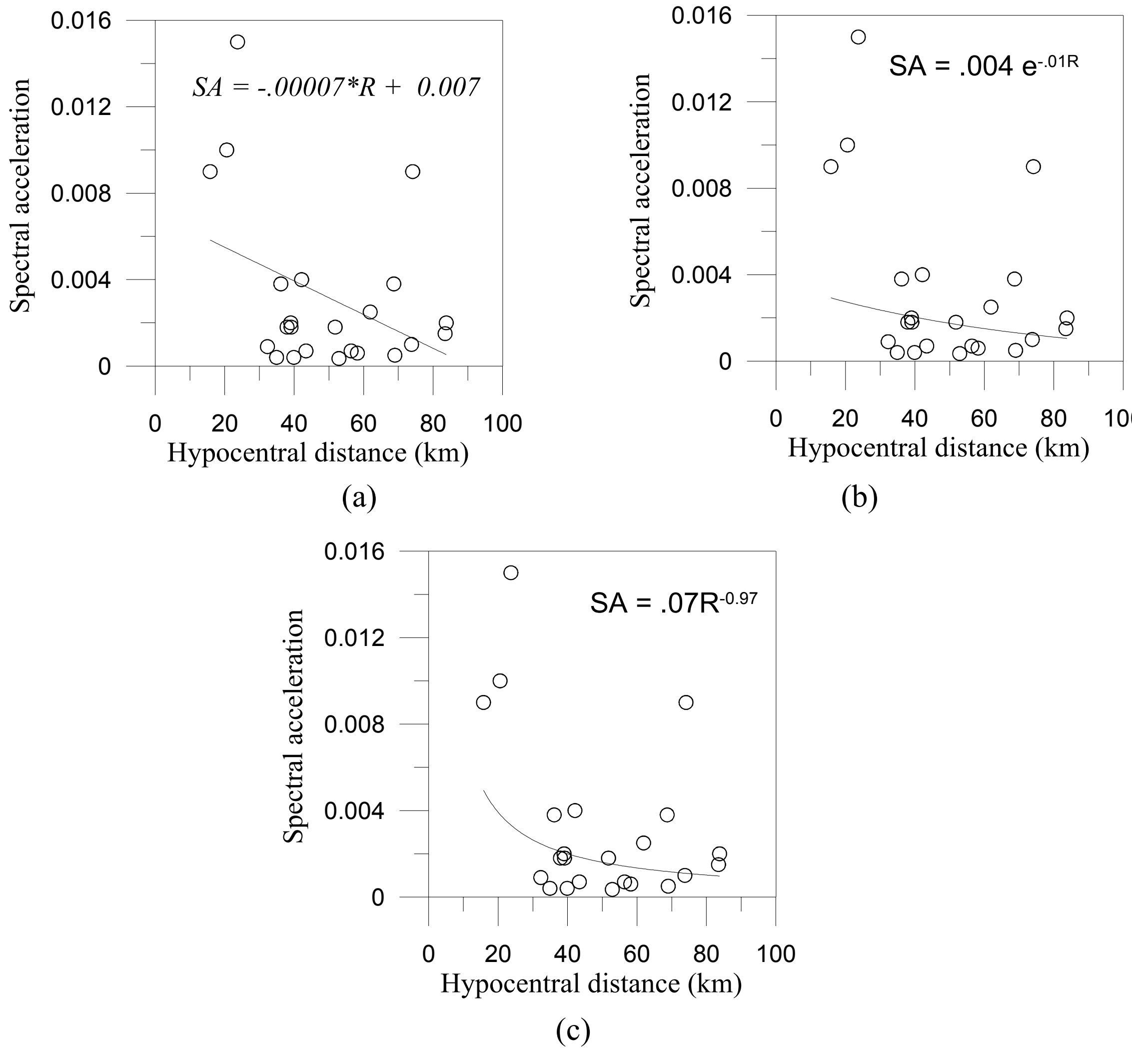


Fig. 7 (a) Linear-, (b) exponential- and (c) power-law dependence of spectral acceleration data used in the present work on hypocentral distance (the parameters SA and $R$ are long-term flat level and hypocentral distance, respectively)

**Table 3: Dependence of Spectral Acceleration on Hypocentral Distance**

| Type of Fit | Obtained Relation for SA | Mean (Data) | S.D. (Data) | Mean (Fit) | S.D. (Fit) | Error Sum of Square | Residual Sum of Square | Correlation Coefficient |
|---|---|---|---|---|---|---|---|---|
| Linear | $-0.00007R+0.007$ | 3.817 | 0.433 | −4.96 | 0.00004 | 8.78 | 12.42 | 0.706 |
| Exponential | $0.004e^{-0.01R}$ | 3.817 | 0.433 | −5.59 | 0.00006 | 9.42 | 9.41 | 0.706 |
| Power | $0.07R^{-0.97}$ | 3.817 | 0.433 | 3.52 | 1.054 | 1.01 | 1.09 | 0.733 |

In Equation (4), $P(f, f_{\max})$ is a high-cut filter and $e^{\frac{-\pi fR}{Q(f)\beta}} \big/ G(R)$ is the filter used to define the anelastic attenuation and geometrical spreading of the seismic energy. As we are using the data from those events, which lie at the hypocentral distances ≤ 100 km, $G(R)$ is assumed as $1/R$ (Singh et al., 2006). The term $Q_\beta(f)$ used in Equation (4) is the frequency-dependent shear wave quality factor. In this work we take $f_m$ as 50 Hz, which is the Nyquist frequency of the processed records at a sampling interval of 0.01 s. This expression serves as the basis for our inversion. For a double-couple seismic source embedded in an elastic medium, on considering only S-waves, $C$ is given as (Boore, 1983)

$$C = \frac{M_0 R_{\theta\phi} \mathrm{FS}}{4\pi\rho\beta^3} \tag{5}$$

In this expression $M_0$ is the seismic moment, $R_{\theta\phi}$ is the radiation pattern, FS is the amplification due to free surface, and $\rho$ and $\beta$ are the density of the medium and the shear wave velocity, respectively. In the present work we have used the values of the parameters $R_{\theta\phi}$ and FS as 0.55 and 2.0, respectively (Atkinson and Boore, 1995). The density of the medium and the shear wave velocity in Himalaya have been assumed as 2.7 g/cm$^3$ (Hanks and McGuire, 1981) and 3.3 km/s (Joshi, 2000), respectively. The filter $S(f, f_c)$ in Equation (3) defines the source spectrum of the earthquake. On using the spectral shape based on the $\omega^{-2}$ decay of high frequency proposed by Aki and Chouet (1975) and Brune (1970), $S(f, f_c)$ is defined as

$$S(f, f_c) = \frac{(2\pi f)^2}{1 + \left(\frac{f}{f_c}\right)^2} \tag{6}$$

Further, Equation (3) is linearized by taking its natural logarithm to become

$$\ln A(f) = \ln C + \ln S(f, f_c) - \frac{\pi f R}{Q_\beta(f)\beta} - \ln R + \ln P(f, f_{\max}) \tag{7}$$

where $Q_\beta(f)$ and $f_c$ are unknown. The term representing the source filter $S(f, f_c)$ can be replaced with the help of Equation (3). Further, with the assumption that $f_c$ is known, we are left with only one unknown, $Q_\beta(f)$. On rearranging the known and unknown quantities on different sides, we obtain the following form from Equation (7):

$$\frac{-\pi f R}{Q_\beta(f)\beta} = \ln A(f) - \ln C - \ln S(f, f_c) + \ln R - \ln P(f, f_{\max}) \tag{8}$$

We obtained following set of equations at the 1st recording station for the $i$th earthquake for the frequencies $f_1$, $f_2$, $f_3$ ………… $f_n$, where $n$ denotes the total number of digitized samples in the acceleration record:

$$\frac{-\pi f_1 R_{i1}}{Q_\beta(f_1)\beta} + e = D_{i1}(f_1) \tag{9}$$

$$\frac{-\pi f_2 R_{i1}}{Q_\beta(f_2)\beta} + e = D_{i1}(f_2) \tag{10}$$

$$\vdots \qquad \vdots \qquad \vdots$$

$$\frac{-\pi f_n R_{i1}}{Q_\beta(f_n)\beta} + e = D_{i1}(f_n) \tag{11}$$

In these expressions, $D_{i1}(f_k)$ is given as (for $j$ = 1)

$$D_{ij}(f_k) = \ln A(f_k) - \ln C - \ln\left(S(f_k, f_c)\right) + \ln R_{ij} - \ln P(f_k, f_{\max}); \quad k = 1, 2, 3, \ldots, n \tag{12}$$

where the subscripts $i$ and $j$ in the parameters $D_{ij}(f_k)$ and $R_{ij}$ represent the event and station number, respectively. In the matrix form, the above set of equations at the 1st recording station for $m$ number of earthquakes can be written as

$$
\begin{bmatrix}
\frac{-\pi f_1 R_{11}}{\beta} & 0 & 0 & \ldots\ldots\ldots\ldots & 0 & 1 \\
0 & \frac{-\pi f_2 R_{11}}{\beta} & 0 & \ldots\ldots\ldots\ldots & 0 & 1 \\
0 & 0 & \frac{-\pi f_3 R_{11}}{\beta} & \ldots\ldots\ldots\ldots & 0 & 1 \\
\vdots & \vdots & \vdots & & \vdots & \vdots \\
0 & 0 & 0 & \ldots\ldots & \frac{-\pi f_n R_{11}}{\beta} & 1 \\
 & & & \vdots & & \\
 & & \text{for } m\text{th earthquake} & & & \\
\frac{-\pi f_1 R_{m1}}{\beta} & 0 & 0 & \ldots\ldots\ldots\ldots & 0 & 1 \\
0 & \frac{-\pi f_2 R_{m1}}{\beta} & 0 & \ldots\ldots\ldots\ldots & 0 & 1 \\
0 & 0 & \frac{-\pi f_3 R_{m1}}{\beta} & \ldots\ldots\ldots\ldots & 0 & 1 \\
\vdots & \vdots & \vdots & & \vdots & \vdots \\
0 & 0 & 0 & \ldots\ldots & \frac{-\pi f_n R_{m1}}{\beta} & 1
\end{bmatrix}
\begin{bmatrix}
\frac{1}{Q_\beta(f_1)} \\
\frac{1}{Q_\beta(f_2)} \\
\frac{1}{Q_\beta(f_3)} \\
\vdots \\
\frac{1}{Q_\beta(f_n)} \\
e
\end{bmatrix}
=
\begin{bmatrix}
D_{11}(f_1) \\
D_{11}(f_2) \\
D_{11}(f_3) \\
\vdots \\
D_{11}(f_n) \\
\vdots \\
D_{m1}(f_1) \\
D_{m1}(f_2) \\
D_{m1}(f_3) \\
\vdots \\
D_{m1}(f_n)
\end{bmatrix}
\qquad (13)
$$

This can be represented in the following form:

$$[G]\{m\} = \{d\} \qquad (14)$$

The rectangular matrix $[G]$ in Equation (14) represents the first rectangular matrix in Equation (13), the column matrix $\{m\}$ represents the column matrix on the left hand side of Equation (13) and the column matrix $\{d\}$ represents the column matrix on the right hand side of Equation (13). In Equation (14), the model parameters are contained in the model matrix $\{m\}$ and the spectral components in the data matrix $\{d\}$. Inversion of the $[G]$ matrix gives the estimated model matrix $\{m\}$ on using the Newton's method as

$$\{m\}_{\text{est}} = \left([G]^T [G]\right)^{-1} [G]^T \{d\} \qquad (15)$$

The above inversion is prone to problems if $[G]^T [G]$ is even close to being singular and for such cases, we can solve for $\{m\}$ by using the singular value decomposition (SVD) (Press et al., 1992). Formulation for the SVD-based solution follows Lanczos (1961). In this formulation, the $[G]$ matrix is decomposed into $[V_p]$, $[U_p]$ and $[\Lambda_p]$ matrices as given by Fletcher (1995):

$$[G]^{-1} = [V_p][\Lambda_p][U_p]^T \qquad (16)$$

where $\left[V_p\right]$, $\left[U_p\right]$ and $\left[\Lambda_p\right]$ are the matrices having non-zero singular vectors and singular values. For the present work, the software QINV developed by Joshi (2006) has been modified and used. We have computed root-mean-square error (RMSE) between the elements of input data matrix and estimated data matrix in each iteration and this is used as the basis for the selection of final model. In the present inversion, we have performed a grid search for $f^c$.We use the initial values of $f^c$ as 0.01 Hz and then it is increased in $\Delta f_c$ increments of 0.01 Hz up to 10.0 Hz. A tree diagram for the selection of corner frequencies of different events is shown in Figure 8. We get different solutions for different possibilities of $f^c$. The final solution is that which gives the minimum RMSE.

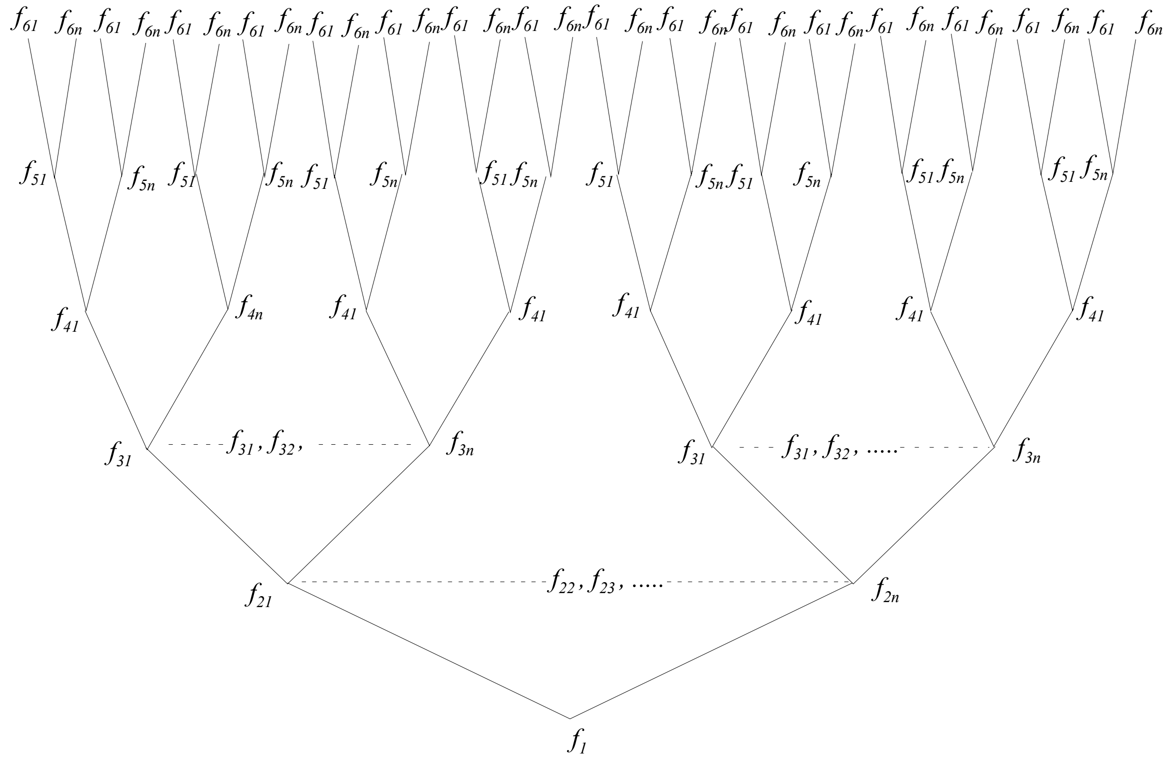


Fig. 8 Tree for the search of corner frequencies of various events (the tree diagram is shown for only two nodes; however, there will be several nodes between $f_{21}$ to $f_{2n}$, $f_{31}$ to $f_{3n}$, etc., where $f_{21}$ denotes the corner frequency of second event with first value and $f_{2n}$ denotes the corner frequency of second event with last value; the present tree diagram is for one value of $f_1$; however, in the present algorithm this also varies from 1 to $n$; for simplicity in the diagram $n$ is kept same for all events; however, in actual algorithm $n$ can be different for different events)

Due to the presence of site amplification effects in the horizontal component of the records we have used the vertical component of a record as an input to the algorithm. The spectrum of S-phase in the corrected accelerogram has been used as an input to the inversion algorithm developed in this paper. A time window, which starts from the onset of S-phase in the record and covers the entire S-phase, has been applied to the corrected accelerogram. This sampled window is cosine tapered with 10% taper at both ends (Sharma and Wason, 1994). The so-obtained spectrum is further smoothened before being used as an input to the present algorithm. The complete process of obtaining spectral amplitudes from the processed time series is shown in Figure 9. The whole algorithm is designed in such a manner that the input of acceleration spectra of different events is given in an order of increasing seismic moment. The value of so-obtained $Q_\beta(f)$ corresponds to different frequencies at different stations.

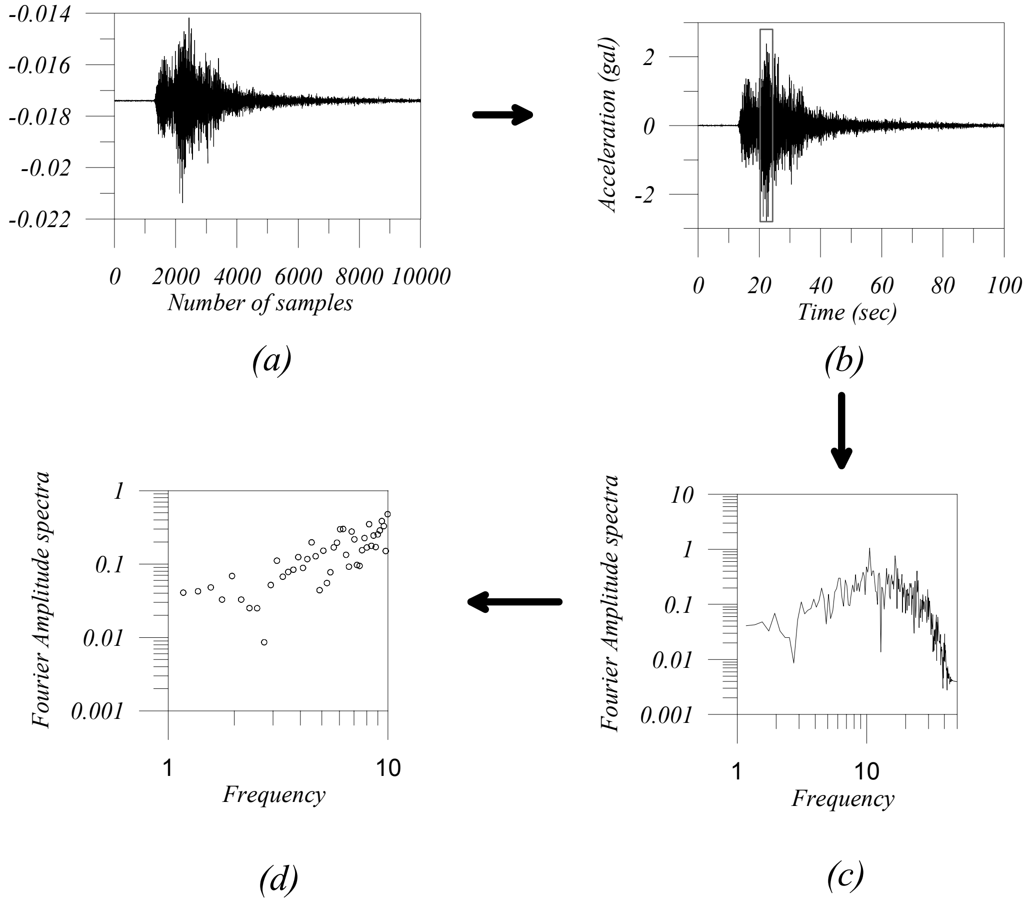


Fig. 9 (a) Vertical component of unprocessed accelerogram of 05/05/06 event recorded at Dharchula station; (b) Processed accelerogram at Didihat station; (c) Acceleration spectrum of S-phase marked by rectangular block with a time window of 4.0 s; (d) Discrete value of acceleration spectra used for present inversion (the discrete values of acceleration spectra are shown by small circles)

## RESULTS AND DISCUSSION

A numerical experiment is performed in which the time window has been changed and its relation with RMSE is observed for deriving the $Q_\beta(f)$ relationship for the station at Pithoragarh. We have taken records from six events recorded at this station, which are given in Table 1. It is seen that the selection of window in this approach is dependent on the S-phase present in the record. The S-phase is small for the near-field events while it is large for the far-field or distant earthquakes. The minimum time window for the S-phase is 3 s in the case of data recorded at Pithoragarh station for the event recorded on 5/08/06. We have changed the time window to 2.5, 3.0, 3.5, 4.0 and 7.0 s. The error obtained and its dependence on time window is shown in Figure 10. The so-obtained relation and errors for different time windows are given in Table 4. It is seen that the minimum error is obtained for the case of 3.0-s time window and that it increases when this window is either increased or decreased. This may be due to the overlapping of other phases in the input record for larger time windows and incomplete S-phases in smaller time windows. This experiment shows that a proper choice of window has strong influence on the obtained $Q_\beta(f)$ structure. On repeating this experiment on other stations, it has been seen that the selection of time window is decided by the shortest time window which covers the complete S-phase in the near-field record at any station. Further, in a separate numerical experiment a comparatively high RMSE was observed when we used different windows for different records as input to the algorithm.

**Table 4: Dependence of Obtained $Q_\beta(f)$ Relationship on Time Window**

| Length of Time Window (s) | Obtained Relation | RMSE |
|---|---|---|
| 2.5 | $Q_\beta(f)=186f^{0.72}$ | 0.000028 |
| 3.0 | $Q_\beta(f)=73f^{1.28}$ | 0.000011 |
| 3.5 | $Q_\beta(f)=181f^{0.64}$ | 0.000056 |
| 4.0 | $Q_\beta(f)=36f^{1.56}$ | 0.00017 |
| 7.0 | $Q_\beta(f)=15f^{1.24}$ | 0.00143 |

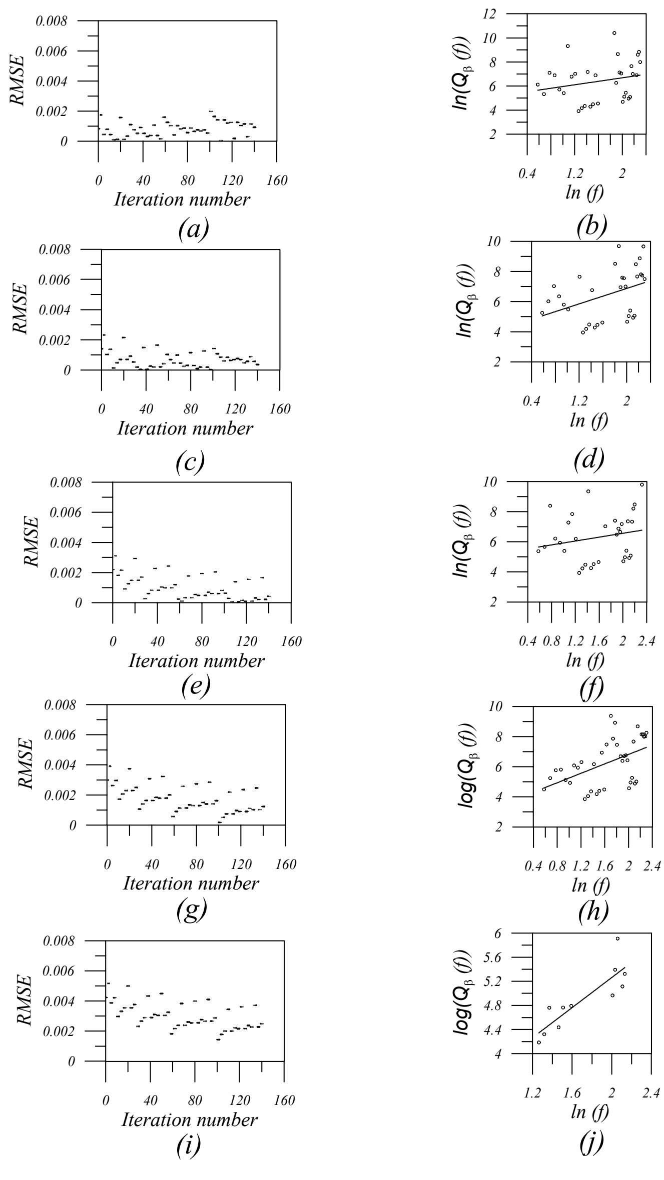


Fig. 10 Dependence of time window on the obtained results (the error plots for time windows of 2.5, 3.0, 3.5, 4.0 and 7.0 s are shown in (a), (c), (e), (g) and (i), respectively; the obtained $Q_\beta(f)$ relationships for the spectra of input time windows of 2.5, 3.0, 3.5, 4.0 and 7.0 s are shown in (b), (d), (f), (h) and (j), respectively)

This inversion algorithm is also dependent on the selection of corner frequency for individual events. We have devised a tree in which the corner frequency of input events is changed in an iterative manner.

Some of the results of this iterative inversion for the data at Pithoragarh stations for the input time window of 2.5 s are shown in Figure 11. The error plot corresponding to the different values of selected corner frequencies and their dependence on RMSE is shown in Figure 11(a). The corresponding relation and the set of corner frequencies for the so-obtained $Q_\beta(f)$ are shown in Table 5.

**Table 5: Different Sets of Corner Frequencies and the Corresponding Errors in the Observed Relation**

| S. No. | Corner Frequency of Input Events | RMSE |
|---|---|---|
| Case 1 | $f_{c1}=1.9,\ f_{c2}=2.0,\ f_{c3}=2.0,\ f_{c4}=2.4,\ f_{c5}=2.4,\ f_{c6}=6.4$ | .0019 |
| Case 2 | $f_{c1}=1.9,\ f_{c2}=2.0,\ f_{c3}=2.0,\ f_{c4}=2.4,\ f_{c5}=3.2,\ f_{c6}=6.4$ | .0016 |
| Case 3 | $f_{c1}=1.9,\ f_{c2}=2.0,\ f_{c3}=2.0,\ f_{c4}=2.4,\ f_{c5}=4.0,\ f_{c6}=6.4$ | .0014 |
| Case 4 | $f_{c1}=1.9,\ f_{c2}=2.0,\ f_{c3}=2.0,\ f_{c4}=3.6,\ f_{c5}=4.0,\ f_{c6}=6.4$ | .000028 |
| Case 5 | $f_{c1}=1.9,\ f_{c2}=2.0,\ f_{c3}=3.0,\ f_{c4}=3.6,\ f_{c5}=4.0,\ f_{c6}=6.4$ | .0014 |
| Case 6 | $f_{c1}=1.9,\ f_{c2}=2.0,\ f_{c3}=2.0,\ f_{c4}=2.4,\ f_{c5}=4.8,\ f_{c6}=6.4$ | .0012 |
| Case 7 | $f_{c1}=1.9,\ f_{c2}=2.0,\ f_{c3}=2.0,\ f_{c4}=3.6,\ f_{c5}=4.8,\ f_{c6}=6.4$ | .0012 |

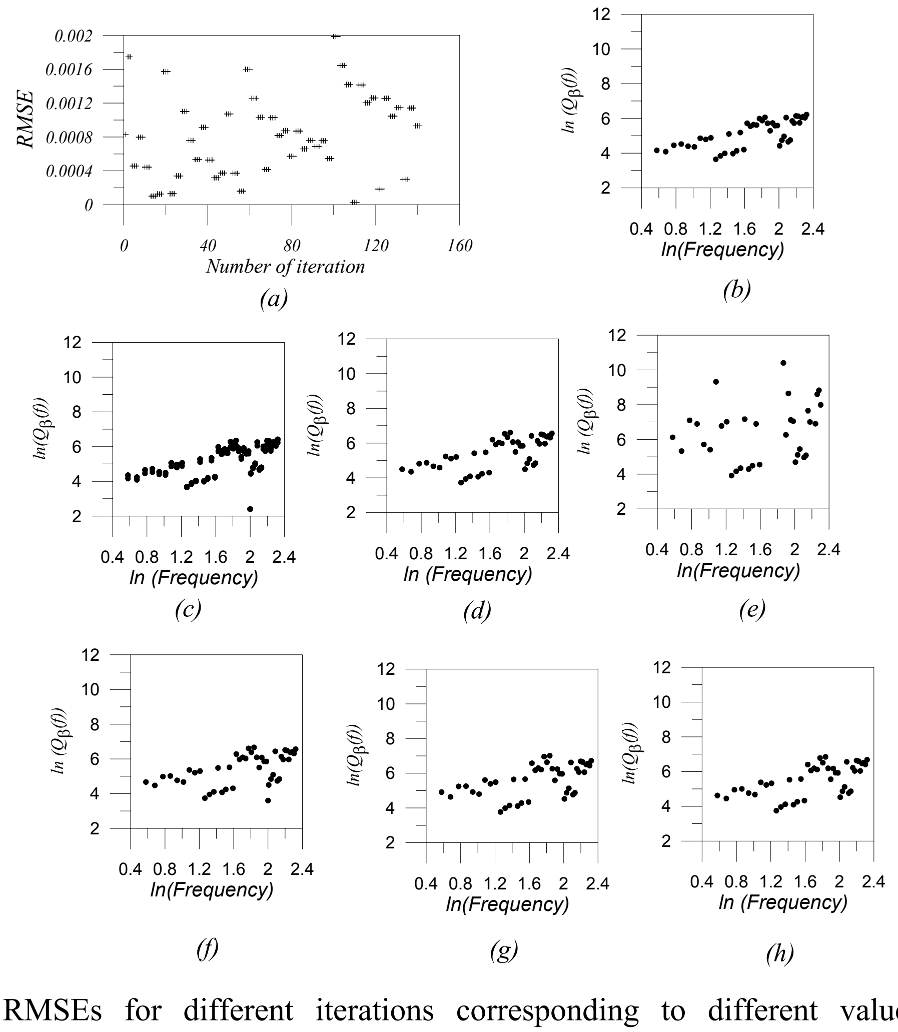


Fig. 11 (a) RMSEs for different iterations corresponding to different values of corner frequencies of selected events; Plots of $Q_\beta(f)$ versus frequency for (b) Case 1, (c) Case 2, (d) Case 3, (e) Case 4, (f) Case 5, (g) Case 6 and (h) Case 7 (the corner frequencies corresponding to different cases are given in Table 4)

Before arriving at the final $Q_\beta(f)$ relationship at each station, various time windows were considered and their effect on RMSE was observed at different stations. Table 6 shows the $Q_\beta(f)$ relation that corresponds to the minimum RMSE for the selected time window at different stations. A plot of the so-obtained variation of $Q_\beta(f)$ with frequency at different stations is shown in Figure 12. It is seen that high $Q_0$ is obtained at the Didihat and Sobla stations while a low value of $Q_0$ is obtained at the Dharchula station. RMSE is low at Pithoragarh, Dharchula and Didihat stations at which we have used the input of six and seven events, respectively. Maximum RMSE is obtained at the Sobla station where we have used the data of only three events. High RMSE is also observed at the Thal station where we have used the data of only five events. As the whole area covers the Pithoragarh region, which is mostly covered by the sequences of Lesser Himalaya, we have plotted the $Q_\beta(f)$ values obtained from inversion at all stations to obtain a regional relationship. In order to maintain the reliability of this relationship we have selected data in the frequency band of 2.0–10.0 Hz, which covers the maximum low-frequency cutoff and minimum high-frequency cutoff of the band-pass filter used in the processing of various records. The plot of $Q_\beta(f)$ versus frequency is shown in Figure 13 and the best-fit line gives a regional frequency-dependent relation as $30f^{1.45}$ which is applicable to the Pithoragarh region.

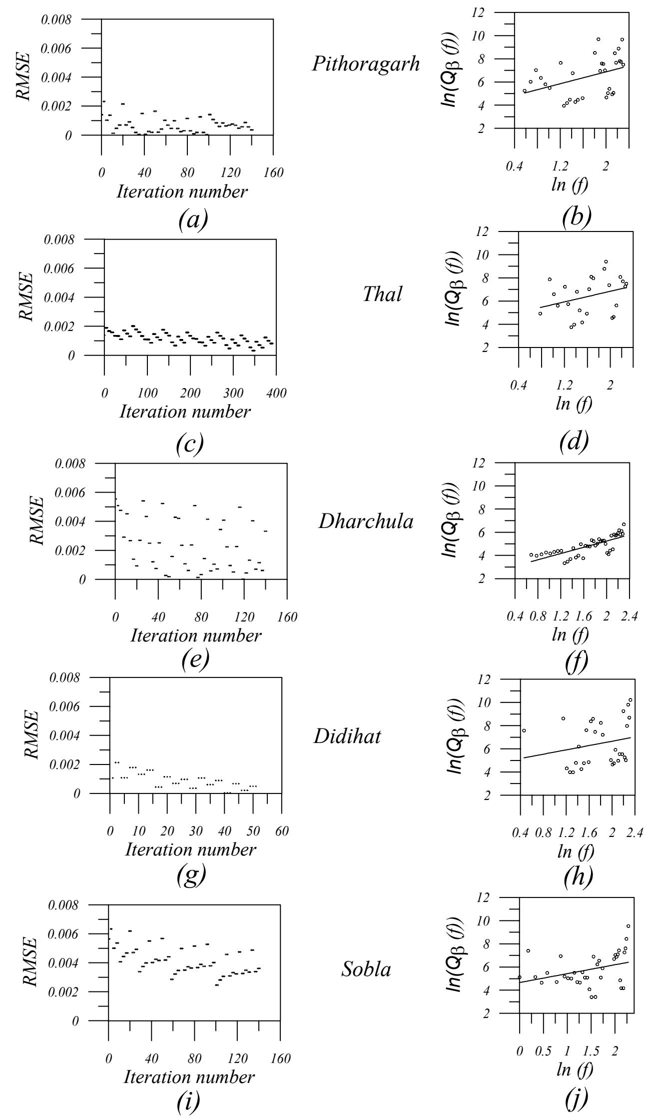


Fig. 12 Plots of RMSE at (a) Pithoragarh, (c) Thal, (e) Dharchula, (g) Didihat and (i) Sobla stations for various iterations; Plots of $Q_\beta(f)$ at (b) Pithoragarh, (d) Thal, (f) Dharchula, (h) Didihat and (j) Sobla

**Table 6: $Q_\beta(f)$ Relations Obtained at Various Stations**

| Station | Relation | RMSE |
|---|---|---|
| Pithoragarh | $73f^{1.28}$ | .000011 |
| Thal | $94f^{1.14}$ | .000318 |
| Dharchula | $13f^{1.3}$ | .000015 |
| Didihat | $120f^{0.93}$ | .000036 |
| Sobla | $105f^{0.76}$ | .001442 |

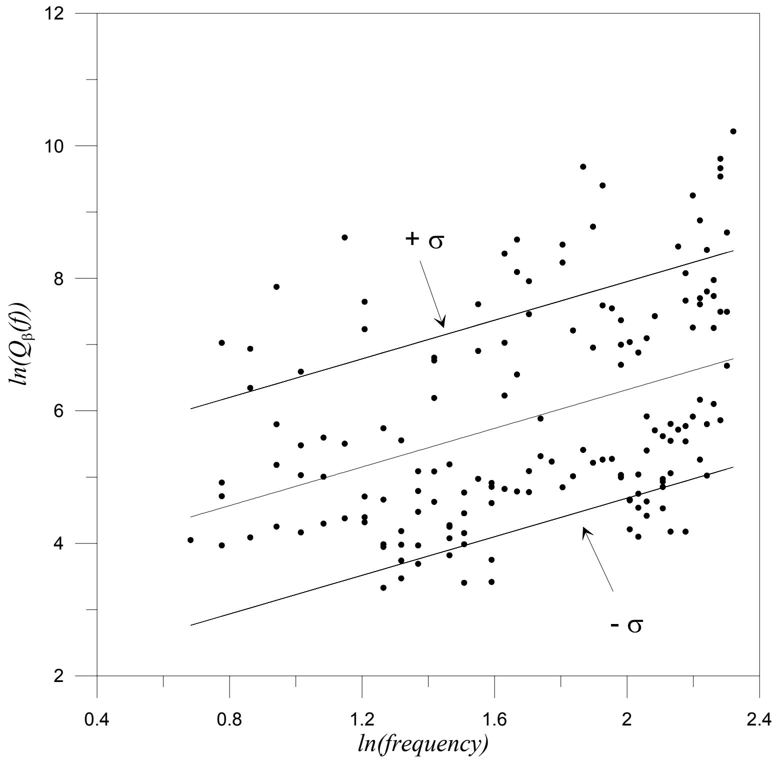


Fig. 13 Average $Q_\beta(f)$ relationship for Pithoragarh region based on the obtained values of shear wave attenuation at different stations at different frequencies

It is seen that although $Q$ is probably constant over a large frequency range in homogeneous material, this is not the case in inhomogeneous media (van der Baan, 2002). At regional distances, estimates typically show an approximately constant $Q$ for frequencies $0.28\times10^{-4}$ to 0.1 Hz (i.e., periods 10 s to 1 hr) and increase with frequency for frequencies greater than 1.0 Hz (Dziewonski, 1979; Sipkin and Jordan, 1979; Sato and Fehler, 1997). For S-waves at frequencies 1 to 25 Hz, $Q$ is proportional to $f^n$ with $n$ ranging between 0.6 and 0.8 on average (Aki, 1980; Sato and Fehler, 1997). The frequency-dependent $Q$ relation can be used to characterize the tectonic nature of the region. The relation $Q(f) = Q_0 f^n$ generally provides $Q_0$ which represents heterogeneities and $n$ represents the level of tectonic activity of the region. Regions with higher $n$ values manifest higher tectonic activity. Various studies defining the relations of frequency-dependent quality factors show that for various active regions like Guerrero (Mexico), Yugoslavia, Hindukush, South Iberia, South Spain, Garhwal Himalaya (India), North-East Himalaya (India), North-West Himalaya (India), Koyna (India), etc., $Q_0$ and $n$ vary from 47 to 169 and 0.7 to 1.05, respectively (Rodriguez et al., 1983; Rovelii, 1984; Roecker et al., 1982; Pujades et al., 1990; Ibanez et al., 1990; Gupta et al., 1995; Paul et al. 2003; Gupta and Kumar, 2002; Kumar et al., 2005; Mandal and Rastogi, 1998; Gupta et al., 1998). For the stable regions like Norway, South Carolina and North Iberia the values of $Q_0$ and $n$ vary from 190 to 600 and from 0.45 to 1.09, respectively (Kvamme and Havskov, 1989; Rhea, 1984; Pujades et al., 1990). A low $Q_0$ (< 200) and high $n$ (> 0.8) value in the relation of frequency-dependent quality factor suggests that the region is tectonically and seismically active (Kumar et al., 2005). A low $Q_0$ and high $n$ value in the developed relation for Kumaon Himalaya suggests a high level of tectonic activity in this part of the region.

Corner frequency is one of the main parameters, which is obtained from source spectra. In the present algorithm, seismic moment is used as one of the inputs. Although long-term flat level from source spectra is used for calculating seismic moment, the role of corner frequency in designing the source spectra cannot be ruled out. The corner frequency obtained from the source spectra of each event at different stations is compared with that obtained from inversion in Figure 14. It is seen that the obtained values of corner frequency of event at different stations from these two approaches do not differ significantly. However, in order to have complete unbiasness of results we need to include seismic moment in inversion at the cost of increased unknown parameters.

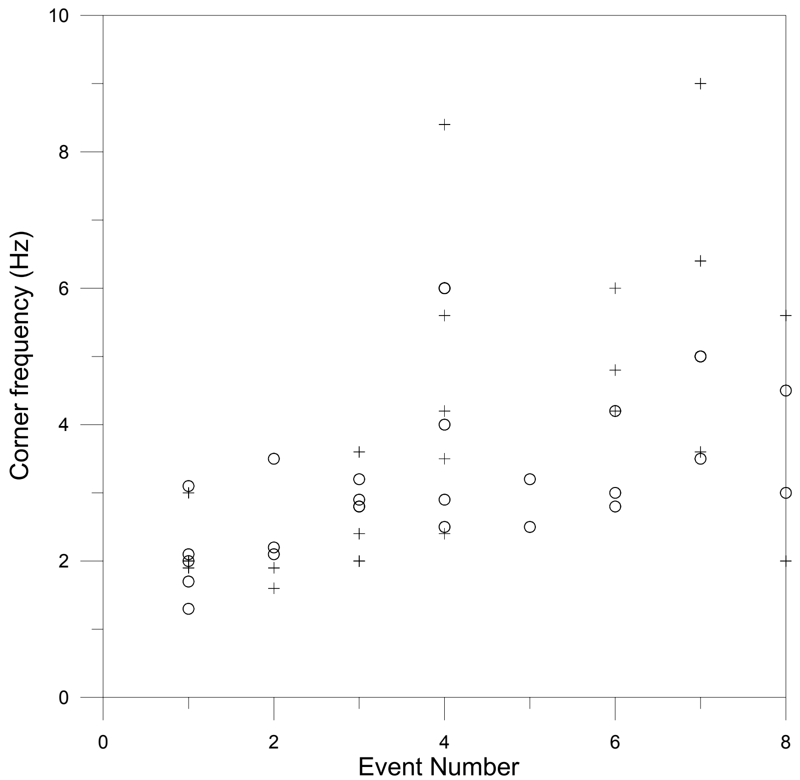


Fig. 14 Comparison of corner frequencies obtained at different stations from source displacement spectra and from present inversion (the crosses and circles show the values of corner frequencies obtained from source displacement spectra and present inversion, respectively; the $x$-axis shows the numbers corresponding to various events)

It may be mentioned that a $Q_\beta(f)$ relationship is directly used in various techniques of simulation of strong ground motion like semi-empirical modeling technique (Joshi et al., 2001; Joshi and Midorikawa, 2004), composite source-modelling technique (Zeng et al., 1994), and stochastic simulation technique (Boore, 1983). Therefore, an estimate of $Q_\beta(f)$ not only serves purpose for the attenuation properties of the region but it is also among the useful parameters needed for a successful prediction of strong ground motion for engineering use in any region as it controls shear wave attenuation in the region.

## CONCLUSIONS

In this paper, an effective algorithm for obtaining $Q_\beta(f)$ relations from strong-motion data has been presented. The data of eight events recorded at five stations located in the Pithoragarh region of Kumaon Himalayas from a local strong-motion network has been used in this study. The final $Q_\beta(f)$ is based on the solution, which gives minimum root-mean-square error in the inversion algorithm. Using recorded strong motions different $Q_\beta(f)$ relations are obtained at different stations. The $Q_\beta(f)$ obtained at different stations from inversion is used to obtain a regression relation of $Q_\beta(f) = 30 f^{1.45}$, which is applicable in a frequency range of 2.0–10.0 Hz. This $Q_\beta(f)$ relation shows that the Pithoragarh region is seismically active and is characterized by local heterogeneities. Besides estimating the nature of material between the source of an earthquake and the observation point, the developed $Q_\beta(f)$ relation can be used for a realistic simulation of strong ground motions by using the stochastic simulation technique in this part of Himalayas.

## ACKNOWLEDGEMENTS

The authors sincerely thank Department of Science and Technology, India, Indian Institute of Technology, Roorkee, Kurukshetra University, and National Geophysical Research Institute for supporting the research presented in this paper. The work presented in this paper is an outcome of the DST project grant No. DST/23(483)/SU/2004, Government of India.

## REFERENCES

1. Aki, K. and Chouet, B. (1975). “Origin of Coda Waves: Source, Attenuation and Scattering Effects”, Journal of Geophysical Research, Vol. 80, No. 23, pp. 3322–3342.
2. Aki, K. (1980). “Attenuation of Shear Waves in the Lithosphere for Frequencies from .05 to 25 Hz”, Physics of the Earth and Planetary Interiors, Vol. 21, No. 1, pp. 50–60.
3. Atkinson, G.M. and Boore, D.M. (1995). “Ground Motion Relations for Eastern North America”, Bulletin of the Seismological Society of America, Vol. 85, No. 1, pp. 17–30.
4. Atkinson, G.M. and Boore, D.M. (1998). “Evaluation of Models for Earthquake Source Spectra in Eastern North America”, Bulletin of the Seismological Society of America, Vol. 88, No. 4, pp. 917–934.
5. Bhattacharya, A.R. (1999). “Deformational Regimes across the Kumaun Himalayas: A Study in Strain Patterns” in “Geodynamics of the NW Himalaya (edited by A.K. Jain and R.M. Manickvasgam)”, Gondwana Research Group Memoir No. 6, Field Science, Osaka, Japan.
6. Boore, D.M. (1983). “Stochastic Simulation of High-Frequency Ground Motions Based on Seismological Models of the Radiated Spectra”, Bulletin of the Seismological Society of America, Vol. 73, No. 6A, pp.1865–1894.
7. Boore, D.M. and Atkinson, G.M. (1987). “Stochastic Prediction of Ground Motion and Spectral Response Parameters at Hard-Rock Sites in Eastern North America”, Bulletin of the Seismological Society of America, Vol. 77, No. 2, pp. 440–467.
8. Boore, D.M. and Bommer, J. (2005). “Processing of Strong Motion Accelerograms: Needs, Options and Consequences”, Soil Dynamics and Earthquake Engineering, Vol. 25, No. 2, pp. 93–115.
9. Brune, J.M. (1970). “Tectonic Stress and the Spectra of Seismic Shear Waves from Earthquakes”, Journal of Geophysical Research, Vol. 75, No. 26, pp. 4997–5009.
10. Converse, A.M. and Brady, A.G. (1992). “BAP: Basic Strong Motion Accelerogram Processing Software, Version 1.0”, Open File Report 92-296A, United States Geological Survey, Denver, U.S.A.
11. Dasgupta, S., Pande, P., Ganguly, D., Iqbal, Z., Sanyal, K., Venkatraman, N.V., Dasgupta, S., Sural, B., Harendranath, L., Mazumdar, K., Sanyal, S., Roy, A., Das, L.K., Misra, P.S. and Gupta, H. (2000). “Seismotectonic Atlas of India and Its Environs”, Geological Survey of India, Kolkata.

12. Dziewonski, A.M. (1979). “Elastic and Anelastic Structure of the Earth”, Reviews of Geophysics, Vol. 17, No. 2, pp. 303–312.
13. Fletcher, J.B. (1995). “Source Parameters and Crustal $Q$ for Four Earthquakes in South Carolina”, Seismological Research Letters, Vol. 66, No. 4, pp. 44–61.
14. Gupta, S.C. and Kumar, A. (2002). “Seismic Wave Attenuation Characteristics of Three Indian Regions: A Comparative Study”, Current Science, Vol. 82, No. 4, pp. 407–412.
15. Gupta, S.C., Singh, V.N. and Kumar, A. (1995). “Attenuation of Coda Waves in the Garhwal Himalaya, India”, Physics of the Earth and Planetary Interiors, Vol. 87, No. 3-4, pp. 247–253.
16. Gupta, S.C., Teotia, S.S., Rai, S.S. and Gautam, N. (1998). “Coda $Q$ Estimates in the Koyna Region, India”, Pure and Applied Geophysics, Vol. 153, No.2-4, pp. 713–731.
17. Hanks, T.C. and McGuire, R.K. (1981). “The Character of High Frequency Strong Ground Motion”, Bulletin of the Seismological Society of America, Vol. 71, No. 6, pp. 2071–2095.
18. Ibáñez, J.M., Del Pezzo, E., De Miguel, F., Herraiz, M., Alguacil, G. and Morales, J. (1990). “Depth-Dependent Seismic Attenuation in the Granada Zone (Southern Spain)”, Bulletin of the Seismological Society of America., Vol. 80, No. 5, pp. 1232–1244.
19. Joshi, A. (2000). “Modelling of Rupture Planes for Peak Ground Accelerations and Its Application to the Isoseismal Map of MMI Scale in Indian Region”, Journal of Seismology, Vol. 4, No. 2, pp. 143–160.
20. Joshi, A. (2006). “Use of Acceleration Spectra for Determining the Frequency-Dependent Attenuation Coefficient and Source Parameters”, Bulletin of the Seismological Society of America, Vol. 96, No. 6, pp. 2165–2180.
21. Joshi, A. and Midorikawa, S. (2004). “A Simplified Method for Simulation of Strong Ground Motion Using Rupture Model of the Earthquake Source”, Journal of Seismology, Vol. 8, No. 4, pp. 467–484.
22. Joshi, A., Singh, S. and Giroti, K. (2001). “The Simulation of Ground Motions Using Envelope Summations”, Pure and Applied Geophysics, Vol. 158, No. 5-6, pp. 877–902.
23. Keilis-Borok, V.I. (1959). “On the Estimation of the Displacement in an Earthquake Source and of Source Dimensions”, Annali di Geofisica, Vol. XII, No. 2, pp. 205–214.
24. Kumar, N., Parvez, I.A. and Virk, H.S. (2005). “Estimation of Coda Wave Attenuation for NW Himalayan Region Using Local Earthquakes”, Physics of the Earth and Planetary Interiors, Vol. 151, No. 3-4, pp. 243–258.
25. Kvamme, L.B. and Havskov, J. (1989). “$Q$ in Southern Norway”, Bulletin of the Seismological Society of America, Vol. 79, No. 5, pp. 1575–1588.
26. Lanczos, C. (1961). “Linear Differential Operators”, D. Van Nostrand Co., London, United Kingdom.
27. Lee, W.H.K. and Lahr, J.C. (1972). “HYPO71: A Computer Program for Determining Hypocenter, Magnitude, and First Motion Pattern of Local Earthquakes”, Open File Report, United States Geological Survey, Denver, U.S.A.
28. Mandal, P. and Rastogi, B.K. (1998). “A Frequency-Dependent Relation of Coda $Q_c$ for Koyna Warna Region, India”, Pure and Applied Geophysics, Vol. 153, No. 1, pp. 163–178.
29. Mandal, P., Pandhy, S., Rastogi, B.K., Satyanarayana, V.S., Kousalya, M., Vijayraghavan, R. and Srinivasan, A. (2001). “Aftershock Activity and Frequency-Dependent Low $Q_c$ in the Epicentral Region of 1999 Chamoli Earthquake of $M_W$ 6.4”, Pure and Applied Geophysics, Vol. 158, No. 9-10, pp. 1719–1736.
30. Paul, A., Gupta, S.C. and Pant, C.C. (2003). “Coda $Q$ Estimates for Kumaun Himalaya”, Proceedings of the Indian Academy of Sciences (Earth and Planetary Sciences), Vol. 112, No. 4, pp. 569–576.
31. Pelton, J.R. (2005). “Near-Surface Seismology: Wave Propagation” in “Near Surface Geophysics (edited by D.K. Butler)”, Society of Exploration Geophysicists, Tulsa, U.S.A.
32. Press, W.H., Teukolsky, S.A., Vetterling, W.T. and Flannery, B.P. (1992). “Numerical Recipes”, Cambridge University Press, New York, U.S.A.

33. Pujades, L.G., Canas, J.A., Egozcue, J.J., Puigvi, M.A., Gallart, J., Lana, X., Pous, J., Casas, A. (1990). "Coda $Q$ Distribution in the Iberian Peninsula", Geophysical Journal International, Vol. 100, No. 2, pp. 285–301.
34. Rhea, S. (1984). "$Q$ Determined from Local Earthquakes in the South Carolina Coastal Plain", Bulletin of the Seismological Society of America, Vol. 74, No. 6, pp. 2257–2268.
35. Rodriguez, M., Havskov, J. and Singh, S.K. (1983). "$Q$ from Coda Waves Near Petatlan, Guerrero, Mexico", Bulletin of the Seismological Society of America, Vol. 73, No. 1, pp. 321–326.
36. Roecker, S.W., Tucker, B., King, J. and Hartzfeld, D. (1982). "Estimates of $Q$ in Central Asia as a Function of Frequency and Depth Using the Coda of Locally Recorded Earthquakes", Bulletin of the Seismological Society of America, Vol. 72, No. 1, pp. 129–149.
37. Rovelli, A. (1984). "Seismic $Q$ for Lithosphere of Montenegro Region (Yugoslavia): Frequency, Depth and Time Windowing Effects", Physics of the Earth and Planetary Interiors, Vol. 34, No. 3, pp. 159–172.
38. Sato, H. and Fehler, M.C. (1997). "Seismic Wave Propagation and Scattering in the Heterogeneous Earth", Springer Verlag, Berlin, Germany.
39. Shakal, A.F., Huang, M.-J. and Graizer, V.M. (2004). "California: Strong Motion Instrumentation Program Record Processing Methods and Procedures" in "Proceedings of Invited Workshop on Strong Motion Record Processing (edited by D.M. Boore, B.S.-J. Chiou, W.D. Iwan, D.R. O'Connell, A.F. Shakal, J.C. Stepp and C.M. Johnson)", COSMOS Publication CP-2004/02, Richmond, U.S.A.
40. Sharma, M.L. and Wason, H.R. (1994). "Occurrence of Low Stress Drop Earthquakes in the Garhwal Himalaya Region", Physics of the Earth and Planetary Interiors, Vol. 85, No. 3-4, pp. 265–272.
41. Singh, S.K., Iglesias, A., Dattatrayam, R.S., Bansal, B.K., Rai, S.S., Perez-Campos, X., Suresh, G., Baidya, P.R. and Gautam, J.L. (2006). "Muzaffarabad Earthquake of 8 October 2005 ($M_W$ 7.6): A Preliminary Report on Source Characteristics and Recorded Ground Motions", Current Science, Vol. 91, No. 5, pp. 689–695.
42. Sipkin, S.A. and Jordan, T.H. (1979). "Frequency Dependence of $Q_{ScS}$", Bulletin of the Seismological Society of America, Vol. 69, No. 4, pp. 1055–1079.
43. Toksöz, M.N., Johnston, D.H. and Timur, A. (1979). "Attenuation of Seismic Waves in Dry and Saturated Rocks—I. Laboratory Measurements", Geophysics, Vol. 44, No. 4, pp. 681–690.
44. Trifunac, M.D. (1977). "Uniformly Processed Strong Motion Earthquake Ground Accelerations in the Western United States of America for Period from 1933 to 1971: Pseudo Relative Velocity Spectra and Processing Noise", Report USC/CE-77-04, University of Southern California, Los Angeles, U.S.A.
45. Valdiya, K.S. (1999). "Fast Uplift and Geomorphic Development of the Western Himalaya" in "Geodynamics of the NW Himalaya (edited by A.K. Jain and R.M. Manickvasgam)", Gondwana Research Group Memoir No. 6, Field Science, Osaka, Japan.
46. van der Baan, M. (2002). "Constant $Q$ and a Fractal Stratified Earth", Pure and Applied Geophysics, Vol. 159, No. 7-8, pp. 1707–1718.
47. Yang, X., Lay, T., Xie, X.B. and Thorne, M.S. (2007). "Geometric Spreading of $P_n$ and $S_n$ in a Spherical Earth Model", Bulletin of the Seismological Society of America, Vol. 97, No. 6, pp. 2053–2065.
48. Zeng, Y., Anderson, J.G. and Yu, G. (1994). "A Composite Source Model for Computing Realistic Synthetic Strong Ground Motions", Geophysical Research Letters, Vol. 21, No. 8, pp. 725–728.

ISET Journal of Earthquake Technology, Paper No. 509, Vol. 47, No. 1, March 2010, pp. 47–60

# STRUCTURAL HEALTH MONITORING VIA STIFFNESS UPDATE

Prashant V. Pokharkar and Manish Shrikhande
Department of Earthquake Engineering
Indian Institute of Technology Roorkee
Roorkee–247667

## ABSTRACT

The performance of an updated time-domain least-squares identification method for identifying a reduced-order linear system model in the case of limited response measurements and its use in structural health monitoring is evaluated. It is shown that the incorporation of a mass-invariability constraint enhances the robustness of the parametric identification procedure. The full structural stiffness and mass matrices are identified from the identified reduced-order model by using the condensed model identification and recovery method. The damage state is considered to be represented by an incremental stiffness degradation model. The degradation in stiffness is estimated through the minimization of an error function defined in terms of Rayleigh quotients. The performance of the proposed scheme is examined with reference to the simulated damage due to earthquake excitation in a 10-story building with rigid floor diaphragm.

**KEYWORDS:** Detection, Dynamic Condensation, Least-Squares Identification, Structural Health Monitoring, System Identification

## INTRODUCTION

Structural system identification has gained in importance over the last couple of years as a diagnostic tool for the structural health assessment—primarily due to the requirements of enhanced functionality and reduced downtime of buildings and services. The conventional approaches to structural health assessment require physical access to the regions of interest in the structural system and are also very tedious and time consuming. The damage/degradation in structures causes reduction of natural frequencies, increased energy dissipation, and changes in the mode shapes. Therefore, monitoring of vibration characteristics of structural system should permit the detection of both the location and severity of damage. The vibration-based system identification and health assessment is promising because substantial information can be gathered by only a few sensors distributed across the structural system. The system identification approaches can be classified as either parametric or non-parametric methods. In parametric methods, the structural models to be identified are characterized in terms of a finite set of parameters, such as the coefficients of the governing differential equations of motion, or the coefficients of the rational polynomial approximation for transfer function, etc. The non-parametric methods, on the other hand, characterize the dynamic systems in terms of impulse response functions, or frequency response functions derived from the direct measurements of excitation and response at various locations in the structural system.

As the stiffness characteristics are most prominently influenced by the damage, if any, in the structural systems, several approaches have been developed to identify stiffness, or related characteristics of a structural system from the analysis of its vibration signatures. Udwadia (2005) presented a method for the identification of the stiffness matrices of a structural system from the information about some of its observed frequencies and corresponding mode shapes of vibration. Pandey and Biswas (1994) suggested the use of mode shape curvature in detecting damage. For large and/or complex structures, however, the changes in mode shapes and their curvatures may be so small that their use for the detection of damage might not be practical. Stubbs et al. (1995) developed a methodology based on the comparison of modal strain energy before and after damage to identify damage in structure. However, except for very simple structures, moderate damage does not significantly affect the lower modes of vibration, which can be identified with greater reliability. Baruch and Bar Itzhack (1978) proposed a matrix update method, wherein a norm of the global parameter matrix perturbations is minimized with the application of symmetry constraint on property matrix. Many other approaches developed in this area are based on the minimization of the rank of perturbed matrix with connectivity and sparsity constraint on the original matrix. In large scale complex structural systems the natural frequencies and mode shapes towards the higher end of the spectrum can rarely be identified with sufficient accuracy, which in turn affect the reliability of damage detection on the basis of mode shape information. Agbabian et al. (1990) and Smyth et al. (2000) proposed a least-squares method for the parametric identification of a linear system for estimating the coefficients of the governing differential equation. For a limited number of sensors to record the vibration response, the time-domain least-squares identification procedure yields the minimum norm estimates for the coefficients of the reduced order system, which may be significantly different from the 'true' coefficients (Choudhury, 2007). This problem of non-uniqueness of the results of time-domain least-squares identification procedure is addressed in this study. Reduced-order equivalent linear models are identified for different time windows. The full system matrices are recovered from the estimated reduced order models and an attempt is made to detect the presence of damage by tracking the changes in the stiffness coefficients of the recovered full stiffness matrix of the structure. The performance of this scheme is examined with the help of a simple analytical model for a steel structural frame with rigid floor diaphragms and subjected to earthquake excitation.

## TIME-DOMAIN LEAST-SQUARES IDENTIFICATION

Let us consider the governing equations of motion for a multi-degree-of-freedom (MDOF) system subjected to the external forces $\{f\}$:

$$[M]\{\ddot{y}\}+[C]\{\dot{y}\}+[K]\{y\}=\{f\} \tag{1}$$

where, $[M]$, $[C]$ and $[K]$ are the mass, damping and stiffness matrices of the system and $\{y\}$ represents the vector of deformations at each degree of freedom (DOF). In practice, the system response is recorded only at a few select DOFs corresponding to the sensor locations, and we consider these DOFs as primary (or master) DOFs. The least-squares parametric identification would allow us to estimate the coefficients of the reduced-order model consisting only of the primary DOFs. By partitioning the vector of deformations as $\{y\}=\left\{\{y_s\}^T,\{y_p\}^T\right\}^T$, where $\{y_p\}$ and $\{y_s\}$ denote the primary and secondary DOFs, respectively, the system considered for identification is

$$[\bar{M}]\{\ddot{y}_p\}+[\bar{C}]\{\dot{y}_p\}+[\bar{K}]\{y_p\}\approx\{\bar{f}_p\} \tag{2}$$

where, $[\bar{M}]$, $[\bar{C}]$ and $[\bar{K}]$ denote the inertia, damping and stiffness characteristics of the structural system after condensing out the secondary DOFs. The vector $\{\bar{f}_p\}$ represents the equivalent forces on the primary DOFs and depends on the transformation of the full analytical model of Equation (1) to the reduced-order model of Equation (2). Assuming that a total of $n_p$ number of response measurements are available at different sensor locations, a vector of responses, say $\{r_i\}$ $(\in\mathbb{R}^{1\times 3n_p})$, at the $i$th time instant can be constructed as

$$\{r_i\}=\left\{\ddot{y}_1(t_i)\ldots\ddot{y}_{n_p}(t_i),\dot{y}_1(t_i)\ldots\dot{y}_{n_p}(t_i),y_1(t_i)\ldots y_{n_p}(t_i)\right\} \tag{3}$$

Considering the response at all time instants ($t_1$ through $t_n$), a response matrix $[R]$ $(\in\mathbb{R}^{n\times 3n_p})$ can be defined as

$$[R]=\begin{bmatrix}\{r_1\}\\\{r_2\}\\\vdots\\\{r_n\}\end{bmatrix} \tag{4}$$

The coefficients of Equation (2) corresponding to each primary DOF may be arranged as

$$\left\{\alpha_j\right\} = \left\{\bar{m}_{j1},\ldots,\bar{m}_{jn_p},\bar{c}_{j1},\ldots,\bar{c}_{jn_p},\bar{k}_{j1},\ldots,\bar{k}_{jn_p}\right\}; \quad j = 1,2,\ldots,n_p \tag{5}$$

where $\bar{m}_{j1}$, $\bar{c}_{j1}$ and $\bar{k}_{j1}$, respectively, denote the coefficients of the condensed system matrices $\left[\bar{M}\right]$, $\left[\bar{C}\right]$ and $\left[\bar{K}\right]$, and $\left\{\alpha_j\right\}$ ($\in \mathbb{R}^{1\times 3n_p}$) is the arrangement of these coefficients of the $j$th row in a row vector. Equation (2) can then be rearranged in the form:

$$\left[\hat{R}\right]\left\{\hat{\alpha}\right\} = \left\{\hat{b}\right\} \tag{6}$$

where $\left[\hat{R}\right]$ ($\in \mathbb{R}^{nn_p\times 3n_p^2}$) is a block diagonal matrix with the response matrix $\left[R\right]$ on its diagonal, $\left\{\hat{\alpha}\right\}$ ($\in \mathbb{R}^{3n_p^2\times 1}$; $= \left\{\left\{\alpha_j\right\},\ldots,\left\{\alpha_{n_p}\right\}\right\}^T$), and $\left\{\hat{b}\right\}$ ($\in \mathbb{R}^{nn_p\times 1}$) is the vector of corresponding excitation measurements given by

$$\left[\hat{b}\right] = \begin{bmatrix} \left\{b_1\right\} \\ \left\{b_2\right\} \\ \vdots \\ \left\{b_{n_p}\right\} \end{bmatrix} \tag{7}$$

with $\left\{b_j\right\} = \left\{\bar{f}_j\left(t_1\right),\bar{f}_j\left(t_2\right),\ldots,\bar{f}_j\left(t_n\right)\right\}^T$, $j = 1,2,\ldots,n_p$. Here, $\bar{f}_j\left(t_i\right)$, $j = 1,2,\ldots,n_p$ denotes the equivalent forces on the primary degrees of freedom of the condensed system at time $t_i$ and are described in the following section. The least-squares solution of Equation (6) may be then obtained as

$$\left\{\hat{\alpha}\right\} = \left[\hat{R}\right]^{\dagger}\left\{\hat{b}\right\} \tag{8}$$

where $\left[\hat{R}\right]^{\dagger}$ is the Moore-Penrose pseudo-inverse (Golub and Van Loan, 1996) of $\left[\hat{R}\right]$. The least-squares solution computed in Equation (8) corresponds to the solution of associated normal equations ($\left[\hat{R}\right]^T\left[\hat{R}\right]\left\{\hat{\alpha}\right\} = \left[\hat{R}\right]^T\left\{\hat{b}\right\}$). The solution vector $\left\{\hat{\alpha}\right\}$ provides the minimum-norm least-squares estimates of the desired system parameters. It is often required to improve the numerical conditioning of the system of equations and also to impose the constraint of symmetry of coefficient matrices to eliminate physically inconsistent results of system identification.

## ANALYTICAL REDUCTION OF SYSTEM MATRICES

Since the above-mentioned time-domain least-squares parametric identification procedure can only identify a reduced-order model corresponding to the primary DOFs (Smyth et al., 2000), it is desirable to have a set of benchmark values for assessing the quality of parameter estimates before using the results of this identification procedure to draw further inferences. A comparable reduced-order system model can be obtained by the elimination of secondary DOFs from the system of equations by using the dynamic condensation method (Paz, 1984, 2004). Let us write the equations of motion for free vibration in partitioned matrix form as

$$\begin{bmatrix} \left[K_{ss}\right] - \omega_i^2\left[M_{ss}\right] & \left[K_{sp}\right] - \omega_i^2\left[M_{sp}\right] \\ \left[K_{ps}\right] - \omega_i^2\left[M_{ps}\right] & \left[K_{pp}\right] - \omega_i^2\left[M_{pp}\right] \end{bmatrix}\begin{Bmatrix} \left\{y_s\right\} \\ \left\{y_p\right\} \end{Bmatrix} = \begin{Bmatrix} \left\{0\right\} \\ \left\{0\right\} \end{Bmatrix} \tag{9}$$

from which the secondary variables can be eliminated as

$$\left\{y_s\right\} = -\left(\left[K_{ss}\right] - \omega_i^2\left[M_{ss}\right]\right)^{-1}\left(\left[K_{sp}\right] - \omega_i^2\left[M_{sp}\right]\right)\left\{y_p\right\} = \left[T_i\right]\left\{y_p\right\} \tag{10}$$

where $\omega_i^2$ is an approximation for the $i$th eigenvalue of the structural system, and $[T_i]= -\left([K_{ss}]-\omega_i^2[M_{ss}]\right)^{-1}\left([K_{sp}]-\omega_i^2[M_{sp}]\right)$ represents the transformation matrix relating the primary (master) DOFs to the secondary (slave) DOFs for the current approximation of the $i$th eigenvalue obtained from the reduced-order system containing only primary DOFs. The full DOFs-vector $\left\{\{y_s\}^T,\{y_p\}^T\right\}^T$ may be then expressed in terms of the primary DOFs as

$$\begin{Bmatrix}\{y_s\}\\ \{y_p\}\end{Bmatrix}=\begin{bmatrix}[T_i]\\ [I]\end{bmatrix}\{y_p\}=\left[\bar{T}_i\right]\{y_p\} \tag{11}$$

where $[I]$ denotes an identity matrix and $\left[\bar{T}_i\right]$ is the matrix relating the full-DOFs vector to the primary DOFs. The reduced mass and stiffness matrices are then obtained as

$$\left[\bar{M}_i\right]=\left[\bar{T}_i\right]^T[M]\left[\bar{T}_i\right] \text{ and } \left[\bar{K}_i\right]=\left[\bar{D}\right]+\omega_i^2\left[\bar{M}_i\right] \tag{12}$$

with

$$\left[\bar{D}\right]=\left([K_{pp}]-\omega_i^2[M_{pp}]\right)+\left([K_{ps}]-\omega_i^2[M_{ps}]\right)[T_i] \tag{13}$$

These reduced-order system matrices are used to calculate an improved estimate of the $i$th eigenvalue, which is then substituted in Equation (13) and the iterative process is repeated until the eigenvalue is close enough to that for the full model. This process may be repeated for estimating the next eigenvalue. Since the reduced mass and stiffness matrices are influenced by the choice of natural frequency, an iterative scheme is necessary to converge to a set of reduced matrices which have the same natural frequencies in the lower half of the spectrum as those calculated for the full-order system. The final reduced-order matrices can be used for the modeling of the forced vibration problem, for which the response is only monitored at the primary DOFs. The modified force vector for the reduced-order model in the case of excitation by base motion may be expressed as

$$\left\{\bar{f}_p\right\}=-\left[\bar{T}_i\right]^T\begin{bmatrix}[M_{ss}] & [M_{sp}]\\ [M_{ps}] & [M_{pp}]\end{bmatrix}\{1\}\ddot{u}_g(t) \tag{14}$$

where $\left[\bar{T}_i\right]$ is the transformation relating the DOFs of the chosen reduced-order analytical model to the DOFs of the full analytical model—as defined in Equation (11). The damping matrix is not considered in the condensation scheme as the level of damping forces is, generally, very small in structural systems, particularly so in the case of steel structures.

The example structural system considered in this study is an intermediate frame of a ten-story steel building with two bays as shown in Figure 1. The Indian standard rolled beam section ISMB-225 (BIS, 1989) with yield strength $f_y$ of 250 MPa and Young's modulus $E$ of $2\times10^5$ MPa are used for modeling the frame in the SAP2000 structural analysis software. A perfect elasto-plastic constitutive behaviour is assumed. As a first-order approximation to the structural behaviour and also for reducing the problem size, the rigid floor diaphragm assumption is made and the vertical and rotational DOFs are also restrained. This reduces the total number of unrestrained DOFs to 10. The numerals on the right side of the frame in Figure 1 indicate the DOF numbers associated with different floors (assigned internally in SAP2000 after imposing the rigid floor diaphragm constraint). A modal damping ratio of $\zeta$ = 0.05 is assumed. The undamped natural frequencies of this system are found to be $\omega_i$ = 4.049, 12.048, 19.755, 26.983, 33.560, 39.331, 44.169, 47.978, 50.702, 52.326 rad/s. The building response data is assumed to be recorded at the 1st, 4th, 8th and 10th floors, which correspond to the optimal locations for a 10-story building with rigid floor diaphragms (Heredia-Zavoni and Esteva, 1998; Datta et al., 2002). The DOFs associated with these floors, i.e., 2, 3, 9, and 6, respectively, are designated as the primary DOFs and the remaining DOFs (i.e., secondary DOFs) are condensed out by the dynamic condensation procedure. The reduced system matrices are obtained as

$$\left[\bar{M}\right] = \begin{bmatrix} 0.977 & 0.279 & 0.000 & 0.000 \\ 0.279 & 1.527 & 0.392 & 0.000 \\ 0.000 & 0.392 & 1.335 & 0.157 \\ 0.000 & 0.000 & 0.157 & 0.624 \end{bmatrix} \times 10^6 \text{ kg}$$

and (15)

$$\left[\bar{K}\right] = \begin{bmatrix} 5.850 & -1.46 & 0.000 & 0.000 \\ -1.46 & 2.560 & -1.10 & 0.000 \\ 0.00 & -1.10 & 3.290 & -2.19 \\ 0.00 & 0.00 & -2.19 & 2.190 \end{bmatrix} \times 10^8 \text{ N/m}$$

These matrices will now be used as benchmarks for comparing the system matrices estimated by the least-squares identification process.

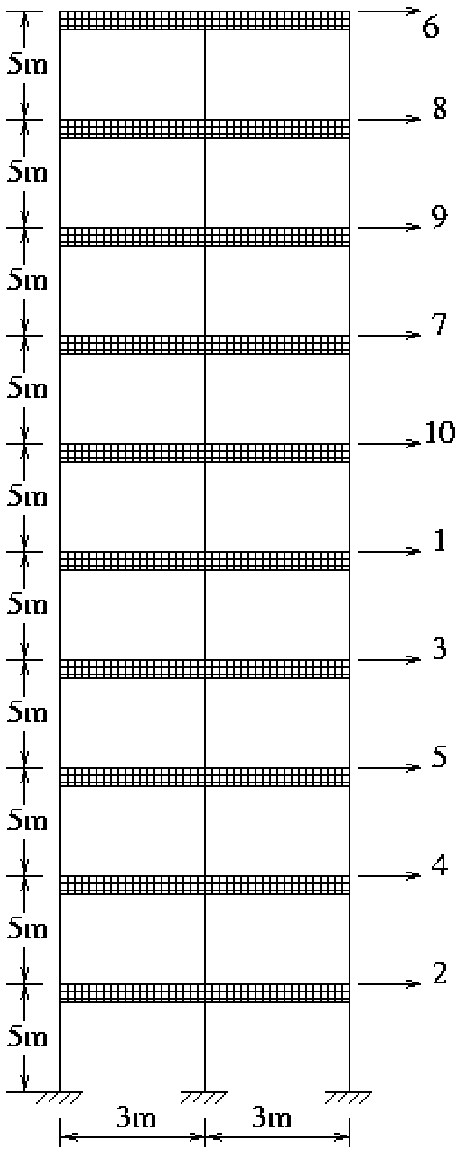


Fig. 1 Structural frame used for analysis

## DATASET FOR SYSTEM IDENTIFICATION

In the time-domain least-squares system identification approach, it is necessary to have the excitation and the response data of the system. The building response data is generated through a non-linear dynamic analysis of an analytical model in the SAP2000 environment. The dataset consists of relative displacement, relative velocity and relative acceleration responses at each of the designated floors assumed to have vibration sensors, namely, the 1st, 4th, 8th and 10th (roof) floors. A scaled time history (with the scale factor of 2) of the Northridge, California earthquake ground motion recorded at Pacoima Dam Upper Left Abutment (with the closest distance of 8 km to the fault rupture) on January 17, 1994 for the component 104 (as in the PEER database[1]) and sampling interval of 0.02 s is considered as the base excitation. This ground motion has the peak ground acceleration (PGA) of 1.58*g*. Figure 2 shows the (unscaled) time history of this ground motion.

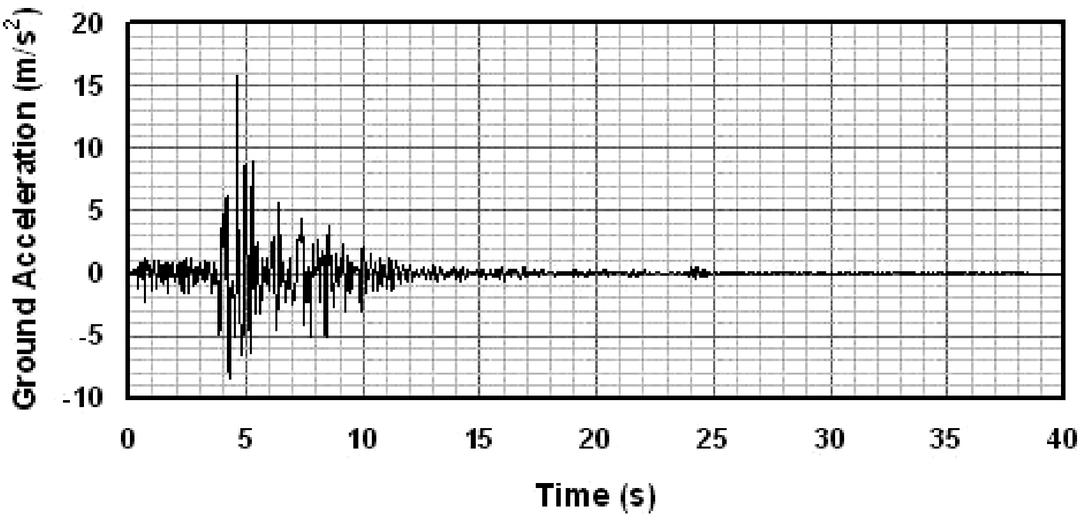


Fig. 2 Northridge earthquake ground acceleration time history

The recorded time history is scaled (by a factor of 2) to enforce the development of plastic hinges in the structural frame during the shaking. A zero-mean Gaussian random noise is added to simulate the effect of measurement noise such that $\sigma_n = 0.05\sigma_s$, where $\sigma_n$ denotes the standard deviation of noise and $\sigma_s$ represents the standard deviation of the actual time-domain signal. A representative plot of the computed relative acceleration, velocity and displacement time histories at the 10th floor is shown in Figure 3. All time histories are sampled at 0.02 s interval. In the case of seismic excitations, response data is generally acquired by using accelerometers, which record absolute accelerations at the base of the transducers. The relative acceleration response is then obtained by subtracting the base acceleration from the recorded floor accelerations. The velocity and displacement time histories are obtained by integrating the acceleration time history filtered to correct for baseline errors. These time histories are then used for the least-squares system identification. However, considering the full-duration data at once smears away the time-varying information and one only gets gross time-averaged information to draw inferences. Since the damage of building frame during an earthquake is a gradual process, it is expected that this effect should be noticeable in the parameter estimates obtained from the data segments from small time windows. The length of the data window is an important consideration for any such moving window analysis and is decided by examining the temporal evolution of the frequency content in the structural response time history. The temporal evolution is depicted by the spectrogram, i.e., the plot of the squared amplitude of the short time Fourier transform (STFT) of the response time history. The STFT of a signal may be defined as

$$Sf(t,\omega) = \int_{-\infty}^{\infty} f(u)g(u-t)e^{-iwu}\mathrm{d}u \qquad (16)$$

[1] Website of PEER Strong Motion Database, http://peer.berkeley.edu/smcat/ (last accessed on January 2, 2010)

where $g(u-t)$ denotes a real, symmetric window in time domain and serves to localize the Fourier integral in the neighbourhood of $u = t$. The spectrogram is defined as the energy density of the STFT as

$$S(t,\omega) = |Sf(t,\omega)|^2 \tag{17}$$

The length of window function is an important factor in STFT-based time-frequency analyses—too short a window enhances the resolution in time at the cost of poor resolution in frequency domain, whereas too long a window provides a sharp spectral resolution with low resolution in time domain. In this study a 256-sample Hann window with 0.9 overlap factor is used for calculating spectrograms. The variation of the energy of various harmonics in a signal with respect to time is color coded with large amplitudes shown in red to very small amplitudes shown in violet colour. Figure 4 shows the spectrograms of the ground motion and the relative acceleration response at the roof level of the example building.

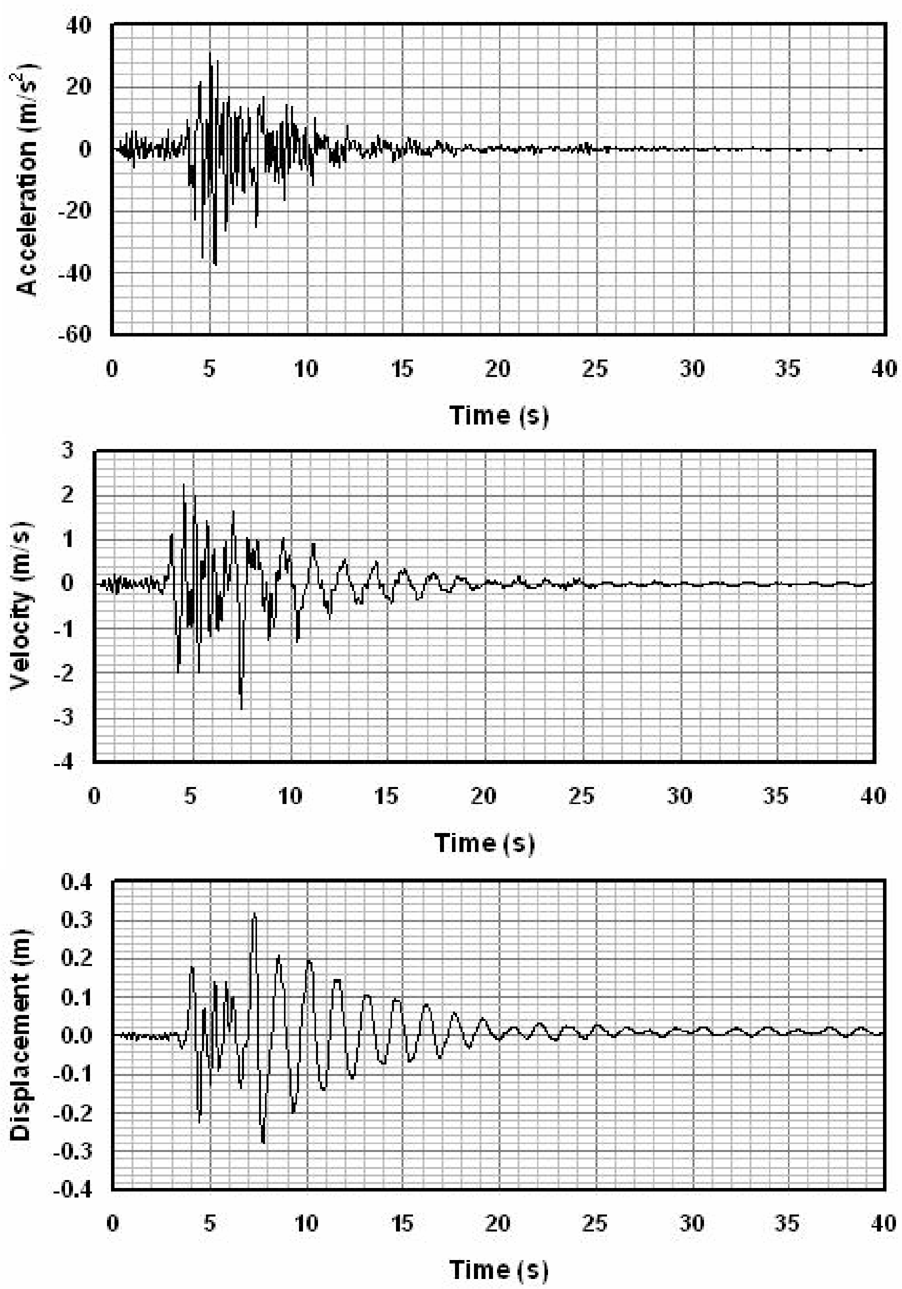


Fig. 3 Computed relative acceleration, velocity and displacement time histories at the 10th floor

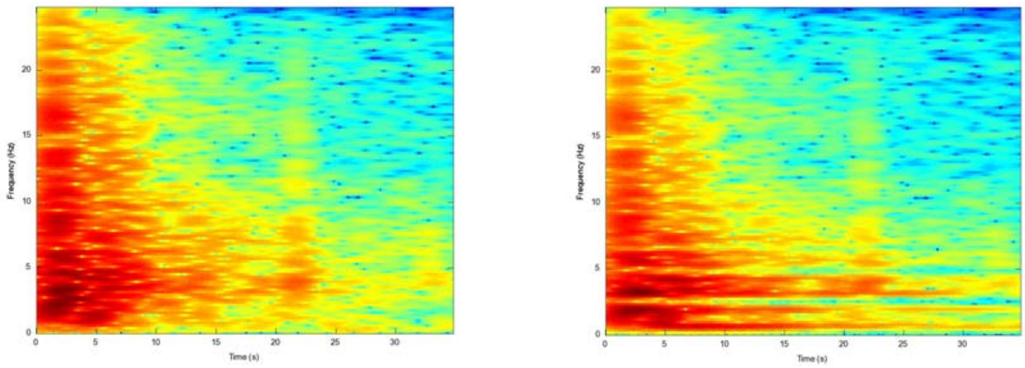

(a) Ground motion (b) Relative acceleration at roof level

Fig. 4 Spectrograms of the acceleration time histories

From the examination of the above spectrograms and the time histories (as shown in Figures 2 and 3), it may be seen that the period of strong shaking, marked by the S-wave arrival, commences after about 4 s from the onset of shaking. This time span of 4 s is also marked by an almost uniform distribution of energy with respect to frequencies. A time window of 4-s length is therefore considered to be adequate to capture the time-varying characteristics in the dataset. Moreover, the data after 20 s can be neglected from the moving window analysis as the amplitude of shaking is very small and is therefore inconsequential for the purpose of damage detection. This reduces the total time frame for the dataset to 20 s with 5 time windows of 4 s each.

**LEAST-SQUARES IDENTIFICATION RESULTS**

Since the least-squares solution procedure yields a minimum-norm solution for the unknown system parameters, the estimated coefficients for the reduced-order model can be greatly underestimated (Choudhury, 2007) and a suitable constraint on the possible solutions is desirable. As the process of damage in a structural system during an earthquake does not lead to any changes in the mass/inertia characteristics of the structure, this constraint of the mass invariance can be imposed on the possible solutions of the least-squares identification. This mass-invariance constraint is imposed by including a requisite number (i.e., as many as the number of mass terms in the parameter vector $\{\hat{\alpha}\}$) of the identities of the type

$$\beta m_{ij} = \beta m_{ij}^{*} \tag{18}$$

to the system of equations given by Equation (6). Here, $m_{ij}^{*}$ denote the analytically computed mass coefficients of the reduced-order model as in Equations (15) and (18). This process is similar to the 'stiff spring' approach for imposing prescribed values for some variables in a system of linear algebraic equations. The coefficient $\beta$ should be chosen large enough so that the mass-invariance identity has substantial weight in the solution of equations. A good choice is to consider $\beta$ to be $10^3$–$10^5$ times the largest coefficient in $\left[R\right]$. The augmented system of equations for the least-squares solution after the inclusion of mass-invariance constraint may be expressed as

$$\begin{bmatrix} \left[\hat{R}\right] \\ \left[R_{\text{mic}}\right] \end{bmatrix} \{\hat{\alpha}\} = \begin{Bmatrix} \{\hat{b}\} \\ \left[R_{\text{mic}}\right]\{\hat{\alpha}^{*}\} \end{Bmatrix} \tag{19}$$

where $\left[R_{\text{mic}}\right]$ is a matrix of $\beta$s and $0$s such that the mass-invariant constraint can be incorporated. Another physical constraint of the symmetry of mass and stiffness matrices is imposed by considering coefficients from the upper triangular regions only in the parameter vector $\{\hat{\alpha}\}$ in Equation (19) and by rearranging the elements of $\left[\hat{R}\right]$ so as to associate the multiple of an element of lower triangular part with its symmetric counterpart in the upper triangular part (Smyth et al., 2000). For the example building and the dataset for the first time window of 4 s, the identified system parameters for the reduced-order model without the mass-invariant constraint are obtained as

$$\left[\bar{M}_{\text{idn}}\right] = \begin{bmatrix} 0.135 & 0.415 & 0.147 & 0.277 \\ 0.415 & 0.675 & 0.792 & 0.103 \\ 0.147 & 0.792 & 0.593 & 0.384 \\ 0.277 & 0.103 & 0.384 & -0.038 \end{bmatrix} \times 10^{6} \text{ kg}$$

and

$$\left[\bar{K}_{\text{idn}}\right] = \begin{bmatrix} -0.70 & 0.680 & -1.20 & 0.950 \\ 0.680 & -0.25 & 0.970 & -0.68 \\ -1.20 & 0.970 & -1.39 & 1.150 \\ 0.950 & -0.68 & 1.150 & -0.79 \end{bmatrix} \times 10^{8} \text{ N/m}$$

whereas these parameters after applying the mass-invariant constraint are estimated as

$$\left[\bar{M}_{\text{idn}}\right] = \begin{bmatrix} 0.977 & 0.279 & 0.000 & 0.000 \\ 0.279 & 1.527 & 0.393 & 0.000 \\ 0.000 & 0.393 & 1.335 & 0.157 \\ 0.000 & 0.000 & 0.157 & 0.624 \end{bmatrix} \times 10^{6} \text{ kg}$$

and

$$\left[\bar{K}_{\text{idn}}\right] = \begin{bmatrix} 4.060 & -1.24 & 1.016 & -0.69 \\ -1.24 & 2.918 & -0.93 & 0.167 \\ 1.016 & -0.93 & 2.823 & -1.25 \\ -0.69 & 0.167 & -1.25 & 1.922 \end{bmatrix} \times 10^{8} \text{ N/m}$$

On comparing these estimated values with the benchmark values shown in Equation (15), it may be seen that the parameter estimates obtained after imposing the mass-invariant constraint are in good agreement with the analytical results. The error in the identified stiffness matrix with respect to the analytically condensed stiffness matrix, evaluated in terms of the Frobenius norm, is 55% when the mass-invariant constraint is not used and 19% with this constraint in place. It may be mentioned here that some good results for the modal frequencies and damping of large-scale structures have also been obtained with the least-squares method without the use of mass-invariant constraint (Smyth et al., 2003). The use of mass-invariant constraint is aimed at improving the robustness of the least-squares identification of the system property matrices themselves and not just the modal characteristics. The natural frequencies of the (analytical and identified) reduced-order models are shown in Table 1 along with the first four natural frequencies of the full analytical model.

**Table 1: Natural Frequencies of Analytical and Identified Models**

| Model | Natural Frequencies (rad/s) | | | |
|---|---|---|---|---|
| | Mode 1 | Mode 2 | Mode 3 | Mode 4 |
| Analytical Model | 4.049 | 12.048 | 19.755 | 26.983 |
| Analytical Reduced Model | 4.085 | 12.718 | 25.186 | 29.314 |
| Identified Reduced Model | 3.793 | 11.935 | 14.595 | 25.920 |

It may be seen that the first two natural frequencies of the identified reduced-order model are in good agreement with the first two frequencies of the analytical model. Therefore, the first two eigenvalues of the identified reduced-order model will be used for the further analysis for damage identification as described next.

## RECOVERY OF FULL STRUCTURAL MATRICES

The identified stiffness coefficients correspond to the mathematically contrived reduced-order system and it is not possible to ascertain the health of physical structure by examining these coefficients. For the identification of damage, it is necessary to reconstruct the full-system matrices from the identified reduced-order matrices. A matrix updating based formulation to identify the incremental changes in the elements of stiffness matrix is proposed based on the condensed model identification and recovery method (CMIR). Koh et al. (2006) used an eigensystem realization algorithm (ERA) to identify a condensed model utilizing complete time-domain records. The proposed method differs only in the use of the least-squares time-domain identification method with the mass-invariant constraint for the identification of condensed models in different time windows, such that a progressive monitoring of the changes in the stiffness coefficients with reference to the undeformed configuration is allowed.

Let $\left[K_a\right]$ and $\left[M_a\right]$ denote the full stiffness and mass matrices of the virgin, undamaged system and $\left[K_p\right]$ and $\left[M_p\right]$ be the full stiffness and mass matrices of damaged system. Further, let $\left[\delta K\right]$ represent the incremental changes in the stiffness matrix due to damage. It is possible to relate the system matrices for the undamaged and damaged states as

$$\left[K_p\right]=\left[K_a\right]+\left[\delta K\right] \text{ and } \left[M_p\right]=\left[M_a\right] \tag{20}$$

where the stiffness increments $\left[\delta K\right]$ are to be determined iteratively so as to minimize the quadratic error function given by

$$\varepsilon=\sum_{j=1}^{2}\left(1-\frac{R_j}{\bar{R}_j}\right)^2 \tag{21}$$

Only two terms corresponding to the first two modes of vibration are considered in constructing the error function because for a reduced-order system of size $N$, approximately first $N/2$ eigenvalues correlate well with the eigenvalues of the original, full system. In Equation (21) $R_j$ and $\bar{R}_j$ respectively denote the Rayleigh quotients computed from the $j$ th mode shape vectors for the analytically condensed system matrices and the identified reduced-order matrices and are computed as

$$\bar{R}_j=\frac{\left\{\phi_{i_j}\right\}^T\left[\bar{K}_i\right]\left\{\phi_{i_j}\right\}}{\left\{\phi_{i_j}\right\}^T\left[\bar{M}_i\right]\left\{\phi_{i_j}\right\}} \quad \text{and} \quad R_j=\frac{\left\{\phi_{p_j}\right\}^T\left[\bar{K}_p\right]\left\{\phi_{p_j}\right\}}{\left\{\phi_{p_j}\right\}^T\left[\bar{M}_p\right]\left\{\phi_{p_j}\right\}} \tag{22}$$

where $\left\{\phi_{i_j}\right\}$ and $\left\{\phi_{p_j}\right\}$ are the $j$ th mode shapes of the identified and analytically reduced matrices, respectively, and $\left[\bar{K}_i\right]$ and $\left[\bar{M}_i\right]$ respectively denote the reduced-order stiffness and mass matrices identified by the time-domain least-squares identification procedure. Similarly, $\left[\bar{K}_p\right]$ and $\left[\bar{M}_p\right]$ respectively denote the analytically reduced stiffness and mass matrices as obtained from the updated structural matrices $\left[K_p\right]$ and $\left[M_p\right]$. The iterative procedure to determine the incremental changes in the stiffness matrix, $\left[\delta K\right]$, requires the computation of the error function for a configuration of incremental stiffness matrices and is arranged in the following order:

1. Considering the current values of the vector of design variables corresponding to the incremental stiffness matrix $\left[\delta K\right]$, the updated structural stiffness $\left[K_p\right]$ is determined as in Equation (20).
2. The matrices $\left[K_p\right]$ and $\left[M_p\right]$ are dynamically condensed to retain the terms corresponding to the primary DOFs only. Let $\left[\bar{K}_p\right]$ and $\left[\bar{M}_p\right]$ be the analytically reduced updated matrices.
3. The Rayleigh quotients based on the identified and reduced updated matrices are calculated by using Equation (22).

4. The error function for the current estimate of the incremental matrix $[\delta K]$ is calculated by using Equation (21).

Due to the symmetry of the stiffness matrix, only the upper triangular elements of $[\delta K]$ are considered as the design variables—a total of 19 elements for a 10-story building with rigid floor diaphragms—for the minimization problem. The design variables are numbered row-wise for the upper triangular part of $[\delta K]$. The sequential quadratic programming is used to minimize the error function defined in Equation (21) with respect to the design variables, i.e., stiffness increments. The upper and lower bounds on the stiffness coefficients are chosen to be 0 and 30% of the original stiffness coefficients, with negative sign added to indicate the nature of stiffness degradation with damage. The starting vector to begin the optimization process is picked by randomly choosing the design variables from the given range. To guard against the possibility of converging on a local minimum, the minimization process is repeated 40 times with randomly selected initial design vectors. The set of design variables corresponding to the minimum $\varepsilon$ (in 40 trials) is assumed to give the desired incremental matrix. This procedure is carried out for all the five time windows. The values of variables obtained for these windows after optimization are shown in Figure 5 and Table 2.

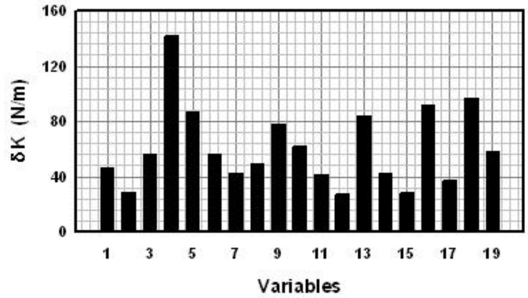


(a) First window (0-4 s)

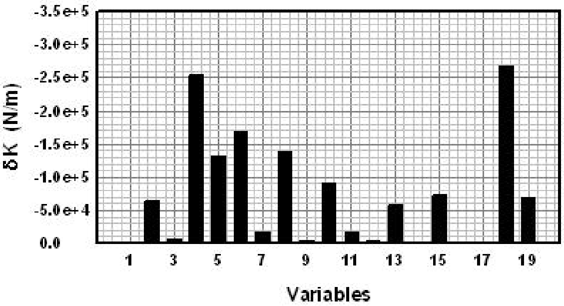


(b) Second window (4-8 s)

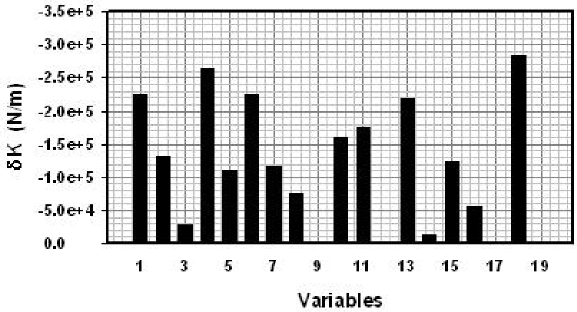


(c) Third window (8-12 s)

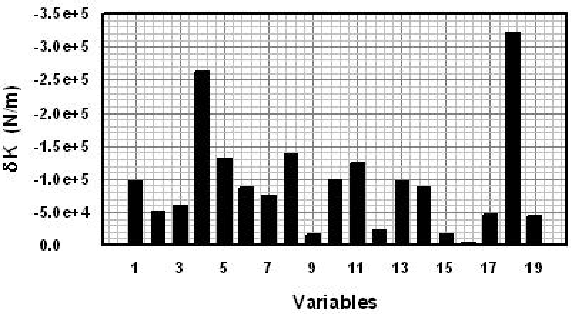


(d) Fourth window (12-16 s)

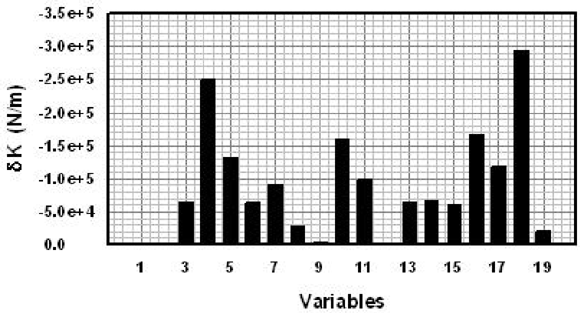


(e) Fifth window (16-20 s)

Fig. 5 Final values of design variables for different time windows

**Table 2: Changes in Stiffness Coefficients (×10$^5$ N/m) in Different Data Windows**

| Variable | 1st Window | 2nd Window | 3rd Window | 4th Window | 5th Window |
|---|---|---|---|---|---|
| $1(\delta k_{1,1})$ | −0.0005 | −0.0130 | −2.2558 | −0.9638 | −0.0025 |
| $2(\delta k_{1,3})$ | −0.0003 | −0.6460 | −1.3168 | −0.5232 | −0.0000 |
| $3(\delta k_{1,10})$ | −0.0006 | −0.0611 | −0.2906 | −0.5977 | −6546 |
| $4(\delta k_{2,2})$ | −0.0014 | −2.5440 | −2.6338 | −2.6440 | −2.5147 |
| $5(\delta k_{2,4})$ | −0.0009 | −1.3170 | −1.1087 | −1.3170 | −1.3170 |
| $6(\delta k_{3,3})$ | −0.0006 | −1.6953 | −2.2569 | −0.8937 | −0.6399 |
| $7(\delta k_{3,5})$ | −0.0004 | −0.1818 | −1.1664 | −0.7466 | −0.9012 |
| $8(\delta k_{4,4})$ | −0.0005 | −1.3783 | −0.7492 | −1.3916 | −0.2725 |
| $9(\delta k_{4,5})$ | −0.0008 | −0.0351 | −0.0095 | −0.1774 | −0.0399 |
| $10(\delta k_{5,5})$ | −0.0006 | −0.9041 | −1.5990 | 0.9988 | −1.5932 |
| $11(\delta k_{6,6})$ | −0.0004 | −0.1771 | −1.7523 | −1.2517 | −0.9868 |
| $12(\delta k_{6,8})$ | −0.0003 | −0.0460 | −0.0002 | −0.2451 | −0.0153 |
| $13(\delta k_{7,7})$ | −0.0008 | −0.5930 | −2.1749 | −0.9826 | −0.6468 |
| $14(\delta k_{7,9})$ | −0.0004 | −0.0120 | −0.1268 | −0.8811 | −0.6628 |
| $15(\delta k_{7,10})$ | −0.0003 | −0.7250 | −1.2371 | −0.1802 | −0.5957 |
| $16(\delta k_{8,8})$ | −0.0009 | −0.0254 | −0.5655 | −0.0427 | −1.6566 |
| $17(\delta k_{8,9})$ | −0.0004 | −0.0125 | −0.0005 | −0.4863 | −1.1847 |
| $18(\delta k_{9,9})$ | −0.0010 | −2.6834 | −2.8348 | −3.2201 | −2.9340 |
| $19(\delta k_{10,10})$ | −0.0006 | −0.6943 | −0.0324 | −0.4647 | −0.2237 |

The changes in the first time window (from 0 to 4 s) are negligible in comparison to the original stiffness coefficients. This indicates that the structure has not suffered any damage during the first time window. For all the subsequent time windows, the design variables 4 and 18 consistently show a significantly large stiffness decrement in comparison to the other variables. These two variables correspond to the stiffness coefficients corresponding to the DOFs 2 and 9, respectively. This is in agreement with the actual damage state of the structural system after the earthquake excitation in the SAP2000 simulation run with the formation of plastic hinges at the ground and eighth floors as shown in Figure 6. However, there are a number of inconsistencies as well, e.g., there are little or no changes in the coupling terms for the DOF 9 to the adjacent DOFs. In addition, there are some false alarms, which are more prominent in the third data window. For the simple analytical model considered in this study, it is possible to segregate these anomalies as outliers and discard those but it may be difficult to take a definitive call in the case of a more complex and realistic analytical model.

## CONCLUSIONS

A matrix update method based on the reduced-order model identified by the time domain least-squares identification procedure is proposed. The effectiveness of the proposed identification procedure for damage detection is demonstrated with the help of an example problem of a structural steel frame damaged by an earthquake ground motion. The 10-story frame is modeled in SAP2000 to simulate the damage during the earthquake excitation. A mass-invariant constraint is proposed for use with the time-domain least-squares identification procedure and is found to be effective in improving the robustness of the identification procedure.

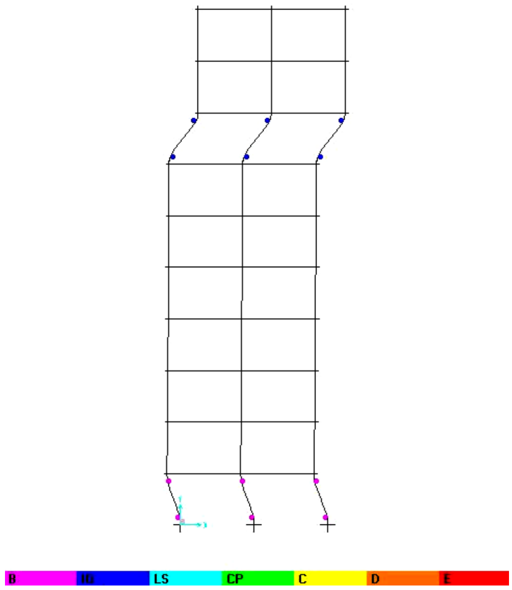


Fig. 6 Damage state of frame after excitation

A moving window analysis is performed to track temporal changes in the stiffness properties of the structural system. The model identification and recovery method is used to recover the full-system matrices from the identified reduced-order matrices for each of the five time windows considered in the analysis. An optimization problem is formulated to identify the required increments in stiffness coefficients in each time window. It is observed that the design variables 4 and 18 (associated with the DOFs 2 and 9 of the structural frame of Figure 1) are consistently large in all time windows, except for the first one, as compared to the other variables. In addition, the magnitudes of these two variables are approximately same across all time windows (except for the first window), while other variables exhibit relatively more variations over time. The consistent indications of reduction in stiffness corresponding to these design variables suggest damage in the ground and eighth floors of the structural frame. Nevertheless, there are also a number of inconsistencies in the identification results, which are easily recognized as anomalies and discarded in the simple example system considered in this study. However, the results of parametric identification of a chosen reduced-order model from different time windows and their extrapolation to a full model may not work well in more realistic and complex systems. In this regard, it would be better to use the time-domain least-squares identification procedure for estimating modal parameters as those are better constrained than the stiffness (and/or mass) coefficients.

## REFERENCES

1. Agbabian, M.S., Masri, S.F. and Miller, R.K. (1990). "System Identification Approach to Detection of Structural Changes", Journal of Engineering Mechanics, ASCE, Vol. 117, No. 2, pp. 370–390.
2. Baruch, M. and Bar Itzhack, I.Y. (1978). "Optimum Weighted Orthogonalization of Measured Modes", AIAA Journal, Vol. 16, No. 4, pp. 346–351.
3. BIS (1989). "IS 808: 1989—Indian Standard Dimensions for Hot Rolled Steel Beam, Column, Channel and Angle Sections (Third Revision)", Bureau of Indian Standards, New Delhi.
4. Choudhury, K. (2007). "On the Reliability of a Class of System Identification Procedures", M.Tech. Thesis, Department of Earthquake Engineering, Indian Institute of Technology Roorkee, Roorkee.
5. Datta, A.K., Shrikhande, M. and Paul, D.K. (2002). "On the Optimal Location of Sensors in Multi-storeyed Building", Journal of Earthquake Engineering, Vol. 6, No. 1, pp. 17–30.
6. Golub, G.H. and Van Loan, C.F. (1996). "Matrix Computations", The Johns Hopkins University Press, Baltimore, U.S.A.

7. Heredia-Zavoni, E. and Esteva, L. (1998). "Optimal Instrumentation of Uncertain Structural Systems Subjected to Earthquake Ground Motions", Earthquake Engineering & Structural Dynamics, Vol. 27, No. 4, pp. 343–362.
8. Koh, C.G., Tee, K.F. and Quek, S.T. (2006). "Condensed Model Identification and Recovery for Structural Damage Assessment", Journal of Structural Engineering, ASCE, Vol. 132, No. 12, pp. 2018–2026.
9. Pandey, A.K. and Biswas, M. (1994). "Damage Detection in Structures Using Changes in Flexibility", Journal of Sound and Vibration, Vol. 169, No. 1, pp. 321–332.
10. Paz, M. (1984). "Dynamic Condensation", AIAA Journal, Vol. 22, No. 5, pp. 724–727.
11. Paz, M. and Leigh, W.E. (2004). "Structural Dynamics: Theory and Computation", Kluwer Academic Publishers, Dordrecht, The Netherlands.
12. Smyth, A.W., Masri, S.F., Caughey, T.K. and Hunter, N.F. (2000). "Surveilance of Mechanical System on Basis of Vibration Signature Analysis", Journal of Applied Mechanics, ASME, Vol. 67, No. 3, pp. 540–551.
13. Smyth, A.W., Pei, J.S. and Masri, S.F. (2003). "System Identification of the Vincent Thomas Suspension Bridge Using Earthquake Records", Earthquake Engineering & Structural Dynamics, Vol. 32, No. 3, pp. 339–367.
14. Stubbs, N., Kim, J.T. and Farrar, C.R. (1995). "Field Verification of a Nondestructive Damage Localization and Severity Estimation Algorithm", Proceedings of the 13th International Modal Analysis Conference, Nashville, U.S.A., pp. 210–218.
15. Udwadia, F.E. (2005). "Structural Identification and Damage Detection from Noisy Modal Data", Journal of Aerospace Engineering, ASCE, Vol. 18, No. 3, pp. 179–187.